TECHNISCHE UNIVERSITÄT WIEN
Vienna University of Technology

# Master Thesis

## Additive Manufacturing of Tricalcium Phosphate Scaffolds for Bone Tissue Engineering

*Conducted at:*
Institute of Materials Science and Technology
Vienna University of Technology

*Under the supervision of:*
Prof. Jürgen Stampfl

*By:*
Christina Schmidleithner

Date

Signature (Student)

# Abstract

Bone fractures caused by trauma or disease can significantly decrease quality of life and pose a growing issue in our aging population [1]. Especially for large defects, native bone repair can be insufficient, and surgical intervention is often required. In that case, bone tissue engineering (TE) has emerged as an alternative to conventionally used tissue grafts [2].

In TE, scaffolds are combined with cells and growth factors to induce the formation of new tissue. These scaffolds need interconnected porosity to enable cell migration, nutrient and endotoxin transportation, and neovascularization. Simultaneously, adequate mechanical integrity is required to ensure load bearing capacity [3], [4]. One approach to attain high strength and low density materials, is by engineering of lattice topology. The present study uses additive manufacturing to precisely define scaffold architectures for tunable mechanical properties and optimized biological activity.

Tricalcium phosphate (TCP) scaffolds with four different pore geometries are designed. A rectilinear cylinder grid lattice, a triply periodic minimal surface (TPMS) inspired Schwarz primitive architecture, a shellular-type hollow Schwarz primitive scaffold, and finally a Kagome geometry with hexagonal unit cell are created using a digital light processing (DLP) stereolithography (SLA) system. Pore sizes for all geometries are set in a range of 400 - 600 μm at porosities of 25, 50, and 75 vol.%.

Material characterization by X-ray photoelectron spectroscopy (XPS) and X-ray diffraction (XRD) confirms presence of the pure β-TCP phase without remnants of organic binder or other contaminants. Validation of geometrical accuracy and homogeneous pore distribution throughout the scaffolds is implemented by micro computed tomography (μ-CT). After incorporation of experimentally determined scaling factors, the cylinder grid geometry is the most reproducible architecture with < 2 vol.% error in porosity and < 6 % relative deviation of average pore sizes. This structure also has the highest compressive strength of 44.7 MPa at 50 vol.% porosity while the Kagome architecture has 19.5 MPa at the same density. Manufactured bulk specimens reach a density of up to 99.50 ± 0.18 % of crystallographic values and compressive strength of 235 ± 37 MPa. After submersion in simulated body fluid (SBF) for 21 days, all investigated scaffolds show increased intergranular porosity in scanning electron microscopy (SEM) images but no significant change in mass.

Preliminary cell culture studies with murine preosteoblast MC3T3-E1 cells on the cylinder grid and the Kagome scaffolds confirm cell growth and early osteogenic markers indicate differentiation into osteoblasts.

With mechanical properties comparable those of bone at similar densities and excellent geometrical reproducibility, as well as promising biological attributes, both the cylinder grid and the Kagome architectures could have future applications in regenerative medicine as bone TE scaffolds.

# Kurzfassung

Knochenbrüche, die durch Traumata oder Krankheiten verursacht werden, können die Lebensqualität erheblich beeinträchtigen und bereiten ein zunehmendes Problem in unserer alternden Gesellschaft [1]. Insbesondere bei großen Defekten kann native Knochenreparatur unzureichend sein, und häufig ist ein chirurgischer Eingriff erforderlich. In diesem Fall hat sich das Tissue-Engineering (TE) als Alternative zu herkömmlich verwendeten Gewebetransplantaten etabliert [2].

In TE werden Scaffolds (Gerüststrukturen) mit Zellen und Wachstumsfaktoren kombiniert, um Bildung von neuem Gewebe zu induzieren. Diese Scaffolds benötigen durchgehend verbundene Porosität, um Zellmigration, Nährstoff- und Endotoxintransport sowie Bildung neuer Gefäße zu ermöglichen. Gleichzeitig ist eine ausreichende mechanische Stabilität erforderlich, um die Belastbarkeitdes Knochens zu gewährleisten [3], [4]. Ein Ansatz, um Materialien mit hoher Festigkeit und geringer Dichte herzustellen, ist das Modifizieren der Gittertopologie. In der vorliegenden Arbeit werden durch generative Fertigung die Scaffold-architekturen genau eingestellt, wodurch mechanische Eigenschaften sowie biologische Aktivität optimiert werden können.

Tricalciumphosphat (TCP) -Gerüste mit vier unterschiedlichen Porengeometrien werden entworfen. Ein geradliniges Zylindergitter, die Kagome Geometrie mit hexagonaler Einheitszelle, die Schwarz primitive Architektur ,welche zu den ´triply periodic minimal surfaces' (TPMS) zählt, sowie die Shellular Version dieser TPMS Geometrie werden unter Verwendung von Digital Light Processing (DLP) Stereolitographie (SLA) hergestellt. Die Porengrößen aller Geometrien werden in einem Bereich von 400 bis 600 µm bei Porositäten von 25, 50 und 75 % festgelegt.

Durch Röngtenphotoelektronen-Spektroskopie (XPS) und Röngtendiffraktion (XRD) kann eine reine β-TCP Phase ohne organischen Binderrückständen oder sonstigen Verunreinigungen bestätigt werden. Weiters kann die exakte Geometrie und die homogene Porengrößenverteilung durch mikro Computer Tomographie (µ-CT) validiert werden. Nach Einbau experimentel ermittelter Skalierungsfaktoren ist die Zylindergittergeometrie die am besten reproduzierbare Architektur mit < 2 vol.% Fehler in der Porosität und < 6 % relative Abweichung der durchschnittlichen Porengrößen. Diese Struktur hat bei 50 vol.% Porosität auch die höchste Druckfestigkeit von 44.7 MPa, während die Kagome-Architektur eine Stärke von 19.5 MPa aufweist. Porenfreie Proben hingegen haben eine Festigkeit von 235 ± 37 MPa und eine Dichte von 99.50 ± 0.18 % des theoretischen Wertes kann erreicht werden.

Nach dem Einlegen in simulierte Körperflüssigkeit (SBF) für 21 Tage zeigen alle untersuchten Scaffolds erhöhte intergranulare Porosität unter dem Rasterelektronenmikroskop (SEM), aber keine signifikante Änderung in der Masse.

Vorläufige Zellkulturstudien mit Maus-Preosteoblasten (MC3T3-E1 Zellen) auf dem Zylindergitter und den Kagome-Scaffolds bestätigen Zellwachstum, und frühe osteogene Marker weisen auf eine Differenzierung zu Osteoblasten hin.

Neben diesen vielversprechenden biologischen Eigenschaften sind weiter Voraussetzungen wie die hohe Reinheit des Materials, die ähnlichen mechanischen Eigenschaften zu Knochen und exzellente geometrische Reproduzierbarkeit erfüllt. Somit können sowohl das Zylindergitter, als auch die Kagome-Architekturen zukünftig Anwendung in der regenerativen Medizin als Knochen-TE-Scaffolds finden.

# Acknowledgments

Foremost, I would like to express my gratitude to Prof. Jürgen Stampfl for allowing me to conduct this project under his supervision and for sharing his insights and support especially in the final stages of the master thesis.

I would, furthermore, like to thank Dr. Deepak Kalaskar and his research group at UCL, where I was allowed to carry out most of the experimental part. I am very grateful to Sara for finding time in her busy schedule to help me with cell culture issues and particularly to Tania for introducing me to the group, taking me under her wing, and always being available for interesting and more often than not eye-opening discussions.

I would also like to sincerely thank Dr. Martin Schwentenwein and Dr. Daniel Bomze from Lithoz for a great cooperation. I very much appreciate the efficient, productive, but also fun working environment. Especially Patrizia's assistance in the laboratory was vital, as she almost magically solves problems before they fully manifest.

Moreover, I would like to acknowledge Dr Robert Palgrave from the UCL Department of Chemistry for the many analytical measurements that I was able to complete with his help and Dr. Michelangelo Corcelli for the µ-CT assistance.

I am also indebted to my family for their more than just emotional support. I want to thank Lisa for brainstorming cell culture crises with me and for proof reading the master thesis. Many thanks go to my Father for taking photographs of scaffolds and to my Mother for correcting the German version of the Abstract.

I would also like to express my deep gratitude to Emanuel for keeping me grounded and for his patience in helping me overcome setbacks.

# Abbreviations

| | |
|---|---|
| ACP | Amorphous calcium phosphate |
| ALP | Alkaline phosphatase |
| ARS | Alizarin Red S |
| CAD | Computer aided design |
| $C_d$ | Cure depth |
| DAPI | 4',6-diamidino-2-phenylindole dihydrochloride |
| DLP | Digital light processing |
| DMD | Digital micromirror device |
| $D_p$ | Penetration depth |
| $E_c$ | Critical energy |
| ECM | Extracellular matrix |
| FWHM | Full width at half maximum |
| HA | Hydroxyapatite |
| IOMS | Institute of Orthopedics and Musculoskeletal Science |
| MEMS | Microelectromechanical system |
| MSC | Mesenchymal stem cells |
| PDMS | Polydimethylsiloxane |
| PI | Photoinitiator |
| pNP | Para-nitrophenol |
| pNPP | Para-nitrophenylphosphate |
| PTFE | Polytetrafluoroethylene |
| SBF | Simulated body fluid |
| SEM | Scanning electron microscopy |
| SLA | Stereolithography |
| st.dev. | Standard deviation |
| TTCP | Tetracalcium phosphate |
| UCL | University College London |
| XPS | X-ray photoelectron spectroscopy |
| XRD | X-ray diffraction |
| β-TCP | Beta tricalcium phosphate |
| µ-CT | Micro computed tomography |

# Contents

# 1. Introduction

## 1.1 Digital Light Processing-Based Stereolithography

In the present work, digital light processing (DLP) based stereolithography (SLA) is employed to fabricate highly complex and precisely defined scaffold structures. As in all additive manufacturing methods, the first step in DLP is the creation of a computer aided design (CAD) model of the required geometry. Conversion into an STL file approximates the surface of the object using triangles. This triangulated geometry is then sliced into individual layers, which is necessary for the subsequent manufacturing of the structure [5].

DLP is a method used in SLA where a photocurable resin is selectively illuminated by UV or visible light one layer at a time. A 3D body can thus be generated in a layer-by-layer manner. In contrast to laser-based SLA, the entire area of the layer is exposed at the same time by a digital micromirror device (DMD) coupled to a projection system [6]–[8].

### 1.1.1 Digital Micromirror Device

The DMD is the key component of the DLP process. It is a microelectromechanical system (MEMS) which functions as a dynamic mask when linked with an image processing computer, a light source, and optics [9]. It can then precisely and quickly project designated cross-sections of light. The chip was developed at Texas Instruments in 1987 and is comprised of an arrangement of mirrors, as displayed in Figure 1. Each mirror is mounted on top of a yoke and hinge system on a silicon memory cell, creating a single pixel.

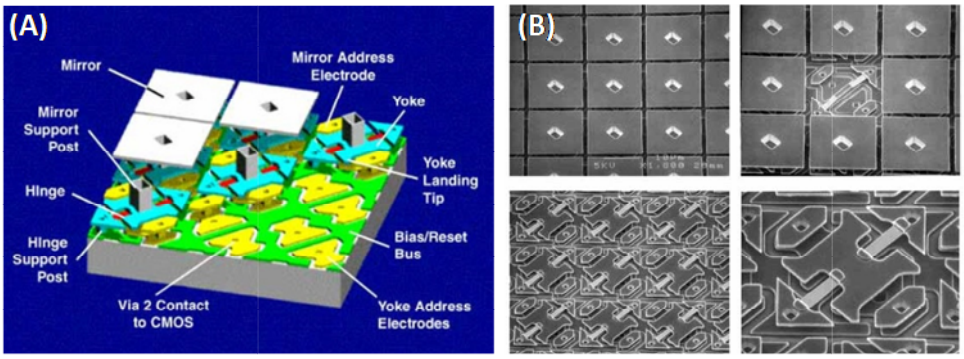


*Figure 1: (A): DMD array schematically and (B): SEM images, reprinted from* [10]

Without applying voltage, the aluminum mirrors are in a stable position in their flat states. When a high enough bias voltage is applied to mirror and yoke, electrostatic attractions create bistable equilibrium positions. These are precisely defined by geometrical limitation of hinge movement at +10° or -10°. The address voltage can then be applied and determines in which of the two directions the mirror tilts. Thus, when switched to 'off', the mirror deflects light away from the target towards an absorber. Correspondingly, when in its 'on' position, light is reflected towards the projection lens, creating the image. This system allows pixels to be switched quickly and reliably [10].

### 1.1.2 The Digital Light Processing Setup

In the DLP process, geometry data and illumination parameters such as exposure energy and time are sent to the imaging unit. Through a projection system, a photopolymerizable mixture is exposed to light and thereby cured. After curing of one layer, the growing parts are re-coated with a uniform film of resin to be able to create the subsequent layer [6].

The setup can be implemented with either a free surface approach (Figure 2 A) or a constrained surface approach (Figure 2 B). In the former, the building platform is lowered into a bath of resin and illumination occurs from above. After each layer, the z-stage is incrementally lowered into the resin

tank and fresh material is coated on top of the growing parts, often by a mechanical sweeper device, to prepare for the following layer [7], [8].

In the constrained surface approach, resin is illuminated from below through a transparent vat. After curing of each layer is complete, the building platform and its attached parts are raised by a defined distance, which determines the layer thickness. The liquid slurry can then flow into the gap and the next layer is prepared. Thus, the manufactured parts grow, suspended from the platform downwards [11].

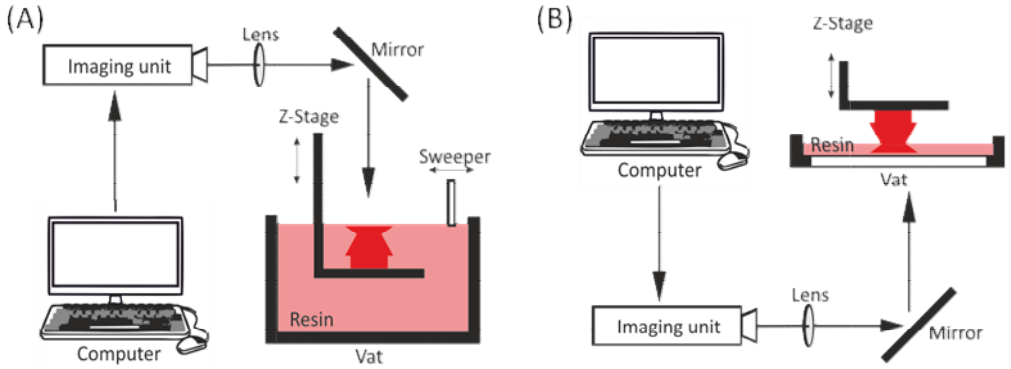


*Figure 2: (A): DLP setup free surface approach and (B): constrained surface approach. Redrawn from* [12]

The recent trend towards the constrained surface approach [11]–[13], which is also used in the present thesis, can be explain by some significant advantages. One of them being accurate movement of the z-stage down to precisions of 0.1 – 1 µm, defining layer height and creating smooth surfaces [14], [15]. This type of layer formation eliminates the need of mechanical sweepers and reduces manufacturing time [12]. Additionally, the created layer is not directly exposed to the air, limiting oxygen inhibition.

Another advantage is that the structure is not entirely submerged in the resin vat, reducing the required amount of resin and by extent the associated costs. The material that is used can be added dose-wise during the SLA process, ensuring continual supply of fresh resin even for larger jobs. If the photocurable mixture is left to age in the resin bath, monomers outside of the designated cross-section can be partially cured by scattered light, which would negatively affect viscosity of the bath and resolution of the produced specimen [8].

One difficulty in the constrained surface setup, however, is overcoming the attractive forces between the manufactured part and the vat floor after each layer [16]. Layers need to adhere to each other and to the building platform more strongly than they do to the vat surface to ensure both that newly irradiated layers do not stick to the bottom and that manufactured parts do not fall from the platform. Approaches to reduce interaction between the cured part and the material tray include coatings of the latter with hydrophobic films such as polytetrafluoroethylene (PTFE) [15], [17], silicon [16], or polydimethylsiloxane (PDMS) [12]. Modifying the separation mechanism with a tilting step of the building platform rather than just lifting it in its horizontal position, can cause the layer to peel off easily [18]. Similarly, applying shear force has also been successfully implemented [17]. An unwanted side effect of these approaches, however, is increase in process time [12].

### 1.1.3 Advantages and Disadvantages

When compared to other additive manufacturing techniques, which have resolutions ranging between 50 – 200 µm [11], [19], [20], SLA based processes show superior properties. Conventional laser lithography machines reach resolutions of 15 – 25 µm [19]. Pinpoint solidification in the focal point of the laser can even lead to submicron resolutions of 0.4 µm in linear optics [21] and spatial resolution of below 0.1 µm is possible with two-photon SLA methods [22], [23]. While typical DLP

resolution is in the order of 25 µm [20], lateral resolutions of 40 µm and layer thickness of 15 µm have been attained with DLP for ceramic-filled resins [15].

A drawback to SLA, also related to smaller layer heights, is longer manufacturing times. Especially for laser-based systems, the point-by-point scanning of each layer's cross-section is time consuming [24]. DLP systems can illuminate an entire layer simultaneously, which, combined with high switching speeds of the DMD [10], decreases manufacturing times irrespective of shape, complexity, or exposure area [6]. This is not only beneficial for financial reasons but is an important prerequisite when working with only partially stable resins, which can necessitate fast processing times [7].

In DLP, the pixel-based exposure mechanism is suitable for features with 90° angles but can be problematic when illuminating curved surfaces, as saw-tooth type roughness is created. Reduction of pixel size, either by increasing the number of mirrors on the DMD or by shrinking the image, can increase resolution [15]. Furthermore, the resins employed in SLA must be photocurable, which somewhat restricts the possible materials and to date only one material can be processed at a time in SLA [11].

In conclusion, when aiming to create specimens with high resolution and in larger quantities, DLP is the method of choice. It combines the accuracy of SLA with the speed of the DMD [8].

### 1.1.4 The Resin Components

Essential components for photocurable resins are the polymer precursors and photoinitiators (PI). Additionally, absorbers are employed for increased control over the reaction and rheological additives are crucial, especially for filled resins.

*Precursors*

Depending on future applications and desired properties, different monomers, oligomers, or prepolymers are employed as polymer precursors.

(Meth)acrylate-based resins for free radical polymerization are very common in DLP processes [20]. For example Murphy *et al.* developed a system based on high molecular weight and highly viscous di(meth)acrylates which were dissolved in low molecular weight (meth)acrylates with a reactive dilutant, *N*-vinylpyrrolidone (NVP) [25]. While acrylates are more reactive than methacrylates, they exhibit extensive shrinkage during curing, which can cause unwanted deformation. The combination with methacrylates is intended to reduce shrinkage while retaining high reactivity [25], [26]. Minimizing shrinkage can also be attempted by including cycloaliphatic or aromatic moieties [20]. The functionality of the monomers can be altered to tune cross-linking density and consequently final mechanical properties [26]. A wide variety of urethane acrylates can also be used for tunable strengths as well as high heat resistance [27].

With the development of efficient cationic PIs [28], cationic photopolymerization-based resins such as epoxy systems have been employed in SLA [29]. Although generally needing longer curing times and being inhibited by moisture, these reactions have enhanced stability against oxygen [30]. Furthermore, epoxy resins exhibit lower shrinkage during curing than their radical counterparts due to their ring opening polymerization mechanism [31].

Hybrid systems can exploit the advantages of both alternatives. By combining acrylate and epoxy-based resins, fast curing and low shrinkage materials can be reached [32].

*Photoinitiator*

Another prerequisite to a successful reaction, beside monomers or oligomers as a basis, is a suitable PI to start the reaction. Depending on the nature of the utilized pre-polymers, radical or cationic PIs need to be selected based on a number of criteria.

The nature of the PI and its concentration in the resin can substantially influence reaction kinetics as well as mechanical properties of the manufactured parts [26], [33], [34]. To minimize energy dosage and therefore exposure time, the absorption maximum of the PI should closely match the irradiation wavelength. With increased light intensity or PI concentration, more reactive species are generated to initiate the polymerization and the resulting conversion is elevated [33]. This affects cross-linking density and by extent, the specimen's stiffness [35].

For biomedical applications, cytotoxicity needs to be taken into account. PIs for cationic polymerization form strong protonic acids in addition to radicals and are therefore not employed in biological environments [29], [36]. Although the radicals generated by radical PIs are also cytotoxic and can lead to DNA damage, they have been utilized in cell-encapsulating polymerization, as low concentrations are survivable by cells [35], [36]. A commonly used low-toxicity PI is Irgacure 2959 [37].

*Absorber*

Another essential component in most SLA resins is a UV or visible light absorber to limit cure depth ($C_d$). This prevents loss in feature development by excessive curing in the z-direction, which is vital for complex geometries with undercuts [6], [8], [38]. However, polymerization rates and cross-linking density are also negatively affected by the absorber. Therefore, absorber concentrations should be decreased as much as possible, which can be achieved by selecting dyes, such as benzotriazole derivates, whose absorption maxima correspond to irradiation wavelengths [39].

### 1.1.5 Filled Resins

Manufacturing metallic or ceramic materials with DLP is possible by utilizing filled resins. Powder added to the organic resin is encapsulated in the created part when the matrix is cured. Subsequently, removal of the organic binder by thermal degradation, a debinding step, and sintering [40]–[42] of the specimens, yields dense materials, as shown schematically in Figure 3 [18].

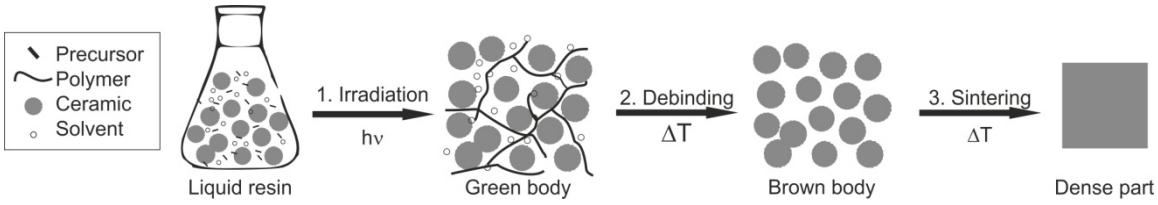


*Figure 3: Manufacturing scheme of dense ceramic parts by DLP; adapted from* [43]

Particle size is an important parameter in filled resins, as they need to be smaller than the layer height while still fulfilling rheological and optical requirements. High particle content, *i.e.* a volume fraction of at least 0.5 is required to retain geometrically accurate specimens without defects after debinding and to reduce shrinkage during sintering [40], [41]. A positive side effect of a high powder content is that shrinkage of the organic matrix during the polymerization process itself is inhibited, further increasing the precision [26].When the organic component is not removed, it can function as a matrix in the final part. Thus, it is possible to create composite materials with DLP [44], [45].

*Viscosity*

Solid loading greatly affects viscosity. Small filler particles and their correspondingly large surface areas can drastically increase slurry viscosity when added at high volume fractions [41]. This negatively affects the rheology of the resin and reduces coating efficiency, potentially leading to the formation of air bubbles. Furthermore, mechanical forces on the manufactured specimen are increased, necessitating higher forces for elevation of the z-stage in constrained surface DLP machines [16]. A benchmark value, below which fabrication is possible has been estimated at < 5 Pa·s [46]. Reduction of the viscosity can be implemented by increasing the temperature, incorporating diluents, or evoking thixotropic behavior [47].

Temperature dependence of resin viscosity is expected to follow Arrhenius type behavior [47], [48]. However, heating the resin during manufacturing can drastically lower viscosities beyond the predicted model if, for example, the temperature is above the melting point of matrix components [49]. Thermal dilution can be achieved if the organic matrix has a higher thermal expansion coefficient than the inorganic filler. In that sense, volume of the matrix increases in respect to filler, effectively decreasing the solid loading and, subsequently, the resin viscosity [47].

Non-reactive diluents such as N-methylpyrolidone [19] as well as reactive, low viscosity monomers have been used to decrease slurry viscosity [26]. Rheological additives, such as polyelectrolyte surfactants, can cause shear thinning attributes, facilitating the manufacturing process [48].

*Resin Stability*

Rheological additives can increase the stability of filled slurries during larger jobs and extend their shelf-life by ensuring a consistently homogeneous slurry composition and powder distribution [48]. Particle sedimentation or agglomeration can be reduced by the use of dispersants like oligomeric surfactants [50], long-chained fatty acids [51], or phosphine oxides [52]

These surface-active agents adsorb onto ceramic particles with their hydrophilic moieties, whereas their hydrophobic components positively interact with the often apolar monomer matrix. Thus, for optimized packing density, minimum viscosity, and enduring slurry stability, high adsorption level onto the powder is paramount [50].

Particle dispersion can be ensured, also in aqueous media, by steric or electrosteric repulsion of polyelectrolyte stabilizers. By adsorbing polyelectrolytes onto the particles in aqueous media and then transferring the thusly modified filler to the organic matrix, the same mechanism can be engaged to stabilize the photocurable slurry [48].

*Light Scattering*

In highly loaded ceramic suspensions with particles in the colloidal domain, the major mechanism of interaction with light is scattering, which consequently determines $C_d$. Griffith *et al.* have established a model for ceramic loading of > 0.1 and for particle sizes in the dimensions of the wavelength of incident light, as expressed in Equation (1) [53].

$$C_d = \frac{2d}{3Q}\frac{n_0^2}{\Delta n^2} ln\left(\frac{E}{E_c}\right) \quad (1)$$

$C_d$ … *Cure depth [µm]*
$d$ … *Average particle size [µm]*
$Q$ … *Scattering efficiency term*
$n_0$ … *Refractive index of medium*
$\Delta n$ … *Refractive index difference*
$E$ … *Energy density [mJ cm$^{-2}$]*
$E_c$ … *Minimum energy density [mJ cm$^{-2}$]*

The combined pre-logarithmic factor can be interpreted as the inverse of the extinction coefficient in Beer's law, also referred to the penetration depth of the incident light. Thus, it is apparent that the attenuation of light is highly dependent on the refractive index and that $\Delta n$ is a decisive factor on scattering behavior [53].

In order to predict both cure width, and thereby lateral resolution of the DLP process, as well as cure depth, the aforementioned parameters need to be precisely defined. It has been shown that while greater solid loading increases light attenuation in the z-direction, it has no effect on the lateral attenuation factor [54]. Approaches to decrease lateral scattering have therefore been focusing on tuning of the refractive index [48], [55].

## 1.2 Bone

Bone is an organ with many metabolic functions such as mineral storage, detoxification, and regulation of the acid-base balance. Blood production is another important task of bone and sound transduction through bone plays a significant part in hearing. The focus in the present work, however, lies in their structural function. Bones serve as levers for muscle action, as protection of vital organs, and as structural support, often in load bearing configurations [56], [57].The following chapter discusses bone formation, the structural properties of bone tissues, and the bone remodeling process.

### 1.2.1 Osteoblast maturation

One distinguishes between two methods in bone formation; intramembranous and endochondral. The former occurs in the development of flat bones, where adequate vascularization is present. In the latter, bone is formed through intermediate cartilage growth. In both cases, osteoblasts differentiate from mesenchymal stem cells (MSC), and although they undergo different intermediate steps, they share the same mechanism of osteoblast maturation from pre-osteoblasts [58].

The first phase of this three-step process is defined by continued proliferation of pre-osteoblasts. In stage two, differentiation commences, collagen is deposited, alkaline phosphatase (ALP) activity rises, and the extracellular matrix (ECM) matures. Finally, differentiation is completed while the mature ECM is mineralized. This is accompanied by osteocalcin expression and characteristic formation of the cuboid shape of osteoblasts [58], [59].

### 1.2.2 Bone Structure

Bone tissue is an anisotropic composite material with hierarchical structure, compare Figure 4. Collagen fibrils, which are mineralized by formation of hydroxyapatite (HA) crystals, are assembled to fibers, fiber patterns, and osteons, finally forming macroscopic bone tissue [60].

The organic collagen matrix accounts for bone toughness, while stiffness and strength is provided by the inorganic HA phase [56]. Next to these intrinsic material properties, the structuring is decisive especially for crack-growth resistance. Many different mechanisms that impede crack propagation, such as crack deflection and formation of mother-daughter cracks, directly depend on the bone microstructure and are essential for fracture resistance of bone [61], [62].

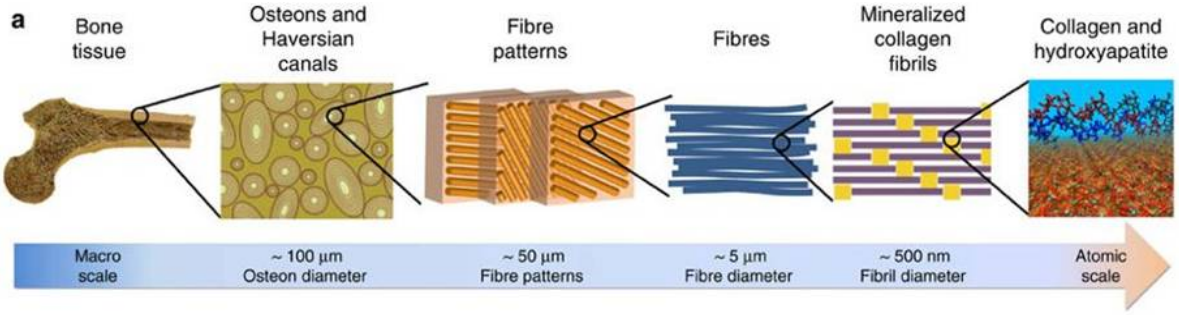


*Figure 4: Hierarchical structure of bone tissue, reprinted from* [60]

Although all types of bones share the aforementioned building blocks, two main categories, cancellous and cortical bone, with vastly different structures and properties can be distinguished, as shown in Figure 5 [63]. Cortical or compact bone has compressive strengths ranging from 130 - 180 MPa at porosities of 5 - 13 % [64], [65]. It is organized into circular subunits called osteons. Mineralized lamellae form concentric rings around an haversian canal containing blood vessels and nerves [57]. Cancellous bone, also called trabecular or spongy bone, is less dense at 30-90 % porosity with compressive strengths of 4 - 12 MPa [64], [65]. The fiber patterns are longitudinally arranged to form trabeculae, which are in turn oriented depending on direction of loading [56].

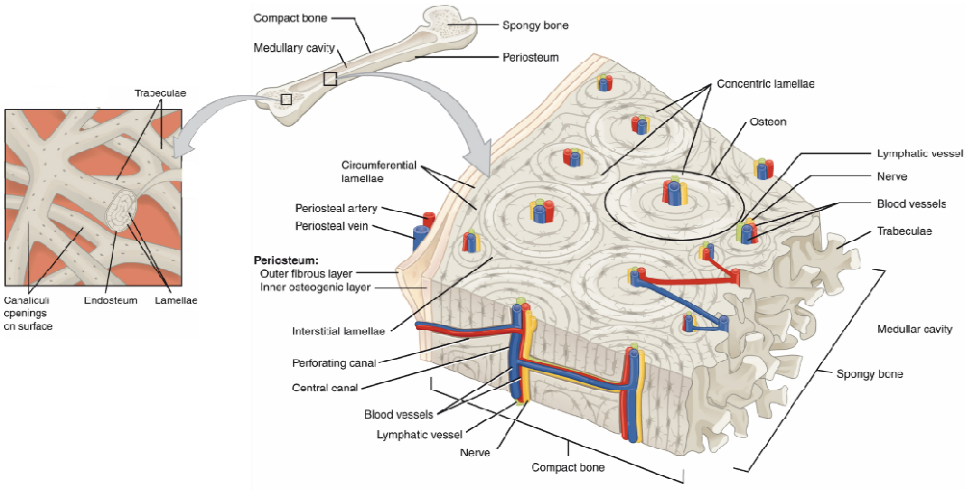


*Figure 5: Cortical and cancellous bone structure, modified and reprinted from* [57]

### 1.2.3 Bone Remodeling

Bone is a dynamic tissue, which constantly undergoes repair and remodeling. In homeostasis, an equilibrium between resorption and formation is reached. Osteoclast precursors are attracted to the site of resorption and differentiate to form mature osteoclasts, which attach themselves to the bone surface. By secretion of acids and proteolytic enzymes, dissolution of HA and degradation of collagen leads to bone resorption. Recruitment of osteoblast precursors on the other hand, and differentiation to mature osteoblasts, leads to bone formation. First, uncalcified bone matrix or osteoid is formed on the surface and calcification occurs within the next days, creating the mature bone [66], [67].

Osteoblasts, which are trapped within this new mature bone, differentiate to osteocytes and those which remain on the surface form the flat bone lining cells. Osteocytes are responsible for sensing mechanical stresses as well as for the production of signalling molecules. Their interconnected nature is vital for communication [56], [66].

Bone remodeling is influenced by different factors such as inflammation, where resorption is augmented, or mechanical loading, which shifts the equilibrium toward the formation of bone [56]. Many bone diseases, such as osteoporosis, occur due to a dysregulation of the balance between these two opposing forces [68].

Stress shielding is another effect of this resorption regulation. According to Wolff's law, bone will remodel depending on mechanical signals, which can be problematic for example in hip replacements. When loads are shielded by the implant and not correctly transmitted to the femur, the reduction in stress leads to loss in bone mass, potentially causing secondary fractures or aseptic loosening. Thus, difficult revision surgeries can become necessary. This highlights the need for precisely defined implants with biomimetic load configurations [69], [70].

## 1.3 Bone Tissue Engineering Scaffolds

The employment of bone grafts has become the standard surgical method for repairing large bone defects [71]. However, both allografts and autografts have certain disadvantages.

Allografts utilize bone from living donors or cadaveric bone, which is devitalized either by freezing or through irradiation. After removal of soft tissue often through ultrasonication, it can be implanted into the patient. Potential immunogenic reactions [72] and the possibility of disease transfer [73] present risks and the absence of viable cells in allografts increases integration time of the graft [74], [75].

For autologous bone grafts, bone is harvested from the patient at a donor site and implanted at the site of the injury [76]. Grafted bone originates from the patients themselves and the presence of living osteogenic cells and growth factors overcome disadvantages of allografts [75], yielding more predictable results [77]. However, long operation durations, limited amounts of available bone tissue, and the occurrence of donor site morbidity remain problematic [77], [78].

Synthetic scaffolds for bone TE are thus being investigated as a potential alternative [2]. When these porous scaffolds are combined with cells and growth factors, they can act as templates for the formation of new tissue. They aim to mimic the natural 3D microenvironment of the cells in order to facilitate cell proliferation and ECM deposition [79]. Basic scaffold prerequisites, materials used in bone TE, and scaffold geometries are discussed in the following chapter.

### 1.3.1 Scaffold Prerequisites

As with all implantable materials, biocompatibility is a requirement which is often mentioned in connection to bone scaffolds. A broad definition of the term has been established by Williams in 1987 as 'the ability of a material to perform with an appropriate host response in a specific application' [80]. However, many different parameters dictate viability of the scaffold and should be considered separately.

Lack of toxicity is one of the most important scaffold prerequisites. Scaffold materials should not be toxic or elicit an immune response. One of the standard criterions examined in this regard is the absence of leachable endotoxins [81].

Biodegradability is also a significant parameter. Ideally, once implanted, the TE scaffold should start to degrade at a controlled rate in accordance with the growth of newly formed tissue. The functions, such as mechanical stability, carried out by the scaffold are thus steadily replaced by the new tissue. Degradation rates must be fine-tuned depending on location of the defect and preferably even on patient specific factors, such as age. Additionally, all degradation products and byproducts must be non-toxic [4].

Mechanical properties of the scaffold, such as compressive strength and stiffness, are designed to closely match the mechanical properties of native tissue. The scaffold should be strong enough to replace the load bearing function of the missing bone, while not too stiff to induce bone loss or secondary fractures due to stress shielding [3], [4]. Especially for ceramics, fracture toughness, brittleness, and resulting scaffold reliability need to be well-defined. Furthermore, factors such as cell migration and stem cell differentiation are affected by the scaffold stiffness [82].

Scaffold permeability is a factor which can reduce the mechanical strength, but which is just as vital to *in vivo* success of the implant. Interconnected porosity is essential for transportation of nutrients and waste products as well as for neo-vascularization and cell migration [3], [4].

For bone scaffolds, osteoconduction, osteoinduction, and osteointegration are relevant concepts as they describe desired properties in bioactive scaffolds. Osteoconduction refers to the ability of a

scaffold to allow cells to adhere, proliferate, and form ECM components, *i.e.* for bone to grow on the surface. Osteoinduction takes matters a step further through recruitment of progenitor cells, stimulation of their differentiation, and induction of new bone formation. Finally, direct bone formation on the scaffold, without growth of fibrous tissue at the interface, and stable anchorage of the implant is referred to as osseointegration [83], [84].

### 1.3.2 Scaffold Materials

Different materials including metals, polymers, ceramics, and their composites have been investigated for bone TE scaffolds.

Porous metallic scaffolds made from iron, titanium or tantalum, such as foams, have adequate compressive strengths and are fatigue resistant. However, they are not biodegradable and can release potentially toxic ions [83]. Resorbable magnesium scaffolds have also been investigated and, although their preparation is still problematic due to the flammable nature of magnesium, they show promise [85].

A plethora of different polymeric materials are available for TE scaffolds. Natural polymers based on for example hyaluronic acid, chitosan, or collagen have excellent biological properties. Their low mechanical strengths and limited control over degradation rates are, however, detrimental [86]. Synthetic polymers such as polylactic acid, polycaprolactone, polyether ether ketone, and many more can be manufactured with highly reproducible and tunable properties. Although cellular interaction is not as advantageous as for natural polymers, modification for instance to encompass cell binding moieties can be carried out [87].

Bioactive glasses can be silicate, phosphate, or borate-based glasses and partially dissolve upon implantation. The released ions are beneficial to osteo- and angiogenesis. An amorphous calcium phosphate (ACP) or HA layer is formed on their surface, facilitating bonding to surrounding tissue. Limitations include low strength and brittleness [88].

The most commonly used ceramic scaffold materials are based on calcium phosphates. HA ($Ca_5(PO_4)_3$)OH) is considered as most similar to the mineral phase in bone and is the least soluble of the discussed calcium phosphates. It is considered as osteoconductive and in its stoichiometric and crystalline form, as non-resorbable. Its solubility and bioactivity can, however, be readily influenced by introducing ionic substitutions. Beta tricalcium phosphate (β-TCP, $Ca_3(PO_4)_2$) is more soluble than HA in aqueous conditions and is osteoinductive as well as osteoconductive [89]. α-TCP has also been considered as a biomaterial, but due to its extremely fast resorption rate or hydrolysis to calcium deficient HA in physiological conditions, the applications have been limited [90].

While reported compressive strengths of these calcium phosphates span from 5 - 500 MPa [64], making a comparison problematic, TCP scaffolds have the tendency of lower mechanical properties than their HA counterparts [91].

These factors warrant the use of biphasic calcium phosphates (BCP), which are a combination of HA and β-TCP. Through variation of the phase ratios, regulated resorption kinetics and controlled bioactivities can be attained [92].

ACPs are also employed in scaffolds for bone TE and have a wide range of Ca/P ratios, often encompassing many different ionic substitutions. This leads to high solubility and a correspondingly elevated biological activity. At extremely fast dissolution rates, however, local changes in pH can negatively affect cell viability [89].

Composite materials aim to combine properties of different material classes. For example, the high compressive strength and E-modulus of ceramic components in association with ductility and toughness of polymers can yield a reinforced material with adequate mechanical properties at

sufficient reliability. Cellular interaction can also benefit from composites, for example through coating of inert iron foams with bioactive calcium phosphates [93].

### 1.3.3 Scaffold Architecture

As briefly mentioned above, interconnected porosity of the bone scaffold is essential for its success but affects biological activity and mechanical integrity of the scaffold alike. Porosity, pore size, and even pore shape should all be taken into account when designing the scaffold.

Scaffold porosity is crucial for vascularization and migration as well as proliferation of cells [3], [4]. Differentiation is also a factor influenced by macroscopic pore percentage [94]. However, with increasing porosity, mechanical strength decreases [64]. It is thus necessary to find a compromise between biological activity and scaffold stability.

Pore size is the second, decisive parameter in the geometry of bone TE scaffolds. It has been shown that pore diameters of larger than 100 µm are necessary for diffusion of nutrients and, therefore, for cell survival. At smaller pore sizes, only unmineralized osteoid and no bone formation can be found [95]. Dimensions of more than 250 µm are necessary for sufficient vascular ingrowth [96]. When vascularization is not adequate due to small pores or limited interconnectivity, low oxygen concentrations lead to chondrogenesis over osteogenesis [97]–[99]. Although pores larger than 400 µm have been suggested to be optimal for vascularization [100], [86], a general consensus has emerged in literature, favoring pores of 300 - 400 µm diameter [99], [101]–[103]. A bimodal pore distribution with additional smaller pores in the range of 0.5 - 8 µm, or pore-wall roughness, has been shown to be beneficial to osteoconduction and the induction of bone formation [104]–[106].

When regarding the pore shape, it has been established that nanoscale topography affects cell behavior [107], [108]. Moreover, mm sized surface curvature also has an effect, as concave surfaces on scales larger than the cell have been shown to increase tissue growth rates [109], [110].

#### *Mechanical Considerations*

From a mechanical point of view, when porosity and pore size are predetermined due to the biological requirements of the scaffold, pore shape remains an adjustable parameter.

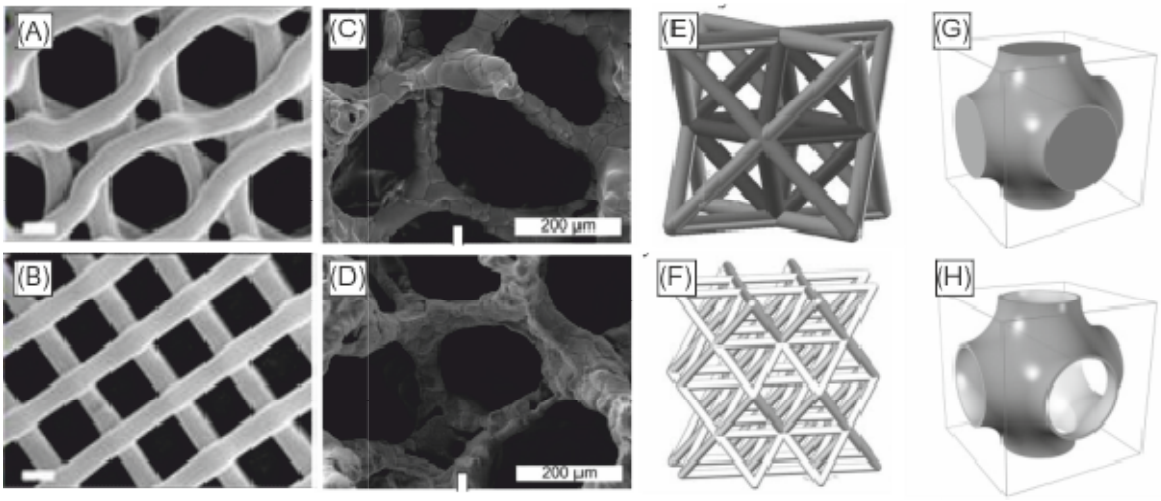


*Figure 6: (A),(B): scanning electron microscope (SEM) images of hexagonal and rectangular extrusion based scaffolds, reprinted from* [112]*. (C), (D): SEM images of cellular foam scaffolds, reprinted from* [113]*. (E), (F): computer aided design (CAD) drawing of octagonal truss-type unit cell and structure, modified and reprinted from* [117]*. (G), (H): CAD drawing of Schwarz primitive triply periodic minimal surfaces (TPMS) unit cell and corresponding shellular TPMS unit cell, modified and reprinted from* [118]*.*

Many scaffolds are fabricated by stacking individual porous layers, which, in turn, are formed by extruding lines on top of each other [111]. In that case, hexagonal pore architectures (Figure 6 A)

have presented superior mechanical properties than their rectangular counterparts (Figure 6 B) [112].

The formation of foams is another scaffolding approach to attain cellular structures (Figure 6 C and D) [113], [114]. Although these scaffolds have interconnected, open porosity, their geometries are not precisely defined. Additionally, their low nodal connectivity leads to bending dominated deformation [115], which decreases compressive strength especially for structures with high porosity [116].

Different periodic truss structures, which are constructed of struts and nodes (Figure 6 E and F), have been studied and certain criteria needed for increased compressive strengths have been identified. Rigid scaffolds with stretching dominated, as opposed to bending dominated, deformations are advantageous. This is the case when enough struts connect each of the scaffold nodes, *i.e.* when Maxwell's criterion for static determinacy is fulfilled [115]. High nodal connectivity is, furthermore, beneficial as it reduces the scaffolds sensitivity to defects [119]. Nano-scale hollow truss structures have also been fabricated [119], [120] and show great potential, as even ceramic scaffolds can exhibit a degree of ductility [121].

Triply periodic minimal surfaces (TPMS) have gained consideration as possible scaffold architectures with sufficient permeability at acceptable mechanical compatibility [122]. Furthermore, their biomimetic morphologies show promise in TE applications [123]. In these geometries, the solid/void interfacial surface is derived from a mathematical function with constant mean curvature and locally minimized surface area [124]. The Schwarz primitive structure (Figure 6 G), has the highest stiffness and strength when compared to other TPMS structures [125]. Even superior properties have been predicted for so-called shellular TPMS [126], where the solid phase is generated by adding material thickness to the interfacial surface, creating two interpenetrating porous networks (Figure 6 H) [118].

## 1.4 Tricalcium Phosphate

The material employed in this study, β-TCP ($Ca_3(PO_4)_2$), can be seen as a solid solution of CaO with 25 mol % $P_2O_5$. Three allotropic forms are shown in the phase diagram displayed in Figure 7. The low temperature modification, β-TCP, crystallizes in the hexagonal R3c space group and is stable until 1125 °C. Above that, the α-TCP phase with a monoclinic $2P_1/c$ crystal system is formed. The stable modification from 1470 °C to the congruent melting point at 1810 °C, is α'-TCP with a hexagonal $P6_3/mmc$ structure [127]. Additionally, a high-pressure modification, γ-TCP exists. The latter two forms are not stable under physiological conditions and thus not relevant for medical applications.

HA is often present in TCP powders due to the synthesis process. In the pure phase diagram, however, it is not a stable component, as HA requires the presence of water. Only then does it occur at a Ca/P ratio of 1.667. During sintering, it can dissociate once more to form TCP and tetracalcium phosphate (TTCP) [128].

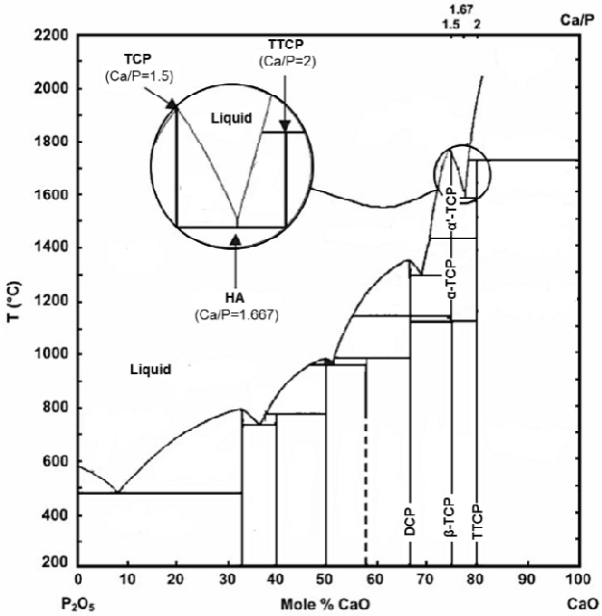


*Figure 7: Phase diagram of $P_2O_5$ and CaO at ambient pressure. DCP = dicalcium phosphate. Adapted from* [129].

Typical sintering temperatures of TCP range form 1100 - 1300 °C to assure sufficient densification, which is often above the reversible β - α transition temperature. In that case, the density difference of the 2 polymorphs can be problematic. β-TCP has a crystallographic density of 3.067 g $cm^{-3}$, whereas α-TCP is less dense at 2.863 g $cm^{-3}$. Especially for materials with coarse microstructures, stresses during expansion and contraction could thus lead to microcrack formation. Sintering at 1200 °C for short time periods of 1 - 3 h can retain small grain sizes and avoid the formation of microcracks even above the transition temperature [130].

### 1.4.1 Tricalcium Phosphate Synthesis

Common synthesis methods for TCP include the sol-gel approach, wet chemistry, and mechanosynthesis. Sol-gel can be applied for instance to synthesize TCP coatings for prosthetics or nanosized powders. Trimethyl phosphate ($(CH_3O)_3P$) and calcium nitrate tetrahydrate ($Ca(NO_3)_2*4H_2O$) are well-established P and Ca sources respectively, which can form HA, TCP, or BCP, depending on their ratio [131]. Wet chemistry approaches for applications in bone cements can be based on the reaction of calcium nitrate tetrahydrate with phosphoric acid. By setting the pH, formation of TCP as opposed to HA can be controlled [132]. Another method is mechanosynthesis, where precursors such as CaO and $P_2O_5$ are milled together in stochiometric

ratios. After a reaction time of several hours, amorphous TCP is attained, which can subsequently be annealed for crystallinity [133].

# 2. Objectives

The aim of this master thesis is the creation of novel TCP scaffolds for bone TE by means of DLP based SLA. Classification of the individual objectives can be implemented in four sections: creation of the scaffolds, validation of the manufacturing process, scaffold screening, and 3D cell culture.

As permeability is a vital factor for any TE scaffold, the prerequisite of interconnected porosity must be given. Conversely, high mechanical strength is necessary to comply with the load bearing function of bone. The present approach to achieve suitable mechanical properties while retaining high porosity, is utilization of additive manufacturing to precisely select pore architectures.

For this, four distinct scaffold geometries over a range of three different porosities at constant pore sizes are designed and manufactured at Lithoz GmbH by use of their ceramic manufacturing system. Validation of the manufactured scaffolds encompasses material characterization and evaluation of geometrical accuracy.

Archimedean density as well as bulk compressive strength and microstructure properties according to scanning electron microscopy (SEM) are determined and give indication of the efficacy of debinding and sintering procedures. Furthermore, XPS and powder XRD analysis are used to assess purity of TCP even after contact with organic binder material during the DLP process. Specimens are measured in µ-CT to analyze their topological dimensions within the scaffolds and on their surfaces, appraising effects of shrinkage or excessive polymerization.

Scaffold screening is implemented to evaluate mechanical properties and biological activity. Compressive strength as well as the apparent stiffness of the scaffolds are determined and compared to those of bone. Their resorptive properties are analyzed by monitoring of response to simulated body fluid (SBF) by utilization of µ-CT and SEM images. Considering these factors, the two most suitable architectures are identified and employed for further optimization.

With these optimized scaffolds, cell viability and osteogenic differentiation is assessed by 3D cell culture methods. Mouse pre-osteoblastic MC3T3-E1 cells are cultured on the scaffolds and DNA is quantified, metabolic activity measured, and cell adhesion visualized through staining. Osteoblast maturation is analyzed by indications of ALP activity and ECM formation and mineralization by quantification of collagen and calcium deposition on the scaffolds.

Finally, taking into account the identified advantages and weaknesses of the individual scaffolds, a suggestion of the most favorable scaffold geometry is made.

# 3. Experimental

The following chapter describes the experimental procedures employed in the present thesis. An overview thereof is given in Table 1.

*Table 1: Overview of utilized methods with location of implementation and name of instrument operator if applicable.*

| **Task** | **Chapter** | **Instrument and Software** | **Location** |
|---|---|---|---|
| **Scaffold Design** | 3.1 | - Autodesk Meshmixer 3.3-<br>- Autodesk Netfabb 2019<br>- Simpleware CAD, Synopsys inc.<br>- SOLIDWORKS 2017 SP03 | University College London (UCL)<br>Institute of Orthopedics and<br>Musculoskeletal Sciences (IOMS) |
| **Manufacturing** | 3.2 | - Lithoz CeraFab 7500 system | Lithoz GmbH, Vienna |
| **Analysis** | 3.3 | | |
| Density | 3.3.1 | - Sartorius kit YDK 01 | Lithoz GmbH, Vienna |
| µ-CT | 3.3.2 | - Bruker Skyscan 1172<br>- NRecon software (Bruker) | UCL, Dep. of Cell and<br>Developmental Biology |
| Compression | 3.3.3 | - ZwickRoell Z005 | UCL, IOMS |
| Powder XRD | 3.3.4 | - Stoe STADI-P<br>- FullProf software [138] | UCL, Dep. of Chemistry<br>by Dr Martin Vickers |
| XPS | 3.3.5 | - ThetaProbe MKII, Thermo Scientific<br>- CasaXPS software | UCL, Dep. of Chemistry<br>by Dr Robert Palgrave |
| SEM | 3.3.6 | - JEOL JSM-6301F | UCL, Dep. of Chemistry |
| **Cell Culture** | 3.4 | | UCL, IOMS |

## 3.1 Scaffold Architectures

Four different scaffold architectures, a cylinder grid, a Schwarz primitive, a hollow Schwarz primitive and a Kagome structure were designed. For each of these, three different porosities, 25 %, 50 %, and 75 %, were chosen with constant pore sizes. All measurements of porosities are given in volume % (vol.%). After screening of these initial designs, a second, optimized array of geometries of grid and Kagome structures at 50 % and 75 % porosity was created. The precise parameters are listed in Table 2 and STLs are presented in Figure 8.

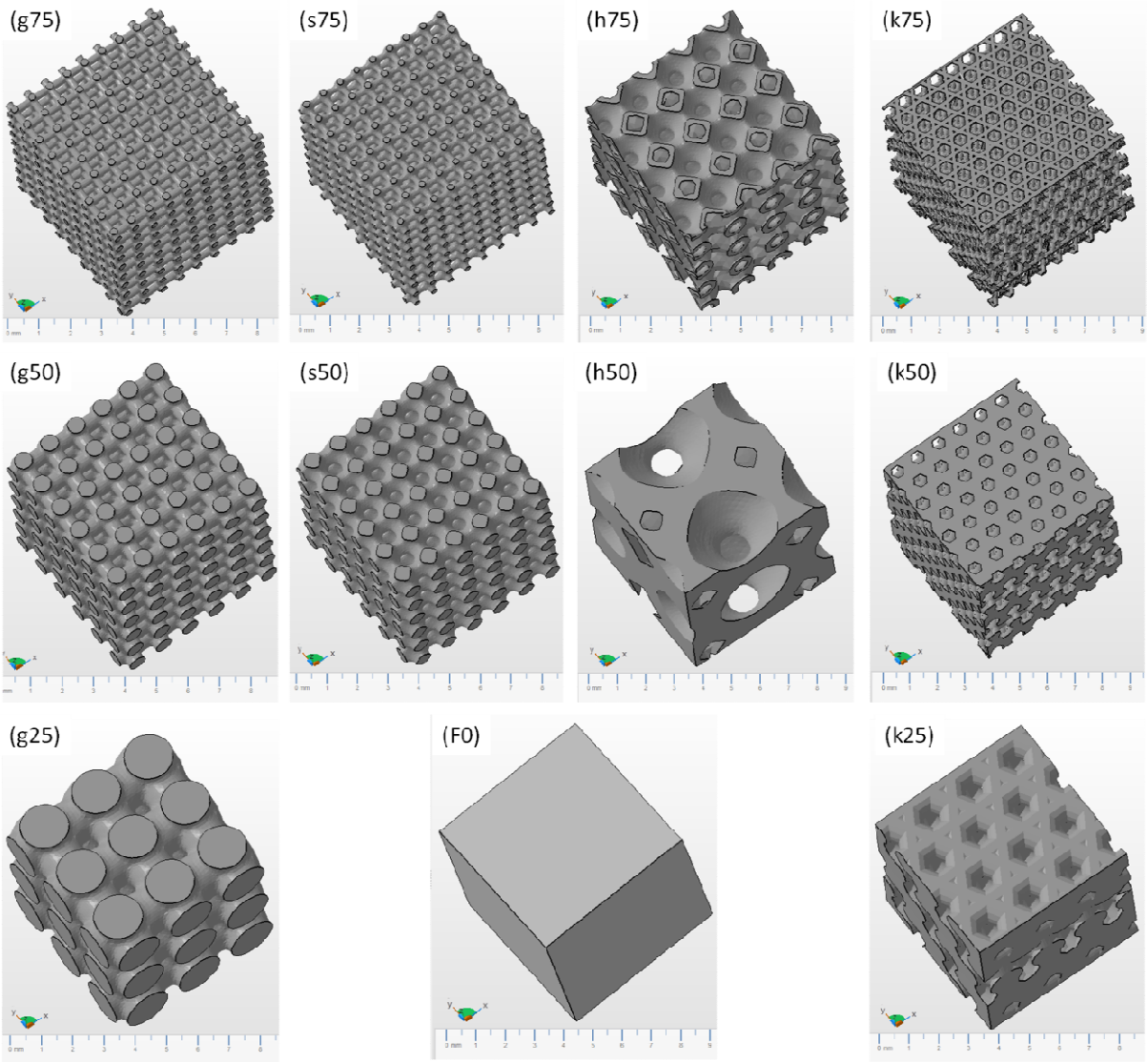


*Figure 8: STL files visualized in Autodesk Netfabb Premium 2019. Designations in bracket represent structure geometries, compare Table 2.*

The grid structure was designed using the Simpleware CAD module (Synopsys®, Inc.). After importing the STL file of the shape *e.g.* a 6x6x6 mm cube, the internal structure wizard was applied. Unit cell type was set to cylinder grid without a shell and the parameters of unit cell size and infill were chosen.

Analogously to the grid structure, the Schwarz primitive was created with the unit cell type being set to Schwarz primitive (pinched). The 25 % porous structure was omitted as it would not have had interconnected porosities.

The Hollow Schwarz structure was created from a regular Schwarz geometry, which was modified in Autodesk Meshmixer 3.3 with the hollow function to create a shell-like structure. As with the Schwarz geometry, the 25 % porosity was not attainable.

Finally, the Kagome architecture was designed in SOLIDWORKS 2017 SP03 by sketching of a Kagome unit cell according to [134], using the swept boss/base function to create trusses, and propagation with the linear patterns function until final geometry of the part is reached. In order to attain correct porosities at constant pore sizes, the truss thickness and scale factors were varied respectively. A regression of these parameters is given in Appendix 1.

The optimized scaffolds were created analogously, with an additional linear scaling factor for porosity and pore size to account for over-polymerization. The factor was attained from previous µ-CT measurements of the screened scaffolds and yielded values listed in Table 2. Assigned structure names consist of a letter for the structure type and a number representing porosities. Optimized structures are designated with capital letters.

All structures were treated with additional scaling factors provided by Lithoz of 1.267 in x and y direction and 1.281 in z direction to account for shrinkage during thermal treatment.

*Table 2: Parameters of the STLs of created geometries. Numbers in parentheses refer to desired final dimensions after accounting for over-polymerization.*

| Name | Structure type | Porosity [%] | Unit cell size [µm] | Pore Size [µm] |
|---|---|---|---|---|
| **F0** | N.A. | 0 | N.A. | N.A. |
| **g75** | Cylinder Grid | 75 | 690 | 460 |
| **g50** | Cylinder Grid | 50 | 1030 | 475 |
| **g25** | Cylinder Grid | 25 | 2000 | 450 |
| **s75** | Schwarz primitive | 75 | 690 | 460 |
| **s50** | Schwarz primitive | 50 | 1030 | 460 |
| **h75** | Hollow Schwarz | 75 | 1450 | 500 |
| **h50** | Hollow Schwarz | 50 | 4000 | 500 |
| **k75** | Kagome | 69 | 500 | 600 |
| **k50** | Kagome | 56 | 521 | 540 |
| **k25** | Kagome | 30 | 850 | 540 |
| **G75** | Cylinder Grid | 83 (75) | 640 | 475 (400) |
| **G50** | Cylinder Grid | 59 (50) | 880 | 475 (400) |
| **K75** | Kagome | 80 (75) | 340 | 460 (400) |
| **K50** | Kagome | 54 (50) | 470 | 460 (400) |

## 3.2 Manufacturing Parts

### 3.2.1 Slurry Characterization

All handling of liquid non-cured slurry was carried out in yellow light conditions. Penetration depth of the TCP slurry, which was provided by Lithoz, was measured by irradiating 10 mm diameter circles in a 1 mm thick slurry film for 2 s at 100 mW $cm^{-2}$. Gray scale exposure ensured energies ranged from 200 to 75 mJ in steps of 25 mJ and from 100 mJ to 37.5 mJ in steps of 12.5 mJ. All energy stages were measured at least in triplicates. After removal of uncured slurry with a cleaning agent provided by Lithoz, thickness of the disks were measured with the help of a thickness gauge.

For data analysis, cure depths were plotted against exposure energy and a logarithmic regression was implemented. Depth of penetration and critical energy could then be obtained from the working curve in Equation (2) [135].

$$C_d = D_p ln\left(\frac{E_p}{E_c}\right) \quad (2)$$

$C_d$ … *Cure depth [µm]*
$D_p$ … *Penetration depth [µm]*
$E_p$ … *Exposure energy [mJ $cm^{-2}$]*
$E_c$ … *Critical energy [mJ $cm^{-2}$]*

### 3.2.2 Manufacturing

A Lithoz CeraFab 7500 system was used to create the TCP scaffolds. The setup is a constrained surface DLP system with an LED radiation source in the blue visible region. Prior to manufacturing, the building platform was coated with adhesive agent R31 provided by Lithoz. In order to assure parallelism between building platform and vat, a first layer covering the entire building area was cured.

The most important parameters are summarized in Table 3. The starting layers have slightly different parameters to ensure adequate adhesion to the building platform and to avoid formation of air bubbles.

*Table 3: most vital manufacturing parameters*

| **Universal parameters** | **Value** | |
|---|---|---|
| Pixel size | 40 µm | |
| Layer height | 25 µm | |
| Ambient temperature | 28 - 30 °C | |
| Shrinkage compensation (xy) | 1.267 | |
| Shrinkage compensation (z) | 1.281 | |
| **Layer dependent parameters** | **Value first 5 layers** | **Value main layers** |
| Slurry layer thickness | 125 - 150 µm | 200 - 250 µm |
| Exposure energy | 150 mJ | 110 mJ |
| Waiting time before exposure | 15 s | 3 s |
| Vat tilting steps | 2 | 1 |
| Tilting down velocity | 3 steps $s^{-1}$ | 5 steps $s^{-1}$ |
| Tilting up velocity | 10 steps $s^{-1}$ | 16 steps $s^{-1}$ |

18 of the samples with 6x6 mm base area were created in one job. For the 5x5 mm samples, 24 specimens fit on one building platform when spacing of 6 mm was selected. The geometries were mixed over different runs to exclude factors of variation between jobs, as displayed in Figure 9.

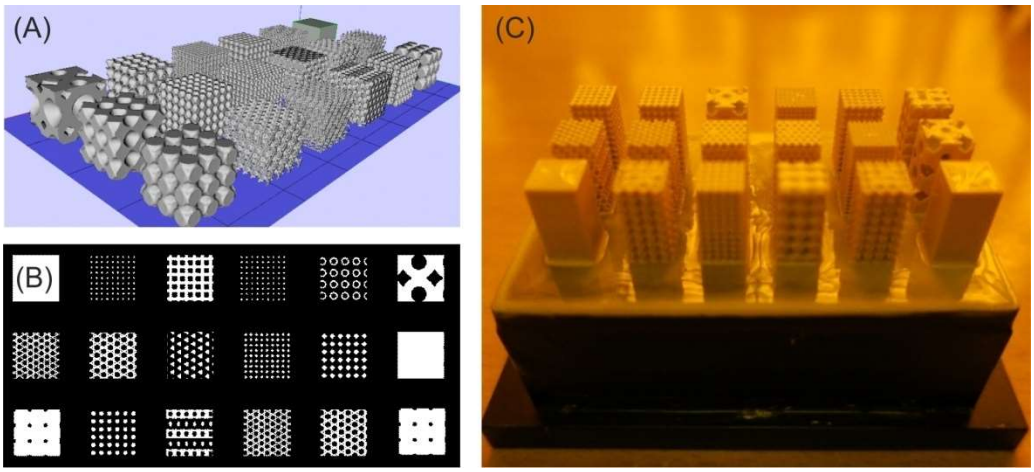


*Figure 9: A variety of building platform setups. (A): CAD view, (B): One layer preview, white indicates illumination and black the absence thereof, (C): Green parts before post processing.*

### 3.2.3 Post-processing

Green samples were removed from the building platform by use of a razor blade. Cleaning of uncured slurry was implemented by a cleaning agent provided by Lithoz in combination with application of pressurized air. Samples were post-cured in a UV chamber for 2 min and stored at 30 °C for no longer than 5 days prior to thermal treatment.

### 3.2.4 Thermal Treatment

Debinding and sintering of the green samples was carried out in a Nabertherm P330 oven. The total program takes 96 h and maximum temperatures of 1200 °C are held for 2 h, see Figure 10 for the exact temperature rates, which vary between 0.17 and 0.52 °C $min^{-1}$.

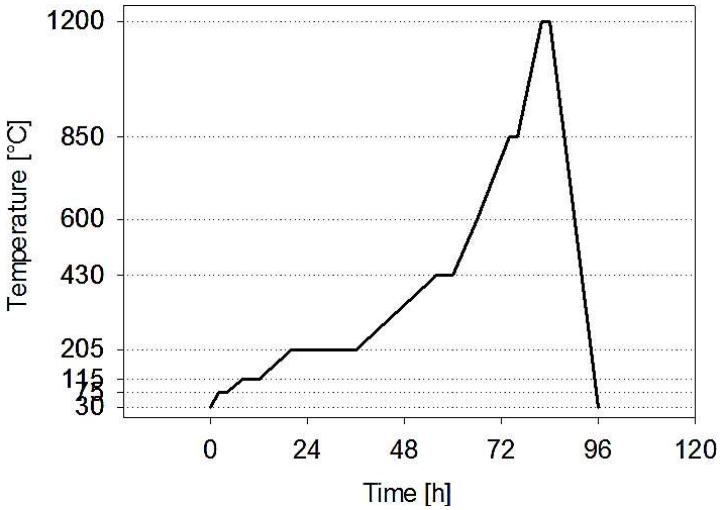


*Figure 10: Temperature program for debinding and sintering of green parts*

## 3.3 Analysis of Manufactured Scaffolds

### 3.3.1 Archimedean Density

A Sartorius density determination kit YDK 01 was used to measure densities of sintered ceramic parts. The specimens were weighed on an analytical balance; the average of 5 measurements was taken to determine the weight in air. The weight in water was attained by taking the average of 5 measurements of the submerged parts. A drop of soap had been added to the water to reduce surface tension and by extent air-bubble formation. Water temperature was measured by a thermometer in order to discern its density. The densities of the sintered parts were calculated using Equation (3).

$$\rho(s) = \frac{W(a) \cdot [\rho(l) - \rho(a)]}{0.99983[W(a) - W(l)]} + \rho(a) \quad (3)$$

*ρ(s)* … *Density of the solid [g cm$^{-3}$]*
*ρ(left)* … *Density of the liquid [g cm$^{-3}$]*
*ρ(a)* … *Density of air [g cm$^{-3}$]*
*W(a)* … *Weight of the solid in air [g]*
W(left) … *Weight of the solid in liquid [g]*

### 3.3.2 Micro Computed Tomography

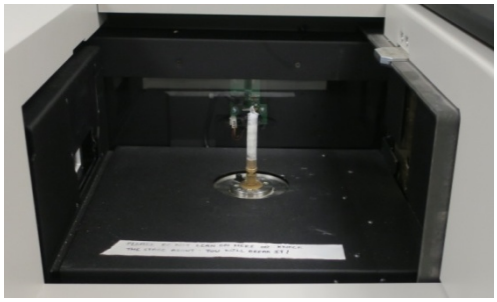

*Figure 11: Setup of the µ-CT measurement chamber*

A Bruker Skyscan 1172 micro-CT apparatus (Department of Cell and Developmental Biology, UCL) was used for analysis of the 6x6x6 mm porous cubes. Four cubes were measured in each scan and immobilization in the measuring tube was achieved by use of a transparent polymer foil, see Figure 11 for the setup. A 0.5 mm aluminum filter was employed, voltage was set to 50 kV and 200 µA current was used. Averages of 4 frames were taken at 0.5° radiation steps and pixel sizes of 9 µm.

*Table 4: µ-CT processing parameters in CT-Analyser software*

| Order | Task | Parameters |
|---|---|---|
| **1.** | Median filtering | Radius = 4 |
| **2.** | Global thresholding | 23 % of maximum grey scale value |
| **3.** | Despeckle black | 50 pixels |
| **4.** | Despeckle white | 50 pixels |
| **5.** | 3D analysis | |

The NRecon (Bruker microCT) software was employed for reconstruction of the data. Histogram ranges were set to values of 0 - 0.2 and ring artifact reduction to a value of 5. Unit cells and pore sizes were measured from these raw images at different locations within the scaffolds: in xy-planes perpendicular to the z axis, in xz and yz planes, in the centre of the specimens and at their surfaces.

Repetitions of four measurements were taken at each of these positions. Surface to volume ratios and porosities were determined after processing in CT-Analyser 1.13 (Bruker-microCT). The volumes of interests were chosen to only include complete unit cells. The parameters are listed in Table 4 and an example slice is depicted in Figure 12.

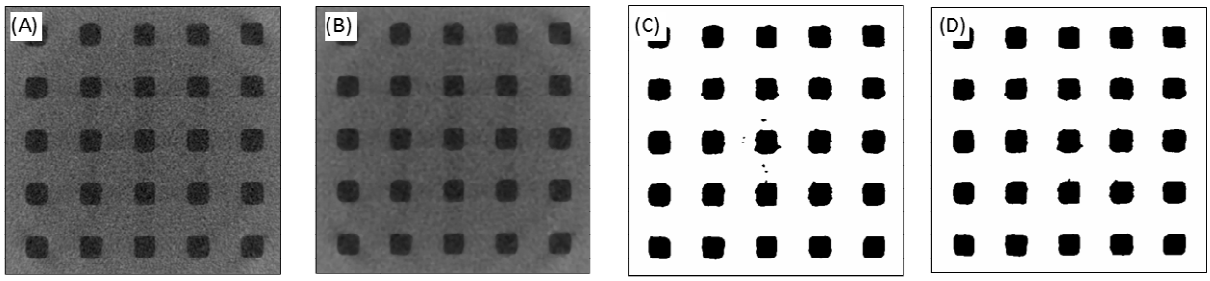


*Figure 12: Example of the image processing procedure in CTAn. (A): raw image; (B): after filtering; (C): after thresholding; (D): after despeckling*

### 3.3.3 Compression tests

An in-house ZwickRoell Z005 compression machine was utilized to measure compressive strength of scaffolds. According to ASTM standard D695-15 [136], crosshead speed was set to 1.3 mm $min^{-1}$. The samples were rectangular prisms with dimensions of 6x6x12 mm unless stated otherwise and at least 6 replicates were measured as fired; 20 replicates were analyzed for the second set of samples. A pre-load of 10 N was applied prior to compression.

The apparent elastic modulus was determined by measuring the slope of the steepest initial, linear portion of the stress-strain diagram through application of a linear regression. The compressive strength of the individual samples was discerned by taking the peak strain value and normalizing it to the cross-section area of the test specimen prior to compression.
Weibull analysis was carried out for specimens where at least 18 data points were available [137]. The results were sorted by ascending value and plotted as $\ln(\sigma_i)$ against $\ln[\ln(1/(1-F(\sigma_i)))]$ where $\sigma_i$ is the compressive strength in MPa and $F(\sigma_i)$ is the fracture probability of each data point, see Equation (4)

$$F(\sigma_i) = \frac{i - 0.5}{n} \quad (4)$$

$F(\sigma_i)$ … *Fracture probability*
$i$ … *Ascending sample rank*
$n$ … *Number of test specimens*

The slope of the calibration function in the Weibull plot is the Weibull parameter $m$ and the axial intercept is the strength at failure $\ln(\sigma_0)$. The Weibull strength $\sigma_{WB}$ can be calculated according to Equation (5).

$$\sigma_{WB} = e^{\frac{\sigma_0}{m}} \quad (5)$$

### 3.3.4 Powder X-ray Diffraction

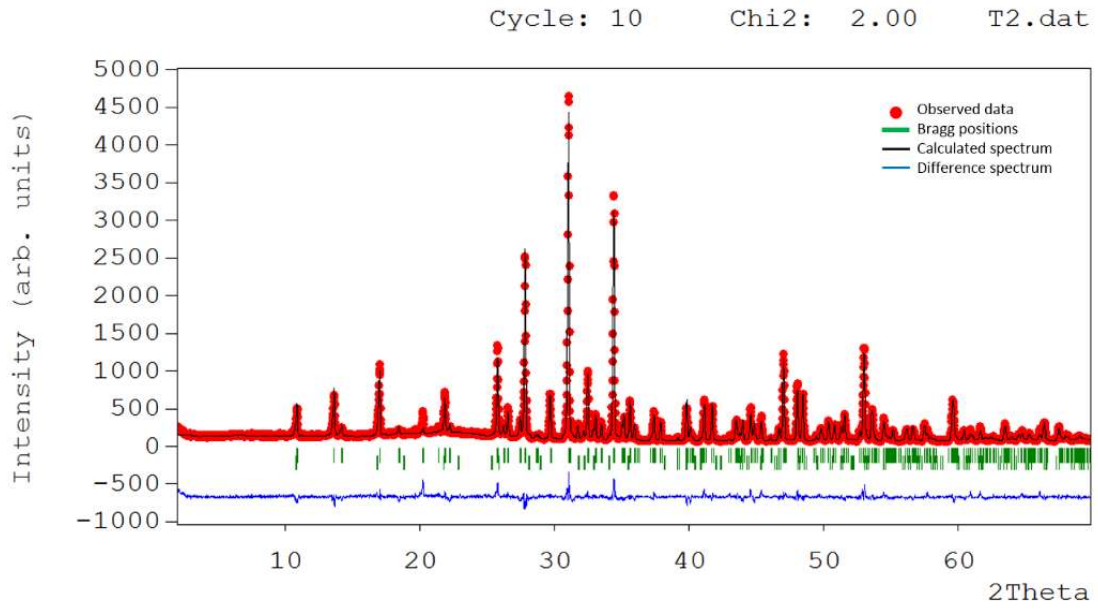


*Figure 13: Example of Rietveld refinement using FullProf*

Samples were prepared by crushing with pistil and mortar until a fine, homogeneous powder was attained and filled into a 0.3 mm capillary. Powder XRD data were then measured on a Stoe STADI-P system (Department of Chemistry, UCL) in transmission mode with Cu Kα1 irradiation. 2 θ scan range was 2.000 - 69.815° with 0.495° steps at 10.0 s/step. The FullProf [138] software was used for data analysis. Starting parameters for β-TCP were taken from [139] and for HA from [140]. Refined parameters are listed in Table 5 and an example of the refinement is displayed in Figure 13.

*Table 5: Rietveld refinement parameters for powder XRD using the FullProf software*

| Order | Task | Parameters |
|---|---|---|
| **1.** | Background | Linear interpolation between background points |
| **2.** | Scale factor | 1 parameter |
| **3.** | Unit cell | 2 parameters (a, c) |
| **3.** | Peak shape | 3 parameters (U,V,W), Pseudo Voigt |
| **4.** | Asymmetry | 2 parameters below 2 θ = 30°, |
| **5.** | 2nd phase | Same procedure as phase 1 |

### 3.3.5 X-ray Photoelectron Spectroscopy

XPS measurements were carried out on a ThetaProbe MKII spectrometer (Thermo Scientific, Department of Chemistry, UCL) with Al $K_\alpha$ radiation and an electron/ion flood gun for charge compensation. Samples were crushed with pistil and mortar to attain a homogeneous powder and were measured before and after 2 min of argon-ion etching to remove adventitious carbon. For high resolution scans a pass energy of 50 eV at steps of 0.100 eV were chosen and total acquisition time amounted to 4.5 min. XPS peaks were calibrated using the C 1s line at 284.8 eV and analysis was carried out using the CasaXPS software.

### 3.3.6 Scanning Electron Microscopy

SEM images were created on a JEOL JSM-6301F system (Department of Chemistry, UCL) after gold plasma coating for 1.5 min at 20 mA and fixation of a copper wire from sample surface to carrier plate to ensure conductivity, compare Figure 14. 5.0 kV were applied at working distances of 7.5 – 8.0 mm.

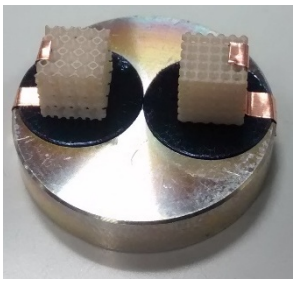

*Figure 14: SEM sample preparation*

Average grain sizes were determined from the 1900 x magnified images by using a lineal intercept procedure. 10 lines were drawn over 3 images, each at a variety of angles, and interceptions with grain boundaries were counted. Grain size was attain according to Equation (6) [141].

$$D = 1.56\,\frac{C}{MN} \qquad (6)$$

*D* … *Average grain size [µm]*
*C* … *Length of test line [µm]*
*N* … *Number of intercepts*
*M* … *Magnification*

### 3.3.7 Simulated Body Fluid

SBF was prepared according to Kokubo [142] with ion concentrations as listed in Table 6. Final pH was set between 7.40 - 7.45. A triplicate of the different 6x6x6 mm scaffolds were weighed thrice and placed in 24 well plates. They were washed once with ethanol and twice with deionized water, prior to being completely submerged in SBF. The samples were stored at 37 °C for 7, 14, and 21 days.

After removal of SBF and rinsing twice with deionized water, the specimens were placed in an evacuated desiccator over silica gel for 72 h at 25 °C. The samples were then weighed three more times and stored in 24 well plates to await further analysis.

*Table 6: Composition of SBF according to Kokubo* [142]

| Order | Reagent | Amount (for 1 L SBF) | Ion | Concentration [mM] |
|---|---|---|---|---|
| **1** | NaCl | 8.035 g | $Na^+$ | 142 |
| **2** | $NaHCO_3$ | 0.355 g | $K^+$ | 5.0 |
| **3** | KCl | 0.225 g | $Mg^{2+}$ | 1.5 |
| **4** | $K_2HPO_4{\cdot}3H_2O$ | 0.231 g | $Ca^{2+}$ | 2.5 |
| **5** | $MgCl_2{\cdot}6H_2O$ | 0.311 g | $Cl^-$ | 148 |
| **6** | 1.0 M HCl | 39 ml | $HCO_3^-$ | 4.2 |
| **7** | $CaCl_2$ | 0.292 g | $HPO_4^{2-}$ | 1.0 |
| **8** | $Na_2SO_4$ | 0.072 g | $SO_4^{2-}$ | 0.5 |
| **9** | Tris | 6.118 g | | |

## 3.4 Cell Culture

Preosteoblast-like mouse cells, MC3T3-E1, were cultivated on the TCP scaffolds and differentiation to mature osteoblast-like cells was analyzed.

### 3.4.1 Culture of MC3T3-E1 Cells

Subclone 4 of MC3T3-E1 cells (CRL-2593; ATCC, UK) were cultured in Minimum Essential Medium without ascorbic acid (α-MEM; A10490-01; Thermo Fisher Scientific Inc., UK) supplemented with 10 % FCS as well as with 1000 U $mL^{-1}$ penicillin and streptomycin. Incubation conditions were 37 °C in 5 % $CO_2$ atmosphere.

225 $cm^2$ culture flasks were utilized and after reaching 70 % confluency, cells were passaged in a ratio of 1:6. For that purpose, aspiration of medium was followed by washing of the cells with 12 mL PBS and detachment from the flask with 12 mL of a 0.05 % trypsin/EDTA solution in PBS. After incubation for 2 min at 37 °C, trypsin was deactivated by addition of 12 mL medium. Transferral of 4 mL of this cell suspension to six new flasks and addition of medium to a final volume of 24 mL was followed by cultivation at 37 °C and 5 % $CO_2$. Medium was renewed every 2 - 3 days and 70 % confluency was reached after approximately 7 days.

### 3.4.2 Cell Seeding

48 well plates were used to seed $2.25*10^5$ cells at passage 3 per scaffold. Scaffolds were sterilized in 70 % ethanol for 1 h and rinsed with PBS. Additionally to the F0, G50, G75, K50, and K75 structures, two empty wells were seeded per time-point. One of these 2D cultivations was carried out, analogously to the scaffolds, in osteogenic medium and the other in the propagation medium α-MEM. Preparation of differentiation medium by dissolution of the individual components and then supplementing of α-MEM was implemented according to Table 7.

Nine repetitions were seeded for each of the four time-points. A cell suspension of $7.6*10^6$ cells $mL^{-1}$ was created and 30 µL of this suspension was carefully pipetted onto the scaffold centers or in empty wells. After resting at 25 °C for 15 min, 400 µL of α-MEM was added and the cells were incubated at 37 °C for 1 h. The remaining 500 µL of medium was then included and incubation at 37 °C and 5 % $CO_2$ for 12 h followed. Then, the scaffolds were transferred to clean wells in order to exclude any cells seeded on the well floors and the medium was replaced with osteogenic medium. Only one of the 2D conditions remained in fresh α-MEM. Subsequently, medium was changed every 2 - 3 days.

*Table 7: Preparation of osteogenic medium*

| Component | Solvent | Concentration in Solution | Final Concentration in Medium |
|---|---|---|---|
| **Dexamethasone** | Ethanol | 100 mM | 100 nM |
| **Ascorbic Acid** | α-MEM | 5 mg $mL^{-1}$ | 50 µg $mL^{-1}$ |
| **β-Glycerophosphate** | α-MEM | 1 M | 10 mM |

### 3.4.3 Cell Growth

For investigation of cell growth, DNA was quantified, metabolic activity analyzed, and cell nuclei as well as cytoskeleton were stained and imaged.

*DNA Quantification*

A Quanti-iT PicoGreen assay (P7589; Thermo Fisher Scientific Inc., UK) was utilized for DNA quantification according to the manufacturer's specifications. Briefly, cells were lyzed with 1 % Triton X-100 (Sigma Aldrich, USA) and after addition of the PicoGreen reagent, diluted 1:200 in the provided puffer solution, fluorescence was recorded with excitation at 480 nm and emission at 520 nm.

For quantification, a standard curve was prepared with MC3T3-E1 cells at passage 4. After seeding of cells in a 48 well plate in triplicates, 4 h incubation at 37 °C in 5 % $CO_2$ atmosphere ensured cell attachment. Subsequently, the assay was carried out, yielding a standard curve depicted in Figure 15. An $r^2$ of 0.998 was attained.

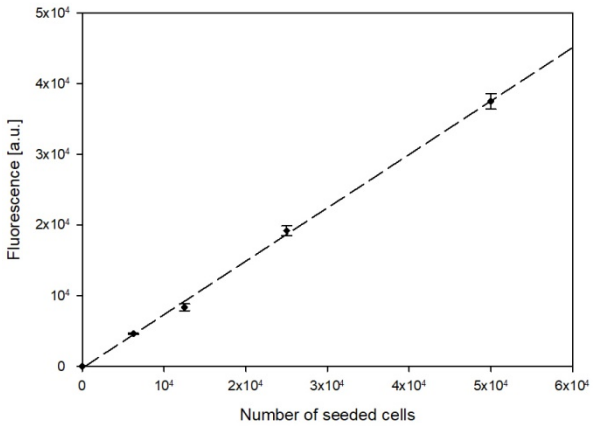


*Figure 15: Standard curve of DNA quantification with PicoGreen assay (n = 3; with standard deviation (st.dev.))*

*Metabolic Activity*

The PrestoBlue assay (A13262; Thermo Fisher Scientific Inc., UK) was carried out according to the manufacturer's protocol to ascertain metabolic activity. 900 µL of a 10 % solution of the reagent in α-MEM was added to the wells in triplicates and after 1 h incubation in the dark at 37 °C in 5 % $CO_2$ atmosphere, fluorescence was measured. Excitation was set to a wavelength of 560 nm and emission was read at 590 nm.

*Cell Staining*

After fixation of the samples in 4 % paraformaldehyde (PFA) for 30 min and washing with PBS, cells were permeabilized by exposure to 0.1 % Triton X-100 in PBS for 5 min. Another wash of the scaffolds was followed by blocking of the samples in 1 % BSA for 30 min.

F-actin filaments were stained by addition of 500 µL Alexa Fluor 594 phalloidin (A12381; Thermo Fisher Scientific Inc., UK) diluted 1:40 in PBS. Incubation in the dark at 25 °C for 40 min was followed by another washing step.

Counterstaining of DNA was carried out by 500 µL of a 1:50 dilution of 4',6-diamidino-2-phenylindole dihydrochloride (DAPI; D1306; Thermo Fisher Scientific Inc., UK) in PBS. After incubation for 10 min in the dark at 25 °C, a final washing step in PBS was followed by addition of 5 µL ProLong Gold Antifade mountant (P36930; Thermo Fisher Scientific Inc., UK).

The samples were kept in the dark at 8 °C until imaging using an in-house ApoTome.2 fluorescence microscope (Carl Zeiss Microscopy GmbH) could be implemented. Confocal microscopy was carried

out by taking images every 20 µm over a depth of 120 µm and images were processed in the ZEN 2 (Carl Zeiss Microscopy GmbH) software.

### 3.4.4 Differentiation and Mineralization Assays

Differentiation of the preosteoblasts was analyzed by regarding alkaline phasphatase (ALP) activity and quantifying collagen as well as calcium deposition on the scaffolds.

*Alkaline Phosphatase Activity*

The colorimetric Alkaline Phosphatase assay (ab83369; Abcam, UK) was used to measure ALP activity in the samples, according to manufacturer's specifications. Para-nitrophenylphosphate (pNPP) was employed as a substrate and optical density (OD) was recorded at 405 nm. The established standard curve with $r^2$ of 0.997 is shown in Figure 16.

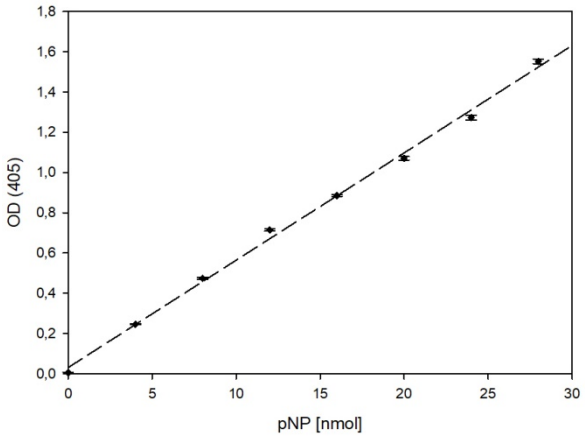


*Figure 16: Standard curve of ALP assay (n = 3; with st.dev.)*

ALP activity was calculated from the para-nitrophenol (pNP) amount according to Equation (7) and normalized to the cell number attained from DNA quantification.

$$ALP\ activity = 1.56\ \frac{pNP}{\Delta T * V} \qquad (7)$$

*pNP … Amount of pNP according to standard curve [µmol]*
*$\Delta T$ … Reaction time [min]*
*V … Volume of measured media [mL]*

*Collagen Quantification*

A Sircol Soluble Collagen assay (S1000; Biocolor, UK) was employed for quantification of total collagen. The assay was not feasible as suggested from the kit, because TCP dissolved in the provided isolation reagents and subsequently interfered with the measurements. Instead, an alternative protocol was used [143]. The specimens were fixed in methanol at -20 °C over night and after washing in PBS, exposed to 1 mL Sircol dye for 4 h at 25 °C. After washing thrice in PBS and two more times in 0.1 % acetic acid in PBS, images were taken with an in-house reflective light (Zeiss Stemi 508). 250 µL of the alkali reagent were added to the wells and the dye was dissolved by shaking for 1 h at 25 °C. Finally, 100 µL of the solution was placed in 96 well plates in duplicates and absorbance was measured at 555 nm. The previously determined standard curve with an $r^2$ of 0.992 is displayed in Figure 17.

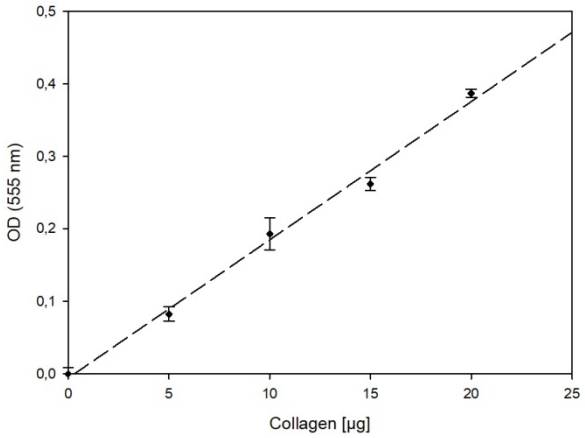


*Figure 17: Standard curve of collagen assay (n = 3; with st.dev.)*

*Calcium Deposition*

Calcium deposition was evaluated using Alizarin Red S (ARS) staining (#8678; ScienCell, UK) according to the manufacturer's protocol. Briefly, calcium was stained with the provided anthraquinone dye and after washing and taking images on the in-house reflective-light microscope (Zeiss Stemi 508), the dye was dissolved in 10 % acetic acid. Subsequently, the solution was neutralized with 10 % ammonium hydroxide and OD was measured at 405 nm. The standard curve for quantification is shown in Figure 18 and exhibits an $r^2$ value of 0.998.

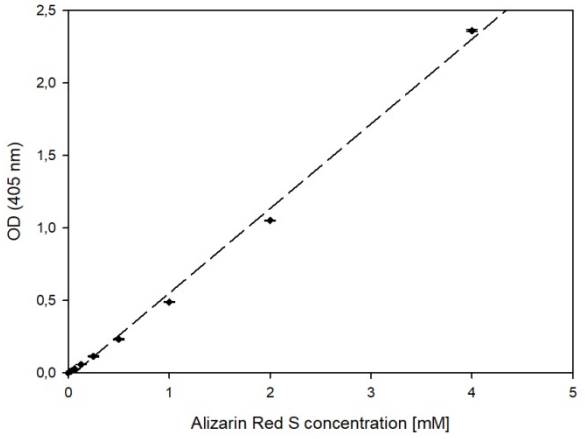


*Figure 18: Standard curve of ARS (n = 3; with st.dev.)*

### 3.4.5 Statistical Analysis

All values were analyzed after subtraction of negative controls. These were attained by characterization of clean scaffolds without cells, incubated in osteogenic media for the 3D conditions and by investigation of empty wells without cells, also in osteogenic media, for the 2D culture conditions. All data were taken from 3 sample replicates, measured in duplicates unless specified otherwise, and represented as mean ± standard deviation (st.dev.). Statistical significance was assessed using analysis of variance (ANOVA) (or the Student's t-test when only two cases were compared) in the SigmaPlot 12.0 software. At $P < 0.005$, statistical significance was declared and at $P < 0.001$, data were marked as highly significant.

# 4. Results and Discussion

## 4.1 Slurry Characterization

The TCP slurry provided by Lithoz is composed of β-TCP powder in a photocurable organic (meth)-acrylate-based binder system. In order to select the exposure energy of the irradiation, the interaction of the slurry with incident light needs to be analyzed.

One of the most important slurry parameters is cure depth ($C_d$), which determines resolution and accuracy of SLA processes; the smaller the $C_d$, the better the resolution [144]. However, a minimum is necessary to accomplish structuring and higher $C_d$ is beneficial for successful thermal processing of filled slurries. In DLP, a benchmark of 3 times the layer thickness can be chosen in order to assure sufficient layer cohesion [145].

Figure 19 A shows the working curve of the TCP slurry, according to Equation (2) [135]. At lower exposure energy, $C_d$ rapidly declines and, following the curve of the logarithmic regression, intercepts with the x-axis at the critical energy ($E_c$) of 24.2 mJ cm$^{-2}$. Below this material specific limiting energy, curing cannot take place. The second characteristic value, representing slurry reactivity, is the penetration depth ($D_p$) of 86.6 µm attained from the slope of the curve.

After consideration of these data and visual inspection of cured disks, as depicted in Figure 19 B, an exposure energy of 110 mJ cm$^{-2}$ was selected for the manufacturing process. This ensures more than adequate $C_d$ while avoiding unwanted phenomena such as over-polymerization.

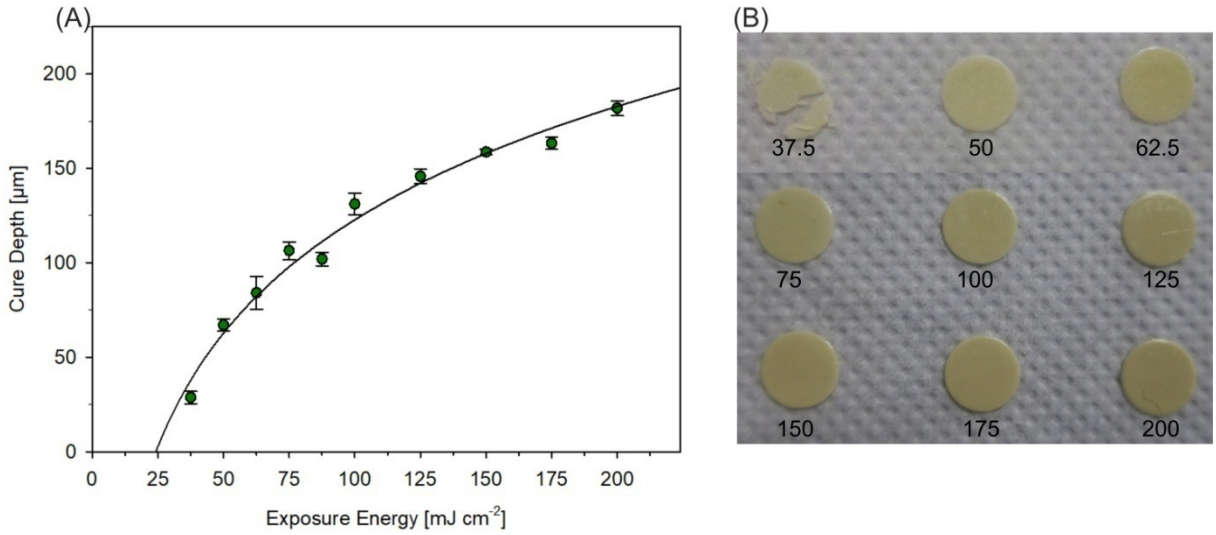


*Figure 19: (A): Working curve of TCP slurry; n = 3, with st.dev. (B): Slurry disks cured at a range of exposure energies, labeled in mJ cm$^{-2}$.*

## 4.2 Material Characterization

Bulk TCP cylinders were characterized in respect to density and compressive testing. Material purity and absence of binder residue was confirmed in XPS and a phase composition of pure β-TCP was found in powder XRD measurements of sintered samples. SEM imaging was utilized to study the microstructure of parts.

### 4.2.1 Bulk Density

Densities of monolithic parts were measured, as summarized in Table 8. The porous structures were not viable for measurement of Archimedean density, as air bubble formation inside the scaffolds could not be inhibited. Wall thickness did not have an effect on the final density of the manufactured parts, which are satisfactory at 98.0 - 99.5 % of the theoretical density of 3.065 g $cm^{-3}$ [146]. Consequently, one can infer that this range is universal to the manufactured TCP and also representative of the scaffold densities.

*Table 8: Densities of sintered TCP cubes with 0 % porosity at different wall diameters; with st. dev.; n = 5. Relative densities were attained by comparison to literature values from* [146]

| **Specimen size [mm]** | **Density [g $cm^{-3}$]** | **Relative density [%]** |
|---|---|---|
| **6x6x6** | 3.049 ± 0.006 | 99.47 ± 0.20 |
| **4x8x8** | 3.005 ± 0.008 | 98.05 ± 0.25 |
| **3x5x5** | 3.050 ± 0.006 | 99.50 ± 0.18 |

### 4.2.2 Bulk Compressive Strength

Compressive strengths were measured for monolithic samples of different sizes, see Figure 20. The highly size dependent nature of mechanical properties with a linear relationship between compressive strength and specimen diameter, was not expected.

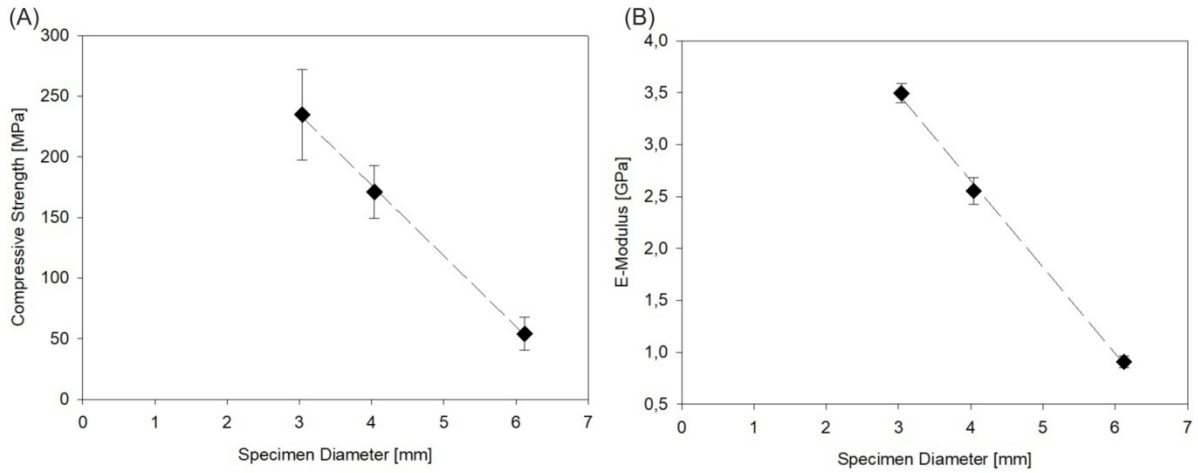


*Figure 20: (A): Bulk compressive strengths with linear regression $r^2$ = 0.999 and (B): E-modulus with linear regression $r^2$ = 0.998 of 0% porous samples of different sizes (6x6x6 mm, 4x4x8 mm, 3x3x6 mm) with st. dev., n = 8*

Theoretically, the size of the test specimen should not influence the attained values [147]. However, larger samples had increasingly arched surfaces, where an outward bulge in the size range of a few hundred µm was observed for the top surface parallel to the built layers as an artifact of the manufacturing method; see Appendix 2 for a light microscopy image thereof. This could on the one hand lead to incorrect positioning of the samples in the testing machine, causing unstable measuring parameters. On the other hand, when loads are applied, they could have been inhomogeneously distributed throughout the specimen and might have affected only the central area of the sample.

Thus, an overestimation of the affected cross-section of the larger parts could lead to lower apparent values. Another factor that needs to be considered is that machine rigidity was not taken into account during the measurements. This could lead to non-comparable results of apparent stiffness.

Nevertheless, measured compressive strengths of a maximum of 235 ± 37 MPa and apparent E-moduli of 3.49 ± 0.09 are within the expected range for TCP ceramics [64].

### 4.2.3 X-ray Photoelectron Spectroscopy

The following XPS results are all taken from measurements after argon-ion etching to remove adventitious carbon, which is present on all sample surfaces due to environmental factors [148]. XPS spectra before argon-ion etching are attached in Appendix 3.

From the C 1s regions displayed in Figure 21, it is evident that all traces of organic substances are removed during thermal processing of the specimens, as no evidence of carbon remains in the samples. This is beneficial, as it eliminates all concerns of potential cytotoxicity due to components of the organic binder present in the slurry.

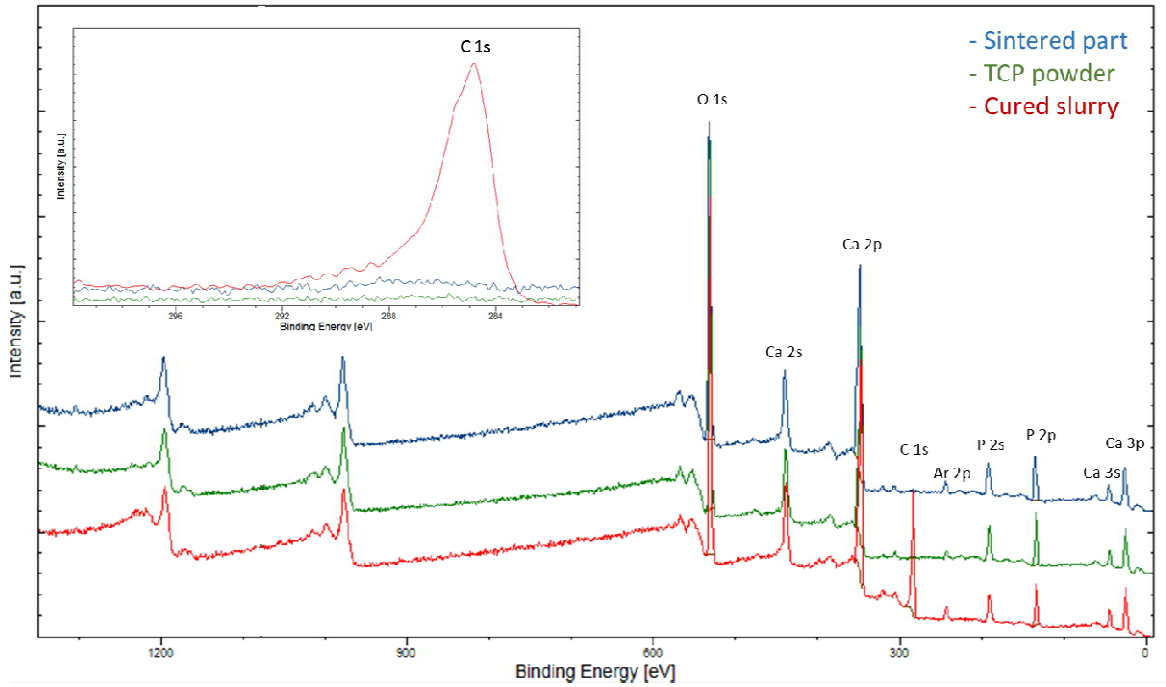


*Figure 21: XPS spectra of cured slurry (dried at 120 °C for 72 h), TCP powder prior to processing, and sintered part; after 2 min of argon-ion beam etching; with magnified C 1s region*

Peak positions and atomic ratios, as listed in Table 9, are in accordance with values known in literature. Although the ideal Ca/P ratio in TCP is 1.5, ratios between 1.4 and 1.5 are to be expected [149]. This could be due to calcium vacancies or substitutions with cation impurities such as magnesium [150]. Traces of magnesium could be indicated by the Mg 1s and Mg KLL peaks at 1303 eV and 306 eV respectively (the value for binding energy of the Auger peak is of course meaningless). Although these peaks are too small to be accurately quantified, they cannot be associated to any other elements, and from the carbon-free spectra it is evident that they are not merely satellite artifacts.

*Table 9: Peak positions and atomic ratios of elements in XPS spectra of cured slurry (dried at 120 °C for 72 h), TCP powder prior to processing, and sintered part; after 2 min of argon-ion beam etching*

| Sample | C 1s | | P 2p | | Ca 2p | | O 1s | | Ca/P ratio |
|---|---|---|---|---|---|---|---|---|---|
| | [eV] | [%at] | [eV] | [%at] | [eV] | [%at] | [eV] | [%at] | |
| **Cured slurry** | 284.8 | 35.06 | 133.0 | 11.03 | 346.6 | 18.44 | 530.7 | 35.48 | 1.67 |
| **TCP powder** | - | - | 133.1 | 19.01 | 346.8 | 27.06 | 530.7 | 53.92 | 1.42 |
| **Sintered part** | - | - | 132.9 | 18.60 | 346.8 | 27.03 | 530.5 | 54.37 | 1.45 |

### 4.2.4 Powder X-ray Diffraction

XRD spectra of TCP powder prior to sintering give mainly the β-TCP phase with 2.90 ± 0.26 vol.% HA, putatively stemming from the powder synthesis. In created parts, which were thermally treated up to 1200 °C, solely β-TCP remains, as depicted in Figure 22 (see Appendix 4 for complete spectra).This can be explained by a phase transition of HA to TCP at the high sintering temperatures [128]. No significant change in peak full width at half maximum after sintering indicates that there was no change in crystallite size and no formation of an amorphous phase could be identified.

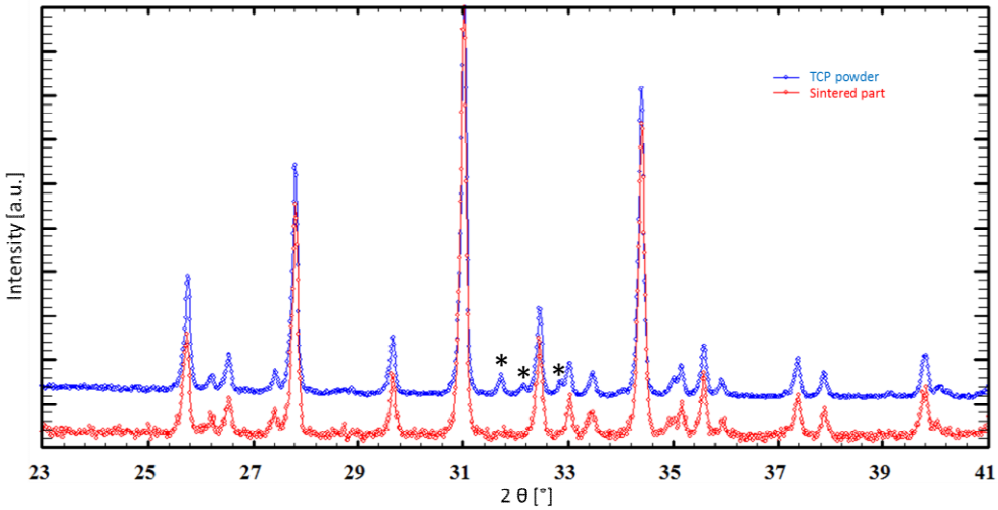


*Figure 22: Section of powder XRD measurement of TCP powder prior to processing, and sintered part. *represent HA reflections; all other peaks correspond to TCP reflections.*

### 4.2.5 Scanning Electron Microscopy

SEM images in Figure 23 A and B show manufactured parts perpendicular and parallel to the z-axis respectively. One can see the individual layers in off - 90° surfaces which create a saw tooth-type surface roughness. As DLP is pixel based, edges that are not completely perpendicular to the individual layers can only be generated by changing the illumination cross-section of each layer by pixel-sized increments. In the case of Figure 23 B, every 2-3 layers, one pixel more is illuminated to achieve the slanted surface. The steps of 20 ± 2 µm fit with the 25 µm layer height of the DLP after considering the shrinkage in z direction during thermal processing.

Grain sizes were measured at 3.83 ± 0.48 µm and few intergranular pores are present in the microstructure, compare Figure 23 C and D, which is in accordance with high densities measured in section 4.2.1.

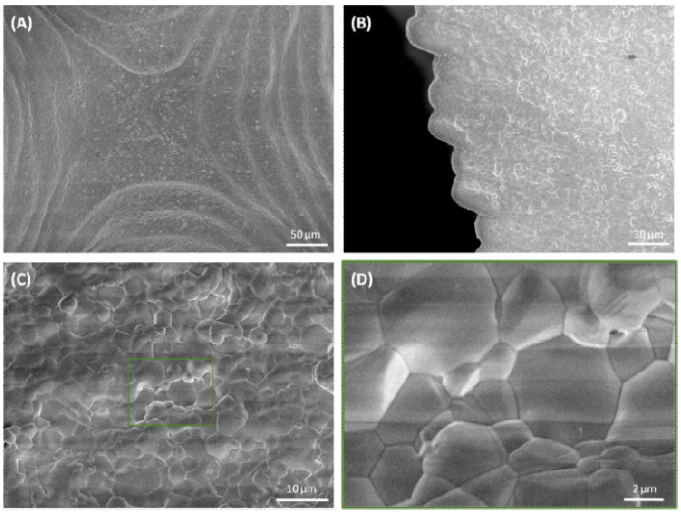


*Figure 23: SEM images of manufactured parts. (A): H50 imaged perpendicular to z-axis (layer top-view). (B): s50 imaged parallel to z-axis (layer side-view). (C) and (D): Microstructure of F0 specimen.*

## 4.3 Scaffold Screening

In the first screening of possible architectures, four different structures with three different porosities were created and analyzed in regards to geometrical accuracy with µ-CT. Mechanical properties were investigated in compression testing and biological activity was studied in SBF. From these results, two architectures were selected for optimization

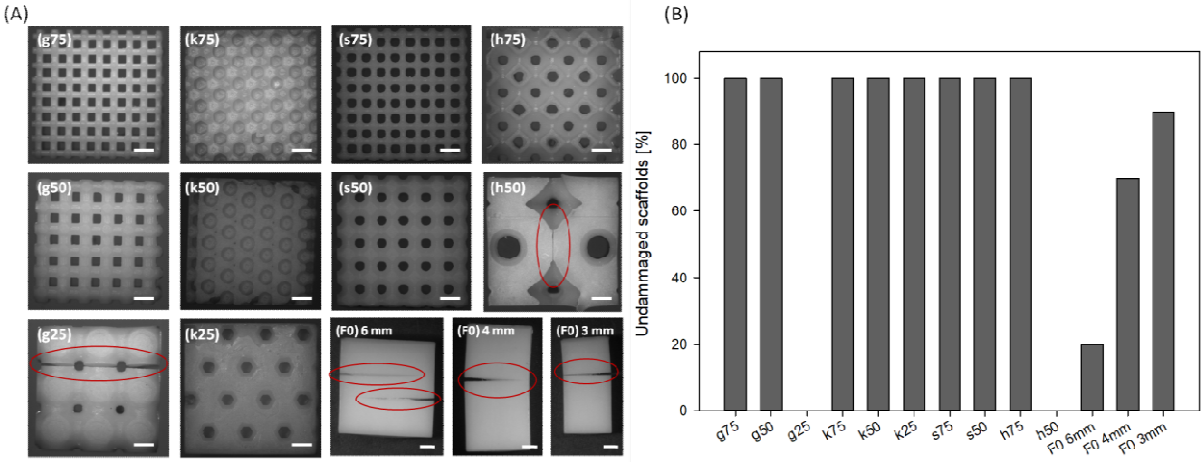


*Figure 24: (A): Reflected light microscopy images of cubes with different pore geometries and (B): percentage of undamaged manufactured scaffolds n = 24 (B). Specimen designation with letters referring to structure type (*F *is full,* g *is cylinder grid,* s *is Schwarz primitive,* h *is hollow Schwarz, and* k *is Kagome) and numbers corresponding to desired porosities, compare Table 2 for precise nomenclature. Defects marked in red. Scale bars are 1 mm.*

As is apparent from Figure 24, the h50 structure was not feasible as all these cubes fractured in the same location after thermal processing. The vertical crack initiated at sharp edges may occur due to the geometrical factor of stress concentration [151].

Structures g25 and F0 show fractures which are parallel to the individual layers. These delamination phenomena occur when interlaminar adhesion of the layers is not sufficient to withstand stresses formed during curing or thermal processing [145].

It is noteworthy that cracks in the g25 structure occur at pores, where change in wall thickness is great, potentially causing stress differences during shrinkage associated with the polymerization

reaction. For the F0 structure, there is a remarkable size dependency of crack formation after thermal processing with larger diameter parts being damaged more often.

This can be ascribed to the size dependency of the highly sensitive debinding step, where the cured polymer network is decomposed and volatilized. As diffusion paths increase in larger specimens, mass transport from the center becomes diffusion limited. Consequences are accumulation of degradation products or solvents, increase in vapor pressure, and finally cracking of the manufactured part [152].

It is thus inferable that these delamination cracks occur when wall thickness exceeds the maximum feasible dimensions *i.e*. approximately 3 mm.

### 4.3.1 Geometrical Accuracy

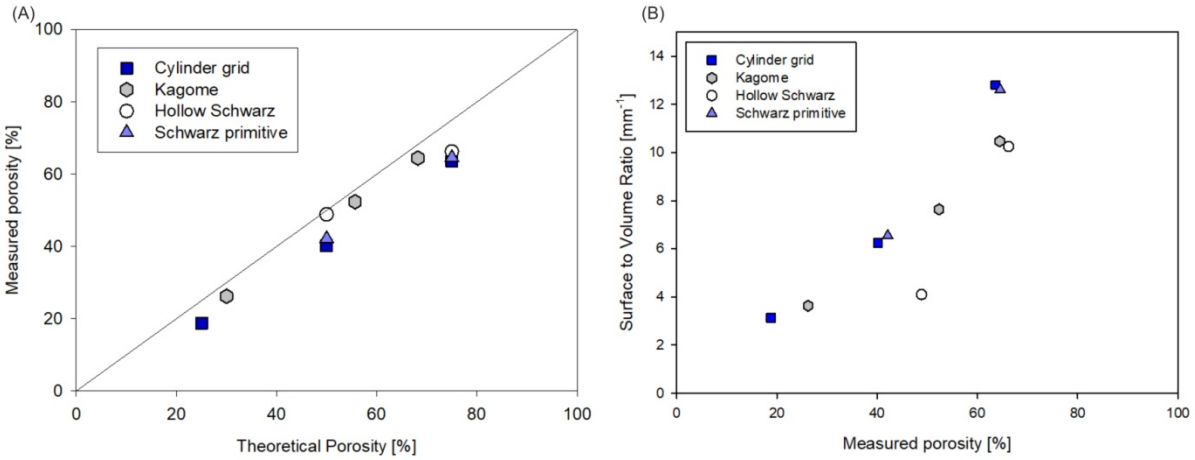


*Figure 25: (A): Measured porosity from µ-CT plotted against porosity according to specifications and (B): surface to volume ratio of the structures.*

All of the sample porosities according to µ-CT data are lower than specifications indicate, as shown in Figure 25 A. The Kagome structure is the most accurate with an average deviation of only -3.6 ± 0.2 % while the cylinder grid architecture differs by -8.7 ± 2.1 %. This could be due to the fact that the pore sizes of the Kagome structure are larger than for the other geometries.

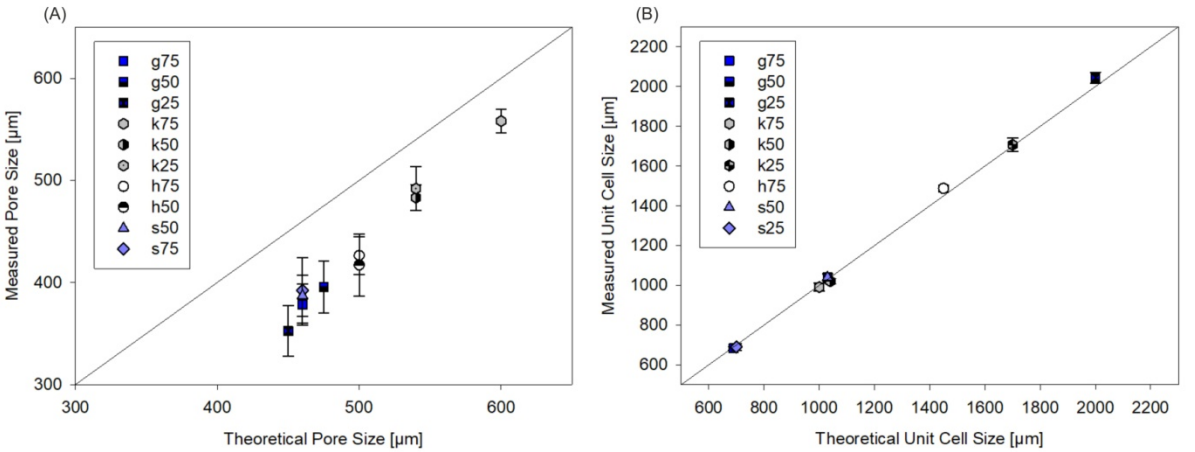


*Figure 26: (A): Average measured pore sizes and (B): unit cell sizes plotted against specifications; n = 16; with st. dev.*

Corresponding to lower porosities, pore sizes presented in Figure 26 A are also reduced when compared to pores of the CAD, with higher deviations for smaller pores than for larger ones. This is not an effect of scaling factors, as unit cell sizes are in accord with designed dimensions (Figure 26 B)

and must thus be an effect of excessive curing of the slurry during illumination. A visual comparison of STL files and µ-CT data is given in Figure 27, where over-polymerization is displayed in black.

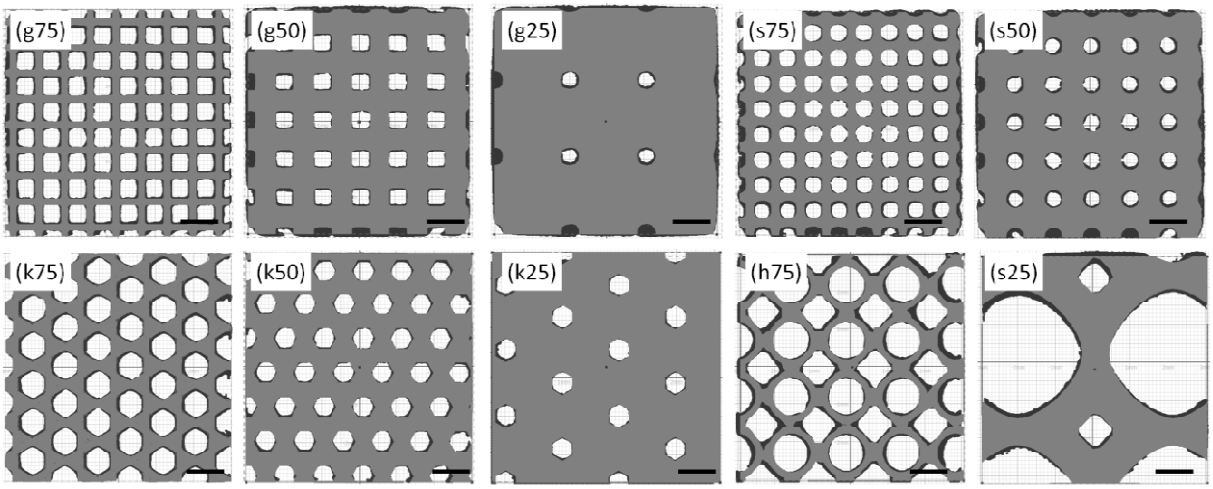


*Figure 27: Overlay of a slice of the scaffolds' STL files in grey with actual structures obtained from µ-CT data in black. Scale bars are 1 mm.*

The aforementioned pore size reduction was studied in detail; see Appendix 5 for measurements of all geometries. As evident from
Figure 28, this over-polymerization appears to be more extensive in scaffold centers than on surfaces and pores show more deviation from specifications in the xy planes than in xz and yz planes, though the latter trend is not statistically significant.

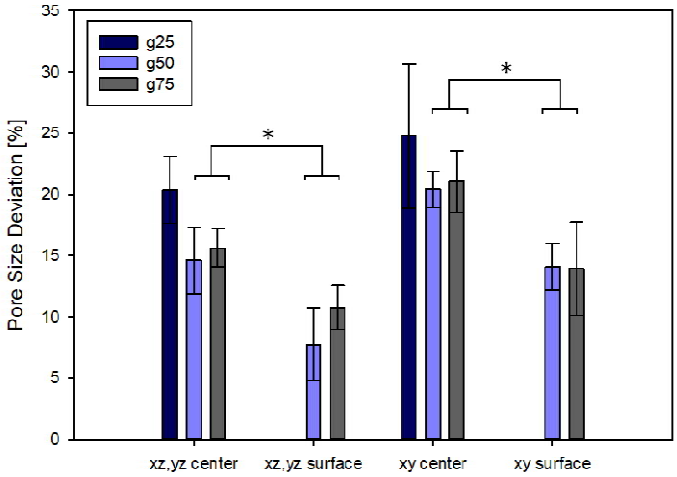


*Figure 28: Pore size reductions of the cylinder grid architecture for different locations in the scaffolds. Plotted with st. dev., n = 4; * for P < 0.05, n.s. for no statistically significant difference.*

A source of over-polymerization in the xy-plane *i.e.* parallel to the manufacturing layers, has been suggested to be light scattering at optical interfaces as well as in the slurry itself. Especially at the center of structures, scattered light from all sides can exceed the energy threshold necessary for polymerization even outside of designated illumination areas [54]. This leads to curing of a larger area and thereby a reduction of pore sizes.

The over-polymerization in planes perpendicular to the z-axis stems from the cure depth of incident light [144]. Each layer needs to be cured further than the 25 µm of layer height to achieve adhesion to the subsequent layer. However, in the case of a pore, there is no subsequent layer and the same excessive curing decreases the pore height.

In an attempt to overcome this issue and attain scaffolds with exact porosities and pore sizes, a factor can be calculated to account for over-polymerization, as is done for the optimized scaffolds.

### 4.3.2 Compressive Testing

Results of compressive testing are plotted in Figure 29. Apparent Stiffness is independent of structure type and only appears to be affected by porosity, with highly porous structures having lower values.

$$\frac{E^*}{E_s} = C_1 \left(\frac{\rho^*}{\rho_s}\right)^2 \tag{8}$$

$E^*$ … *Apparent E-modulus*
$E_s$ … *E-modulus of the cell-wall*
$\rho^*$ … *Density*
$\rho_s$ … *Density of the cell wall*
$C_1$ … *Constant of proportionality* ≤1

This trend is not, however, as pronounced as would be expected. The theoretical relationship to relative density is shown in Equation (8) [153]. With a proportionality constant ≤ 1, it is impossible to fit this equation to the present values. These discrepancies could be caused by machine rigidity, which was not quantified or taken into account during the measurement.

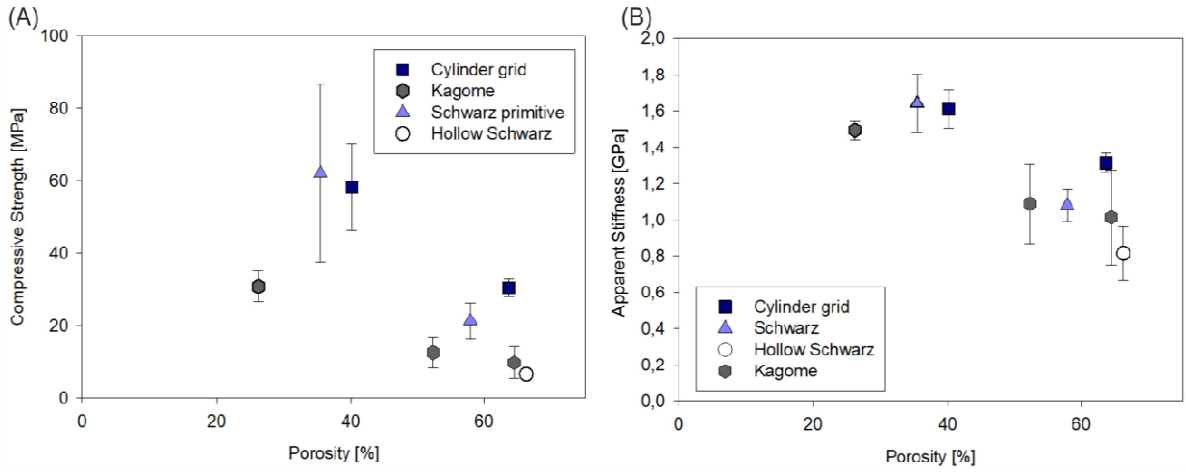


*Figure 29 (A): Compressive strength and (B): E-Modulus of fracture-less structures, with st. dev.; n=6*

When comparing compressive strengths of the different structure types, it was to be expected that the geometrically similar Schwarz primitive structure and the cylinder grid show similar behavior, which is the case. However, the reproducibility of the manufactured Schwarz primitive scaffold is wanting, putatively because the pixel-based illumination of the DLP creates unexpected sharp edges in its otherwise round pores. Due to its rectilinear nature, the cylinder grid structure is not as affected by pixilation and retains its mechanical properties as well as superior reproducibility.

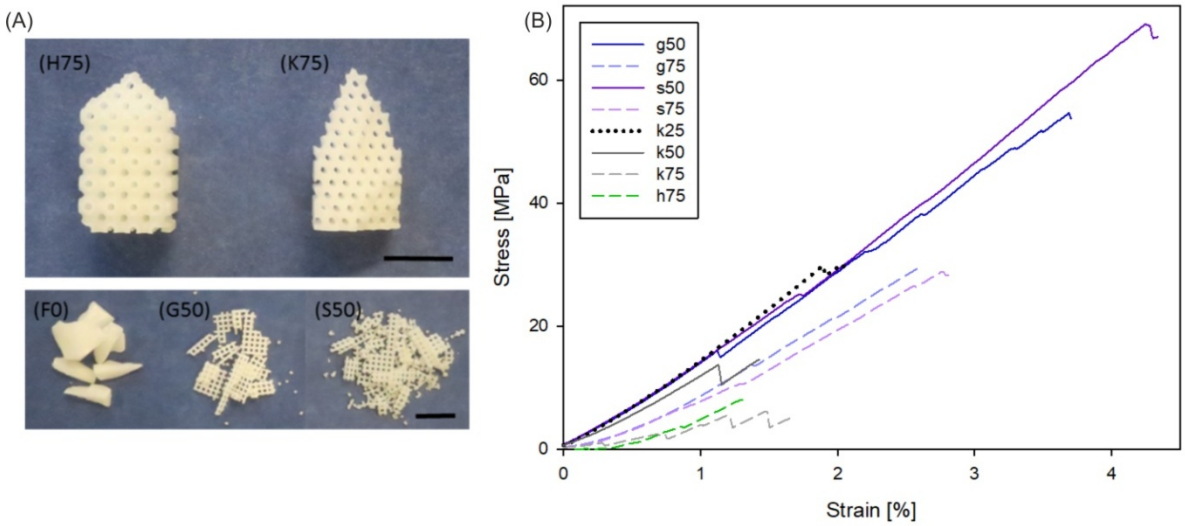


*Figure 30 (A): Pictures of scaffold fragments after compression testing, scale bars are 5 mm and (B) examples of single stress-strain diagrams of structures.*

The hollow Schwarz structure was inspired by a shellular type TPMS architecture, where thin shells of constant thickness create a structure which should exhibit homogeneous stress distribution and thereby withstand greater loads [126]. This was not the case, however, as premature failure along planes 45° to the architecture occurred, as shown in Figure 30 A. It can be argued that this is due to uneven wall thickness, as previous studies have had similar discrepancies between calculated properties and measured strengths [154]. As the CAD was not created parametrically but through a Boolean type subtraction from the Schwarz primitive architecture, the error could originate from the design of the scaffold.

Although literature has shown that the Kagome structure has superior mechanical properties than its grid counterpart [155], it also falls short of expectations. Fracture angles were 30° to the main axis along unit cell borders, attesting to inhomogeneous stress distribution. In Figure 30 B one can see that Kagome structures show pronounced discontinuities in their stress-strain diagrams. This can be explained by individual rows of unit cells failing at each spike and is in accordance with the phenomenon of compressive strength decreasing with the number of layers in Kagome architectures [156]. These steps are present in all structures but are much less pronounced for cylinder grid and Schwarz primitive geometries, explaining the latters' higher degree of destruction after compression.

Due to large variance, especially for stronger specimens, a larger sample number would be required to attain precise values.

### 4.3.3 Analysis in Simulated Body Fluid

After immersion of the scaffolds in SBF, HA deposition or TCP dissolution was investigated. When regarding change in sample mass in Figure 31 A, all structures appear to be inert with no significant gain or loss in mass. This is supported by XPS and XRD measurements after exposure to SBF. No HA or any other phases besides β-TCP were found in powder XRD data, as presented in Appendix 4. XPS indicates a Ca/P ratio of 1.45 with potential traces of Na and Mg, as visible from their respective Auger peaks, see spectrum in Appendix 3.2, which does not differ from the spectrum prior to exposure to SBF.

µ-CT data in Figure 31 B, however, do indicate that the scaffolds were affected by SBF. The very similar cylinder grid and Schwarz primitive architectures also behave similarly by partly dissolving in SBF after 21 days. The hollow Schwarz and especially the Kagome structures indicate material deposition. The most extreme cases (g50 and k50) were also measured for days 7 and 14, pointing to

initial increase in volume with subsequent reduction. This is putatively due to different deposition and dissolution kinetics, with dissolution occurring predominantly at later time-points during the experiment. As only single scaffolds were analyzed in µ-CT, reproducibility of the data is unfortunately not certain.

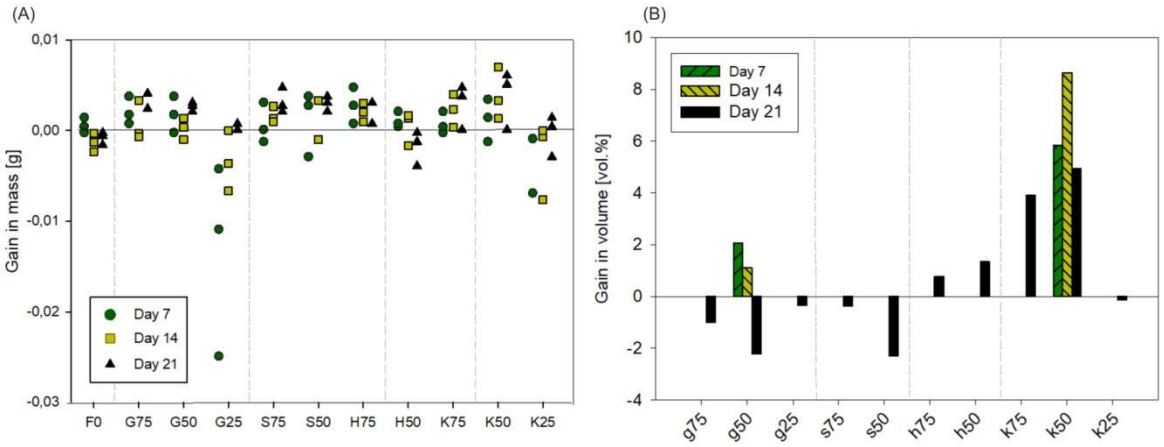


*Figure 31 (A): Change in mass of samples after immersion in SBF for 7, 14, and 21 days and (B): Change in volume, measured from µ-CT data.*

Visual inspection of the µ-CT images shows no blockage of pores and all geometries appear to retain full interconnected porosity, as depicted in Figure 32.

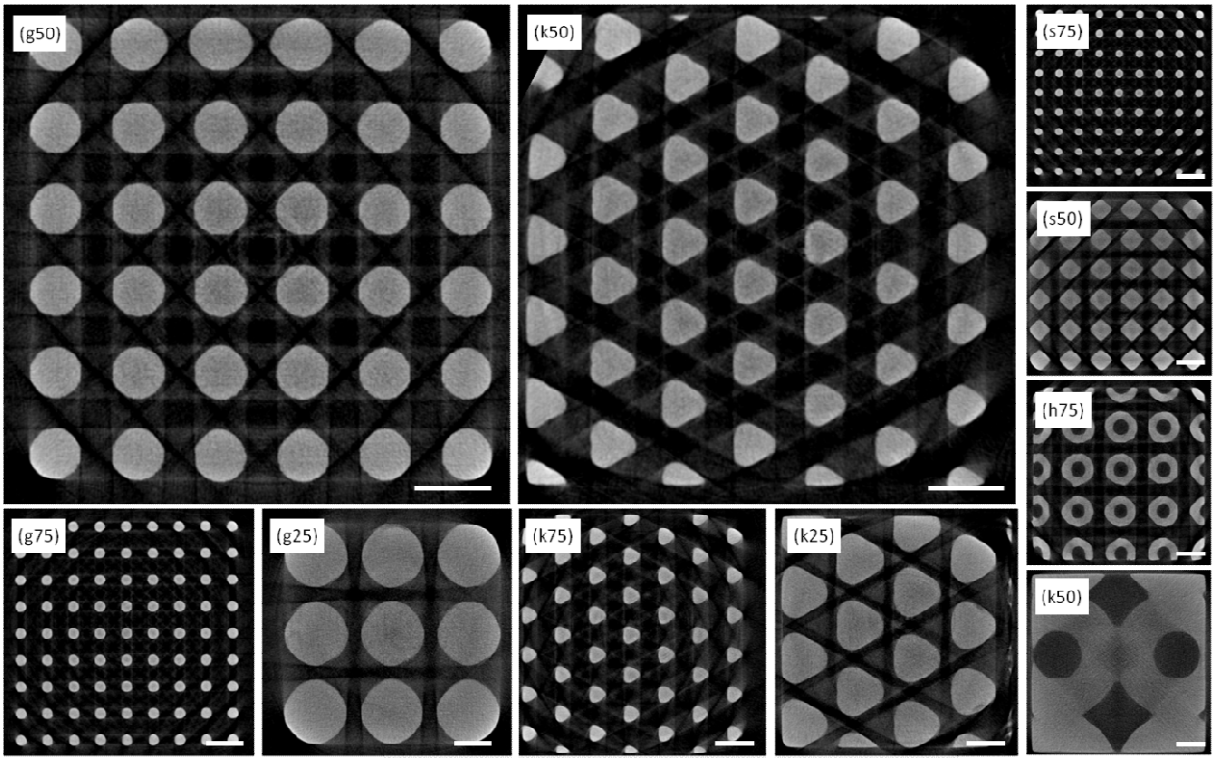


*Figure 32: µ-CT slices of 6x6x6 mm cubes exposed to SBF for 21 days. Scale bars are 1 mm.*

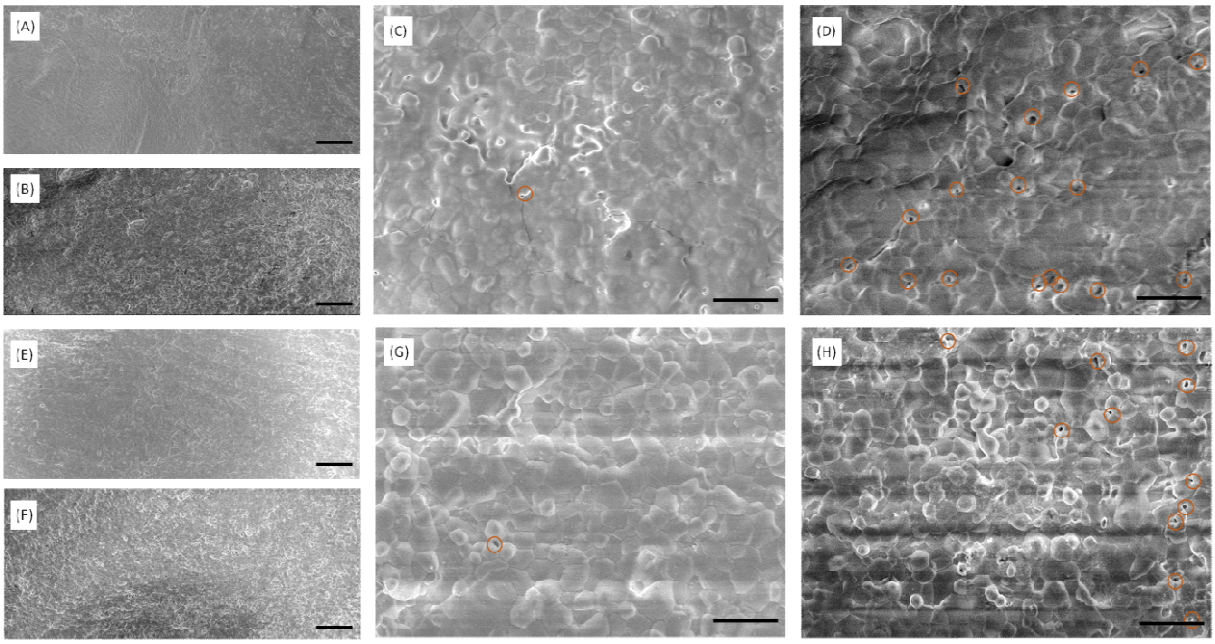


*Figure 33: SEM images of: (A, C): g50 before SBF; (B, D): g50 after 21 days immersion in SBF; (E, G): k50 before SBF; (F, H): k50 after 21 days in SBF. Intergranular porosity is marked in red. Scale bars are 40 µm for (A, B, E, F) and 10 µm for (C, D, G, H)*

SEM images of the samples prior to and after immersion in SBF are shown in Figure 33. Both analyzed structures have increased intergranular porosity post-SBF. The Kagome structure appears to have additional changes in surface morphology which could possibly indicate material deposition, although it is hard to say due to the charging effects in the latter sample.

## 4.4 Optimized Scaffolds

From the previous results, two scaffold architectures were selected for further investigation; the cylinder grid structure, due to its advantageous mechanical properties while still showing higher reproducibility than the Schwarz primitive geometry, and the Kagome structure due to its performance in SBF and unique pore shape. Porosities were selected at 75 and 50 % and pore sizes were set to 400 µm. µ-CT images of the scaffolds are depicted in Figure 34.

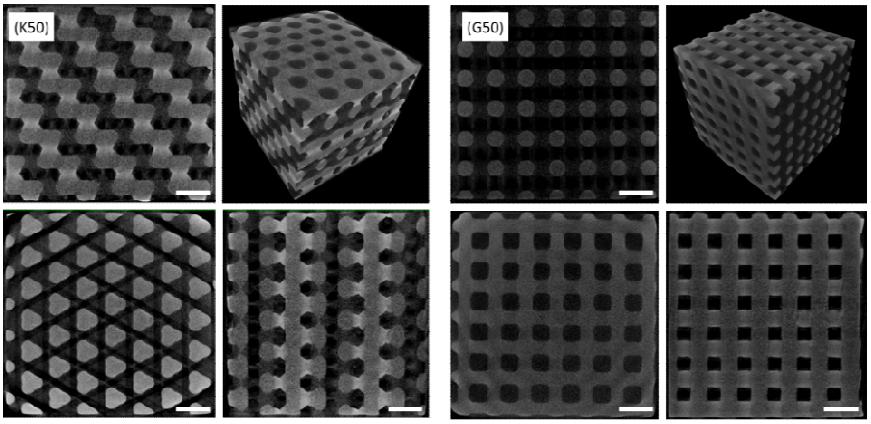


*Figure 34: µ-CT images of the K50 (left) and G50 (right) scaffolds at 50 % porosity*

### 4.4.1 Geometrical Accuracy

The linear scaling factor employed in order to attain more precise results, appears to be satisfactory for the pore sizes of both structures, compare Figure 35 A. Measured pore sizes are within ± 23 µm of the desired dimensions, which is less than the 40 µm pixel size of the DMD. Without this scaling factor, especially the cylinder grid structure had significantly larger deviations. Unit cell sizes remain acceptable at average deviations of less than ± 11 µm, compare Figure 35 B.

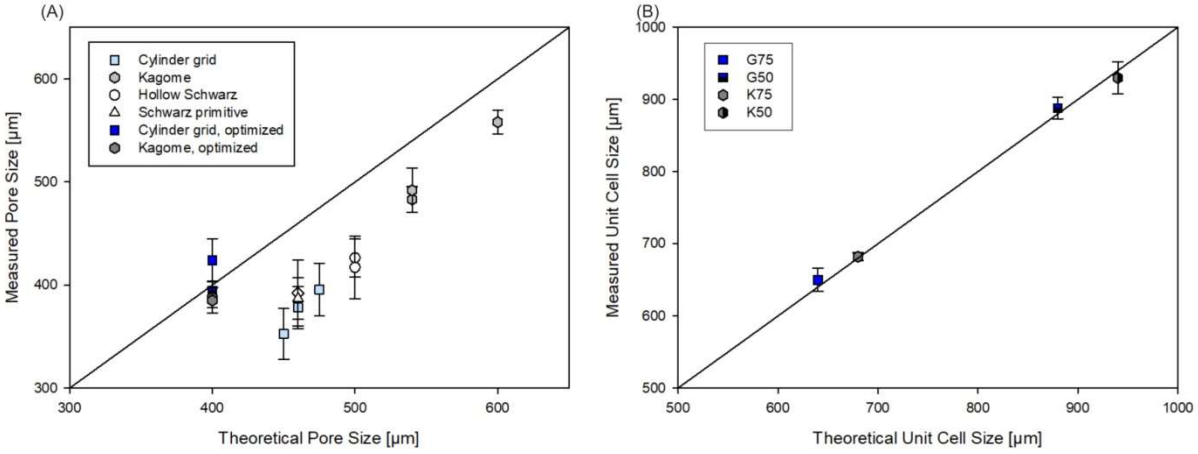


*Figure 35: (A): Average measured pore sizes compared to non-optimized scaffolds and (B): unit cell sizes plotted against specifications; n = 16; with st. dev.*

As visible from Figure 36 A the factor for porosity is adequate only for the cylinder grid geometry, where deviations are reduced to less than 2 % as opposed to the previous 11 %. For the Kagome structure, over-polymerization remains at 9 %. This might be due to the fact that the Kagome geometry does not follow linear laws in its volume increase. Additionally, the pore sizes of previous Kagome structures from which scaling factors were calculated, were significantly larger, which might not be transferrable to the present geometries.

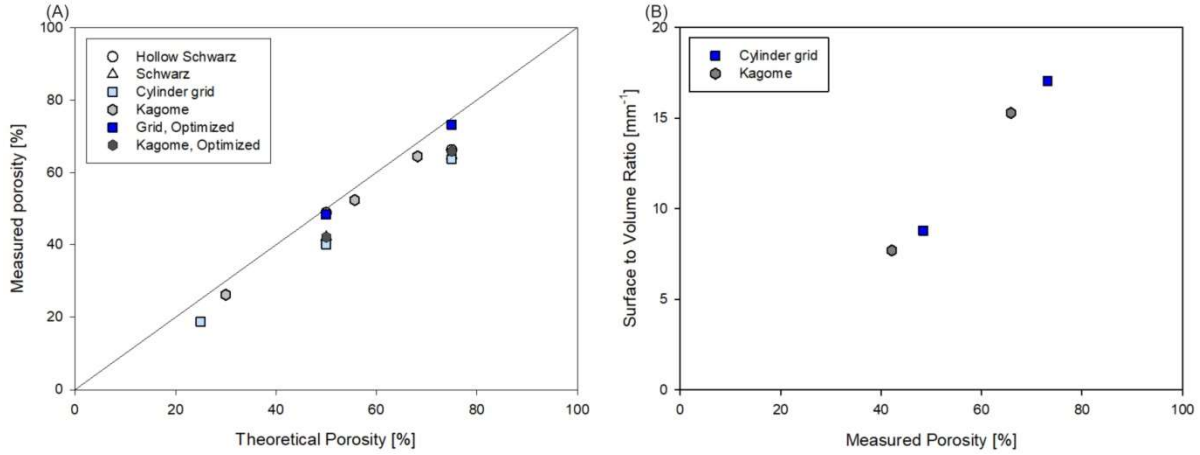


*Figure 36 (A): Measured porosity from µ-CT plotted against porosity according to specifications and compared to non-optimized scaffolds. (B): Surface to volume ratio of the optimized scaffolds.*

### 4.4.2 Compressive Testing

Figure 37 and Table 10 show results of compressive testing. One can see that, as expected from previous results, the cylinder grid structures show superior strength at not significantly different apparent stiffness. Superior reproducibility of the Kagome structure, reflected by Weibull modulus as well as standard deviation of the apparent stiffness, is putatively due to the distinct failure mechanism, as previously discussed in section 4.3.2.

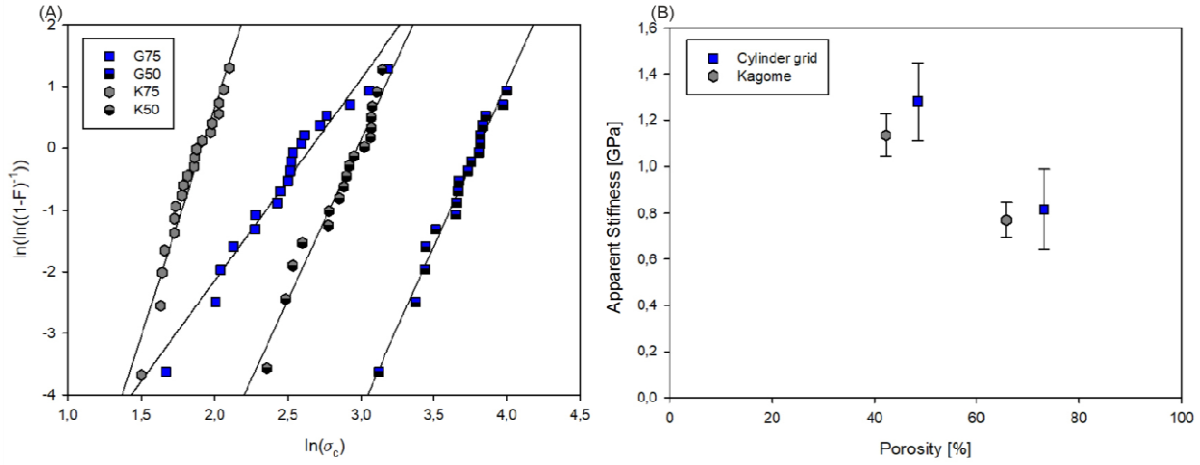


*Figure 37: (A): Weibull plot of fabricated scaffolds and (B): average E-Modulus with st.dev., n ≥ 18.*

Weibull moduli of ≥ 10 would be desired for ceramics. These slightly lower values are, however, in accordance with values of 3 - 10 previously found in literature for similar TCP structures [91]. As only at least 18 replicates were measured, which is at the lower limit for Weibull evaluations, further analysis might be necessary.

*Table 10: Weibull modulus, compressive strength and E-modulus of fabricated scaffolds with st.dev., n ≥ 18*

| Sample | Weibull modulus | Compresive strength [MPa] | E-Modulus [GPa] |
|---|---|---|---|
| **G50B** | 5.28 | 44.7 | 1.28 ± 0.17 |
| **G75B** | 3.27 | 14.2 | 0.82 ± 0.17 |
| **K50B** | 5.18 | 19.5 | 1.14 ± 0.09 |
| **K75B** | 7.40 | 6.75 | 0.77 ± 0.08 |

## 4.5 3D Cell Culture

Murine pre-osteoblast cells, MC3T3-E1, were cultured on the scaffolds in osteogenic medium as well as on 2D wells with osteogenic (OM) or basal (M) medium. Cell growth, differentiation, ECM formation, and mineralization were analyzed in a 21-day experiment.

### 4.5.1 Cell Growth

Figure 38 shows the amount of cells for the different conditions and 2D controls. Although the same amount of cells was seeded for all wells, the 3D scaffolds had significantly lower cell numbers starting from day 1, with the non-porous one having the lowest amount of cells. This is putatively due to low seeding efficiency of the scaffolds as the majority of the cells wash through to the floor of the well [157]. Nevertheless, the porous scaffold exhibited higher amount of initial cell attachment than the non-porous TCP block. The 2D cultures did not have seeding issues, leading to the higher cell numbers detected throughout the entire experiment, further reducing their comparability to the 3D conditions.

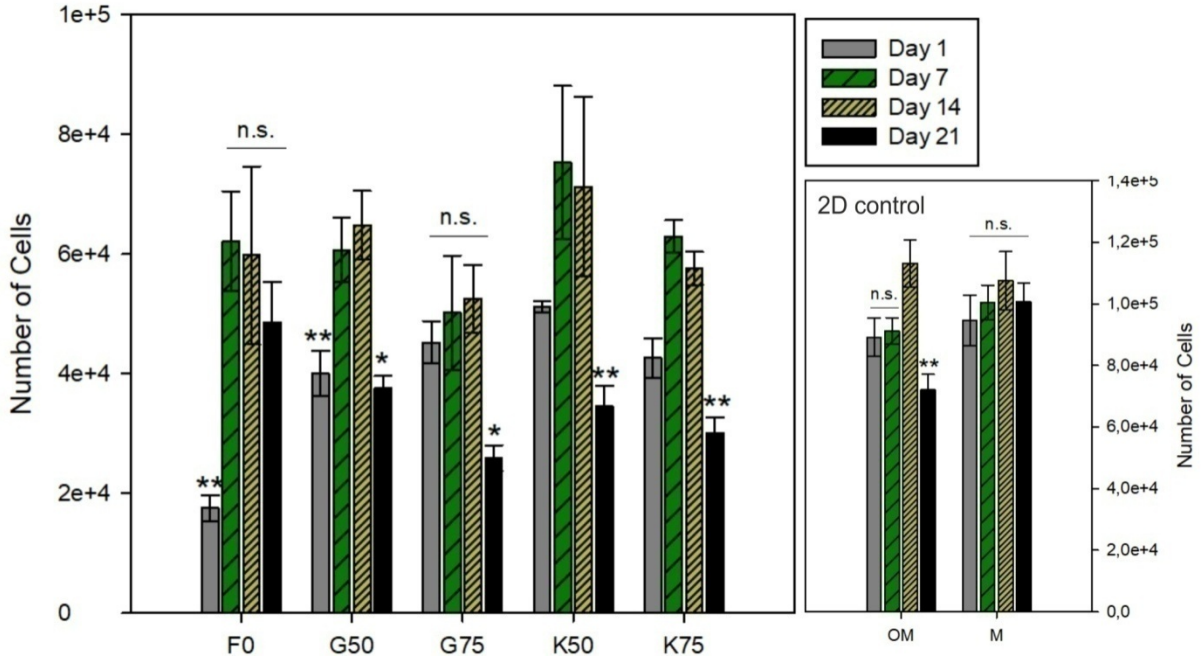


*Figure 38: Number of cells from DNA quantification and comparison to a regression curve for the different scaffolds (left) and 2D cultures (right) in osteogenic medium (OM) and basal medium (M) at 4 time points. n.s. for not statistically significant, * for P ≤ 0.005, and ** for P < 0.001.*

Evidently as a consequence of the stress that cells had to endure during the seeding process, metabolic activity on the first day is reduced when compared to the other time points, as seen in Figure 39. Cells on the non-porous scaffold took longer to regenerate, as day 14 still shows low activity. All further time points, however, show no statistically significant difference in metabolic activity within one scaffold type.

After an initial growth phase of 7 days, shown by the drastic increase in DNA (Figure 38), the amount of cells on the scaffolds stays constant until day 14. Although not statistically significant, it appears that Kagome scaffolds have more cells at these time-points than the grid architectures. By day 21, however, all porous scaffolds as well as the cells seeded in osteogenic medium, exhibit a significant decrease in cell numbers. As the 2D control also exhibits this phenomenon, it cannot be an effect of lacking viability of the scaffolds but indicates that the cells had other issues with long-term stability.

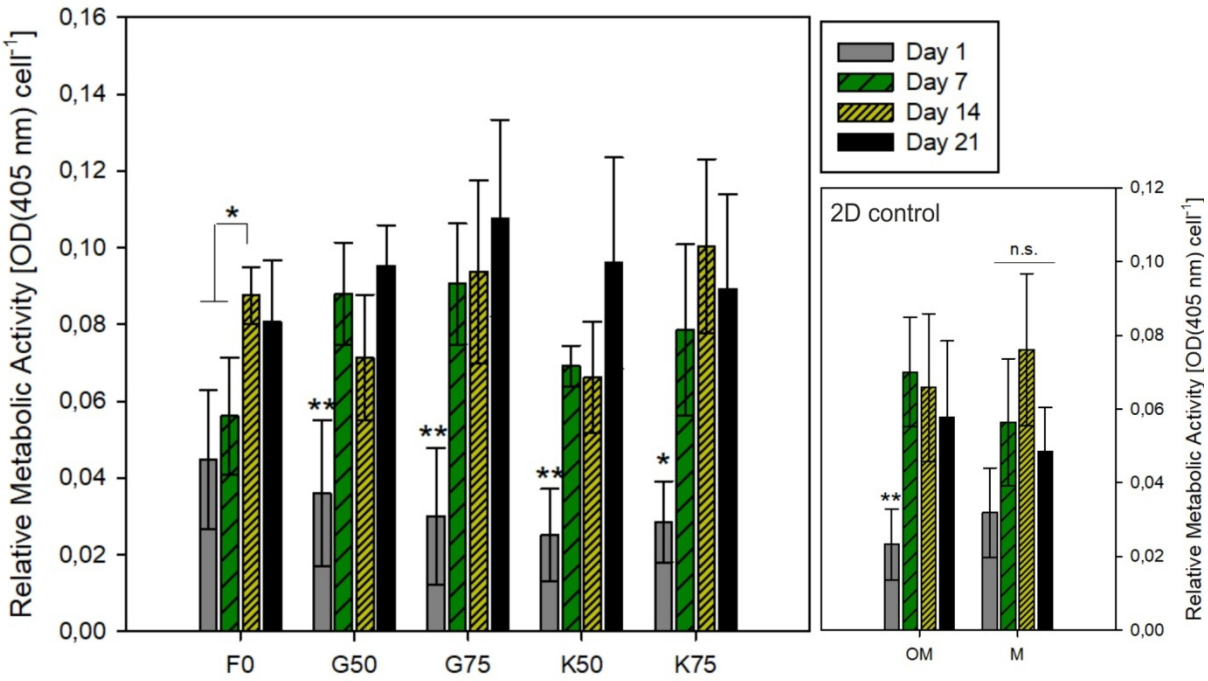


*Figure 39: Relative metabolic activities scaffolds and 2D cultures normalized to cell number. n.s. for not statistically significant, * for P ≤ 0.005, and ** f.*

The fluorescence images in Figure 40 after staining of the nucleus and cytoskeleton provide supporting information. While cells are not yet confluent on day 1, all of the conditions except for the non-porous F0 scaffold are completely confluent by day 7, with the cells forming a dense multilayer on all of the scaffolds. By day 14, however, cell morphology starts to deteriorate. Actin fibers are no longer structured and nuclei start to detach, as seen by the isolated specks of DNA. By day 21, all of the scaffolds except for F0 and K75 have further deteriorated, as indicated by a further decrease of F-actin structures and by the increasingly dot-shaped DNA clusters as opposed to healthy circular or oval shapes in earlier samples. Thus, these images indicate that cell death is induced by over-confluency early on in the experiment, which is a well-described phenomenon of MC3T3-E1 cells [158].

By visual comparison, the actual presence of DNA seems not to have decreased, which appears to contradict the DNA quantification assay. This might be extremely misleading, however, as it is impossible to estimate quantification especially on these complex 3D scaffolds. Additionally, some detached DNA fragments which were not washed away prior to staining, could have been eliminated in the more aggressive washing step preceding DNA quantification.

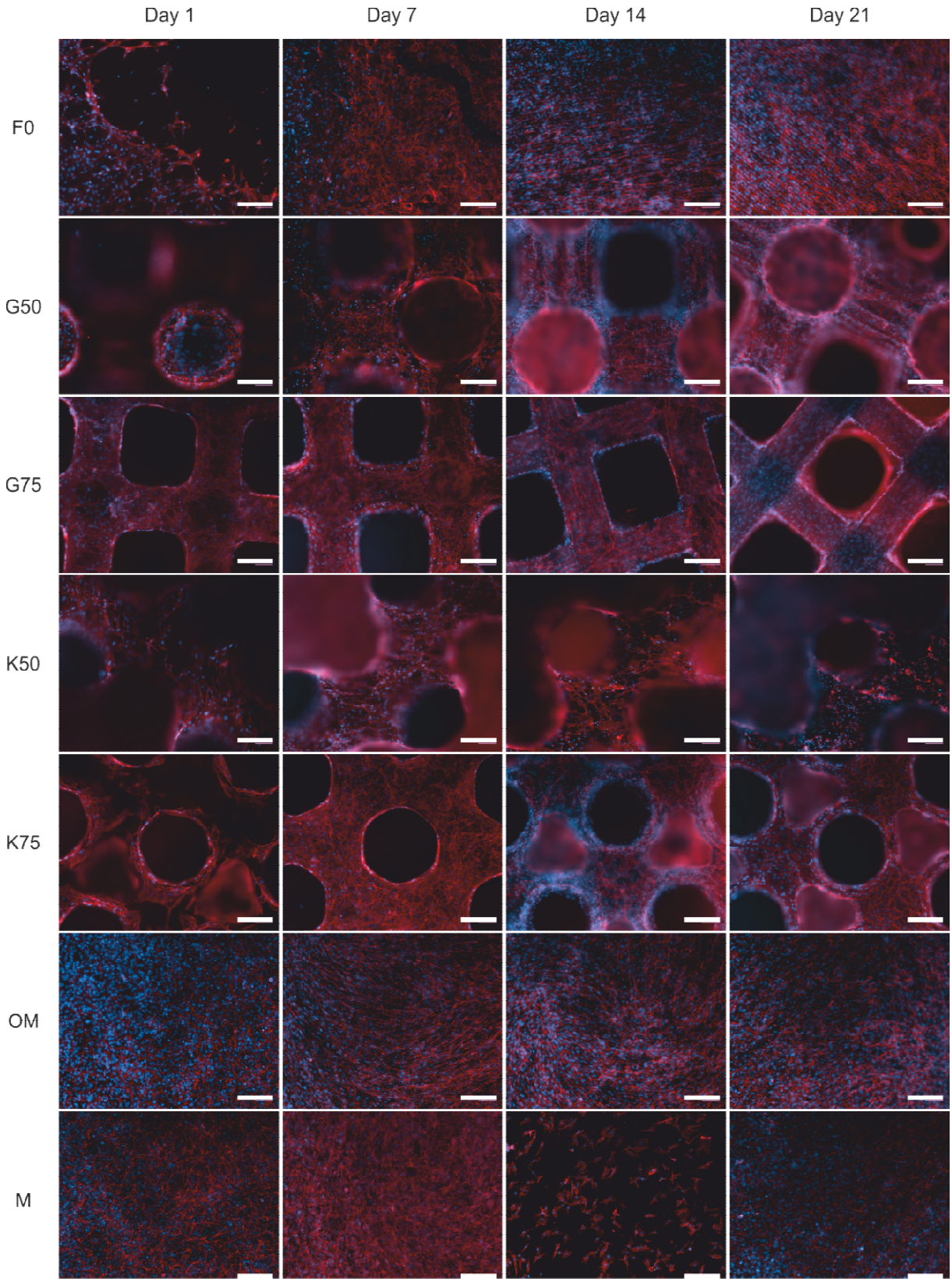


*Figure 40: Fluorescence microscopy images after staining of DNA with DAPI (imaged in blue) and of F-actin with phalloidin (imaged in red). Scale bars are 200 µm*

When regarding cell morphology, several phenomena need to be addressed. Attached cells start to exhibit the typical cuboid osteoblast shape by day 21, as imaged in Figure 41 (bottom row) on the example of the K75 structure. On day 1, the not yet confluent pre-osteoblasts have attached to the

scaffold and bridge concavities with actin filaments. By day 7, confluency is reached and on day 21, the cells appear as fully differentiated osteoblasts.

Especially on the F0 structure (Figure 41 top row), one can see that cells orient themselves along the scaffold grooves originating from the individual scaffold layers. Nuclei as well as actin filaments follow the ridges which, at 20 µm, have similar dimensions as the individual cells. It has been previously described that micro grooves improve cell adhesion [159], which could be a positive side effect of the present additive manufacturing method.

The larger notches in the G50 structure (Figure 41 middle row), which stem from the pixilation necessary for rounded surfaces, also act as a guide for the cells. Here, however, it is primarily the actin filaments which are oriented whereas the nuclei retain a degree of disorganization. This might be due to the larger groove dimensions.

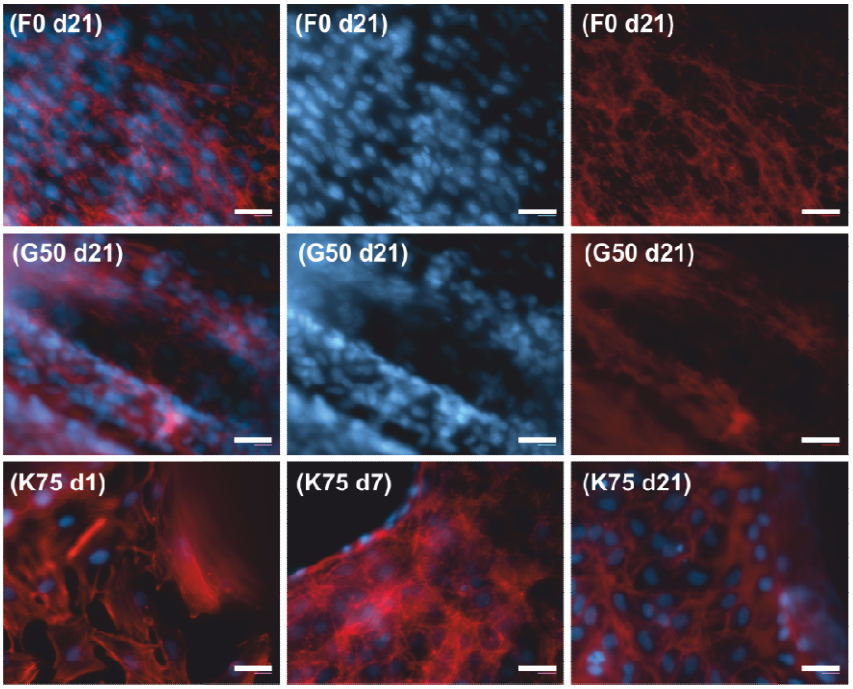


*Figure 41: Selection of fluorescence images at larger magnifications. Scale bars are 40 µm.*

In order to see further than just the scaffold surfaces, confocal fluorescence microscopy was implemented. Thus, the pores' interiors could be imaged, as shown in Figure 42. More Actin stress fibers can be seen for lower porosity scaffolds, presumably due to the fact that the lower surface area is covered more quickly by cells and therefore they expand further into the pores. It is notable that the hexagonal pores of the Kagome scaffolds exhibit a larger amount of growth than the cuboid pores of the grid structure.

This curvature driven tissue growth has been extensively investigated for osteoblasts on HA by Rumpler *et al.,* who propose that it is due to the cells aiming to reduce surface tension. They also state that the total tissue growth is not affected by their channel geometry, which is also the case for the present pores. According to DNA quantification, the slightly higher total number of cells on the Kagome scaffolds is not statistically significant.

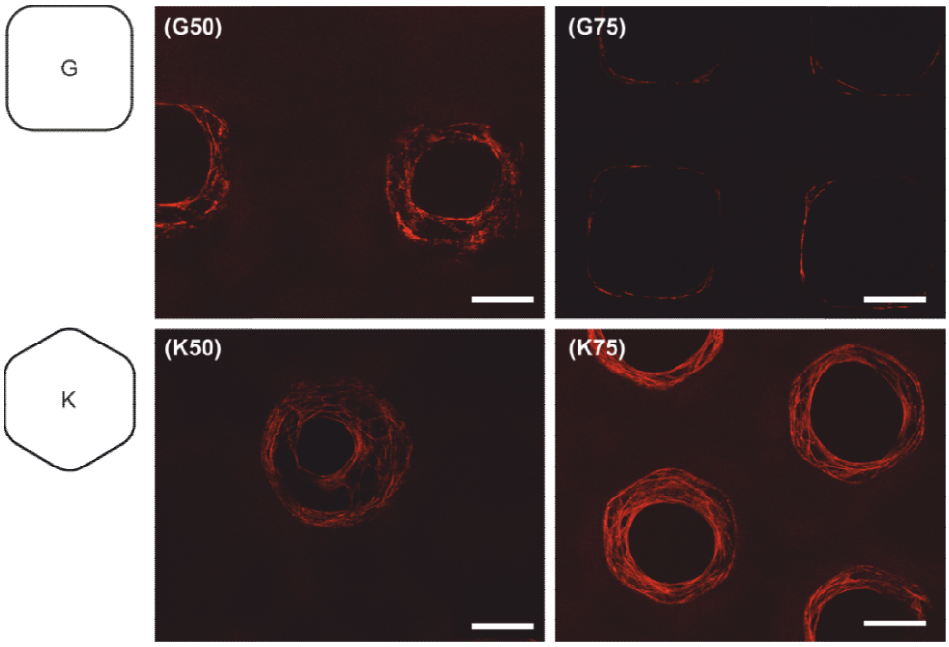


*Figure 42: Overlay of a z-stack of confocal scanning microscopy images of F-actin stained scaffolds at day 7. Depth is 120 µm with one image every 20 µm. Scale bars are 200 µm.*

### 4.5.2 Differentiation

As an early osteogenic marker, ALP activity is expected to rise as cells progress from the proliferation to the differentiation stage. An increase of 2 - 6 times the initial activity is expected after 3 weeks of differentiation [160]. Figure 43 shows that ALP activity of cells on the scaffolds is unexpectedly high starting from day 1 with no significant difference to day 7. Perhaps due to the high amount of cells seeded and due to possibly inhomogeneous application of the cell suspension to the scaffolds, isolated areas of confluency could have started to differentiate prematurely. After 2 weeks on the scaffolds, activity rises and stays elevated also until day 21. The notable exception is the G50 scaffold, where a statistically significant decrease in ALP activity can be observed on day 21.

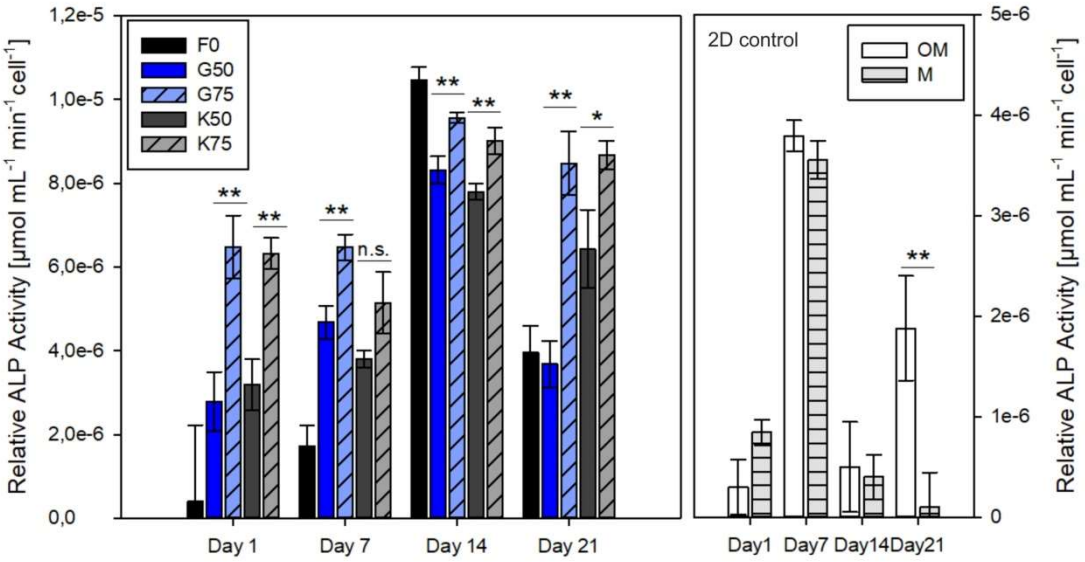


*Figure 43: ALP activity normalized to cell number; n = 6; with st.dev.; n.s. for not significant, * for P < 0.005 and ** for P < 0.001.*

The non-porous F0 structure exhibits lower ALP activity on days 1 and 7 with highest activity on day 14, which drops by day 21. The 2D wells similarly have a single maximum time-point but a week

earlier, in accordance with more effective cell seeding. Their maximum ALP activity is less than half as high as for cells on 3D scaffolds. Notably, there is no difference between cells cultured in osteogenic or basal medium.

With ALP being more active on the scaffolds for an extended period of time when compared to both non-porous and 2D references, one can safely propose that early osteogenic differentiation is enhanced on the porous TCP structures. A comparison of the individual scaffold types yields no significant difference between grid and Kagome structures. Scaffold porosity does, however, appear to strongly affect ALP activity. At all time-points the 75 % porous structures have higher activities than their 50 % counterparts.

### 4.5.3 ECM Formation

ECM formation of osteoblasts can be characterized by collagen type I deposition. As visible from Figure 44, collagen deposits can be observed starting from day 7 with a gradual increase until day 21. The utilized assay, however, quantifies total collagen content, not only type 1. This explains the initially high levels, as newly synthesized collagen which is not yet integrated into fibrils is also taken into account. Although this rationale limits the relevance of the present assay, it nevertheless aids in validation and quantification of ECM formation, as illustrated by the vast difference in collagen quantity when comparing cells cultured in osteogenic and basal medium. Additionally, the increase in collagen on day 21 for all investigated samples indicates osteoblast formation. It is to be noted that in this case comparison of absolute values of collagen content between 2D and 3D cultured cells is not advisable, as normalization to cell number cannot be implemented due to the additive nature of the collagen deposition.

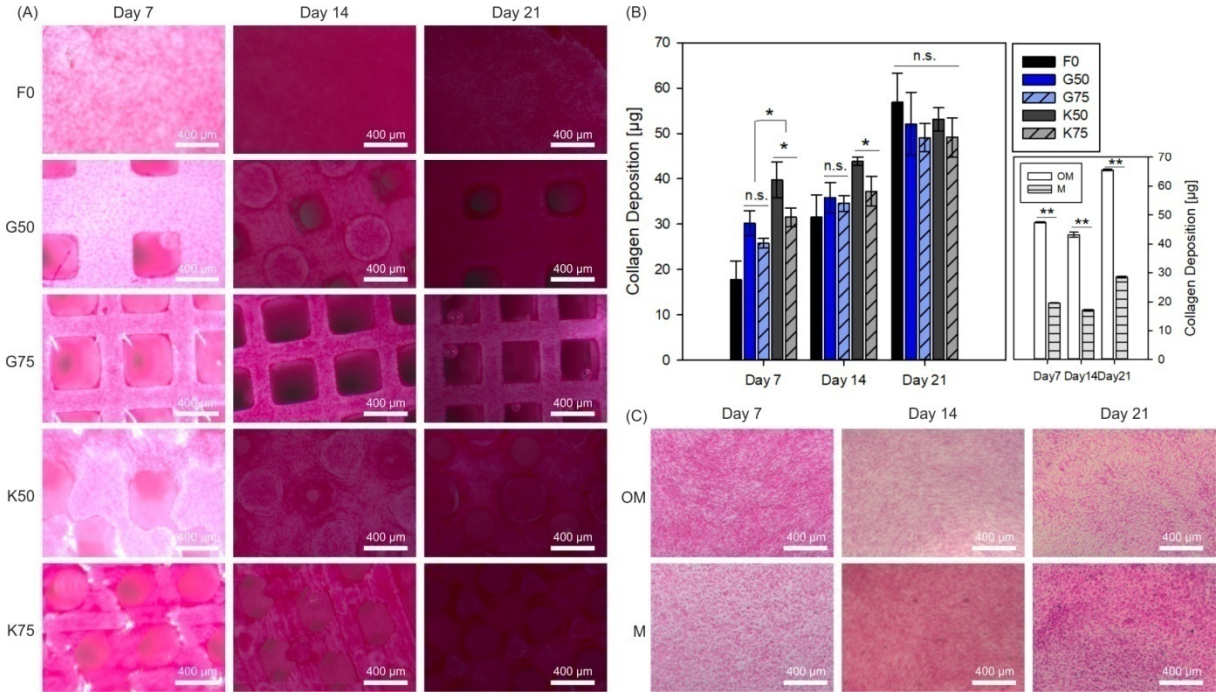


*Figure 44: (A): Reflected light microscopy images of stained collagen on 3D scaffolds. (B): Colorimetric quantification of collagen, n = 6 with st.dev.; n.s. for not statistically significant ,* for P ≤ 0.005, and ** for P < 0.001. (C): Stained collagen on 2D wells*

Though not always significant, the 50 % porosity scaffolds seem to have higher amounts of collagen deposition than those with porosities of 75 %. As this effect is miniscule and contradicts the trend of ALP activity, it raises the question whether it is an effect of the cellular activity or an artifact of collagen being washed away from the more permeable scaffolds during media changes or even during implementation of the assay. Additionally, by day 21, the individual scaffold types show no

difference in collagen deposition. Only up until the second week of the experiment did the Kagome structure exhibit higher collagen formation than the grid scaffold.

### 4.5.4 Mineralization

Calcium deposition is one important aspect of ECM mineralization. Thus, $Ca^{2+}$ was stained with ARS and quantified, compare Figure 45. The F0 structure has low calcium deposition, which gradually increases over time. This is the only sample which acts according to expectation. All of the porous scaffolds have constantly high levels of ARS staining with no significant difference between time-points or scaffold types. Conversely, the 2D conditions show no significant calcium deposition whatsoever.

One potential issue in ARS staining is that the TCP scaffolds also contain calcium. However, while ARS does adsorb onto solid calcium-rich phases, its affinity is not high enough to dissolve the compounds [161]. Furthermore, the validity of using the present assay is confirmed by the negative controls, see Appendix 6, which only show pale pink discoloration as opposed to the dark red precipitate formed on the viable scaffolds, and by extension show ARS concentrations not significantly different from 0.

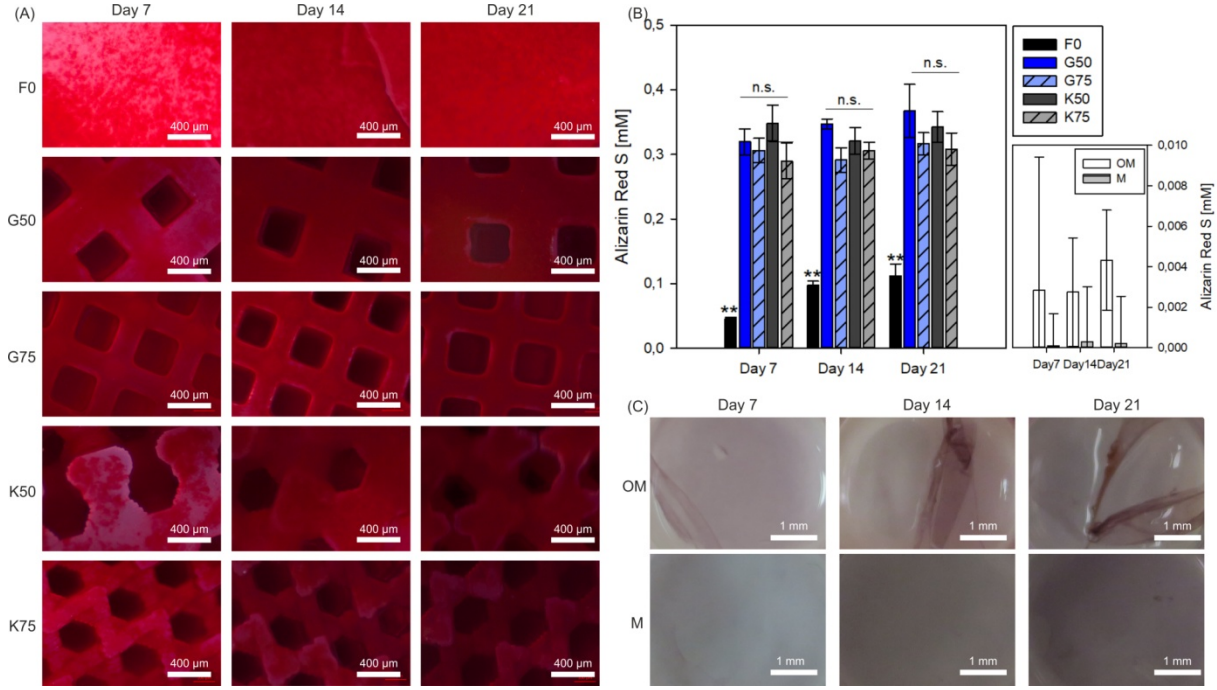


*Figure 45 (A): Reflected light microscopy images of ARS stained calcium on 3D scaffolds. (B): Colorimetric quantification of ARS, n = 6 with st.dev.; n.s. for not statistically significant,* for P ≤ 0.005, and ** for P < 0.001. (C): Stained calcium on 2D wells*

Another proposed reason behind the continuously high levels of calcium is that it was not the collagen fibrils that were mineralized by the cells but the scaffolds themselves. A saturation of the surface by day 7 could explain the lack of an upwards trend in calcium content in the subsequent weeks.

Although the clean negative controls also validate the washing process of the dye, it is possible that the presence of cells and of the proteins that they synthesized impede permeability of the scaffolds. Thus, unbound dye could be trapped in the scaffolds centers, explaining the high concentrations of the porous samples.

Taking into account all of these factors and uncertainties, the significance of this assay is limited, if not highly questionable in the present case.

# 5. Conclusion

Material characterization by XPS shows that no significant contaminants are present. A slight calcium deficiency in the sintered samples of an average of 1.2 at.% indicates vacancies. XRD measurements show that there are traces of an HA phase in the TCP powder prior to sintering. After sintering to 1200 °C, phase transition occurs and only β-TCP remains in the white parts.

Scaffold manufacturing indicates a maximum feasible wall thickness of approximately 3 mm, as seen by crack formation when this limit is exceeded. Accordingly, with the exception of the Kagome structure, 25 % porous scaffolds could not be manufactured. Only 50 % and 75 % porosities were achieved without the formation of visible defects.

µ-CT measurements show that manufactured scaffolds have up to 20 vol.% lower porosities and up to 100 µm smaller pores than designated according to CAD. By introduction of an experimentally determined scaling factor, the accuracy of pore sizes could be significantly improved for both the cylinder grid and the Kagome structures to accuracies of ± 23 µm and porosity was improved to fall within an error margin of ± 9 vol.%.

Static compressive testing yields satisfactory results, as depicted in Figure 46. Especially the Kagome scaffolds do not quite reach the compressive strengths desired for cortical bone at the same density, but they are well within the expected range of similar scaffolds [91]. Although this characterization method gives a good first estimate of the mechanical properties of the scaffolds, other essential factors such as brittleness, behavior under cyclic loading, and potential anisotropies have not been characterized and would be needed before consideration as load bearing scaffolds.

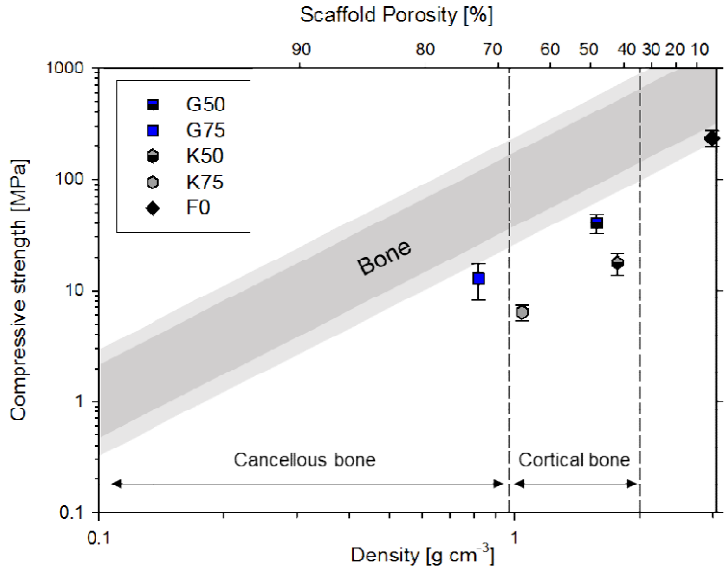


*Figure 46: Compressive strengths of manufactured scaffolds compared to predictions for bone. Upper limit was taken from* [162] *and lower limit from* [163] *with 30 % margin of error marked in light gray. Figure adapted from* [91].

The TCP structures are stable in SBF for 21 days, with no significant change in mass or composition. According to µ-CT measurements, only the Kagome structure shows an increase in volume. Surface properties are modified by exposure to SBF, as investigated in SEM images, with an increase in the number of intergranular pores.

Cell culture experiments show that all scaffolds support growth of MC3T3-E1 cells for at least 14 days at more than 2.6 ± 0.3 fold increased seeding efficiencies than on non-porous TCP cubes. After that, a decrease in DNA can be observed for the 3D as well as for the 2D conditions, pointing towards a

cause unrelated to the scaffolds. Furthermore, at 14 days of cell culture, a maximum of ALP activity indicates osteogenic differentiation for all scaffolds. ALP activity is higher for the 75 % porosity structures as opposed to the 50 % porous ones at all time-points by an average factor of 1.6 ± 0.4.

When comparing cylinder grid and Kagome architectures, no significant differences can be observed in any of the cell culture experiments, although DNA quantification does indicate a tendency of higher cell numbers on the Kagome scaffolds. A remarkable trend is that the hexagonal pores in the Kagome architecture are more prominently filled by actin stress fibers by day 7 than the rectangular grid pores. Perhaps relatedly, initial collagen deposition up until day 7 is higher in the Kagome scaffolds.

Next to the high accuracy, the DLP manufacturing method has revealed another potential advantage of inducing cell alignment along the 20 µm spaced layers. This could affect cell adhesion but also gene expression and differentiation behavior [164], necessitating further investigation.

Considering the excellent geometrical reproducibility, superior mechanical properties, and absence of a significant difference in cell interaction to the Kagome architectures, especially the grid structures could be promising for future applications in bone TE. By selecting scaffold porosities, stiffness and strength can be tuned according to prospective future applications, while keeping in mind that higher porosities are beneficial for ALP activity. Extensive further studies are needed, however, to fully characterize osteogenic differentiation and to asses bone tissue formation.

# 6. Appendix

## 6.1 Construction of Scaffolds

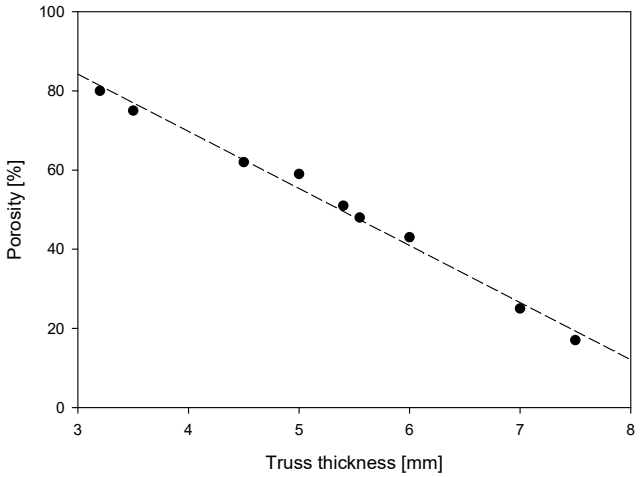


*Appendix 1: Truss diameter of the Kagome structure specified in SOLIDWORKS for truss lengths of 10 mm plotted against resulting scaffold porosity according to NetFabb with linear regression.*

## 6.2: Manufactured Cube

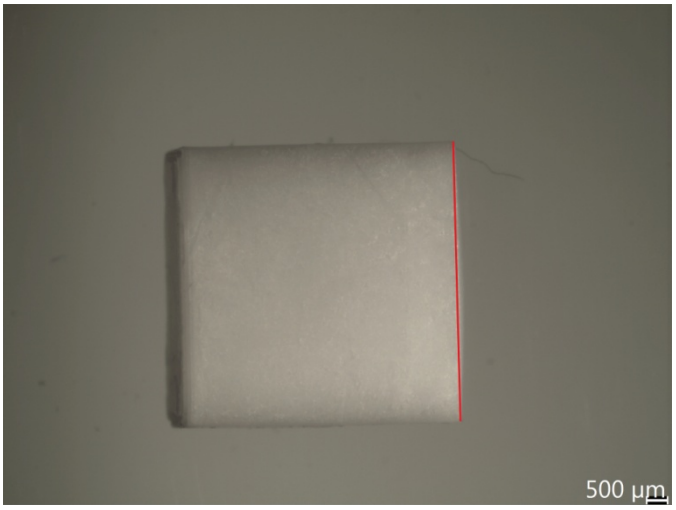


*Appendix 2: Light microscopy image of an F0 6x6x6 mm manufactured cube with red line highlighting a bulge in the top surface parallel to the manufacturing layers.*

## 6.3 XPS spectra

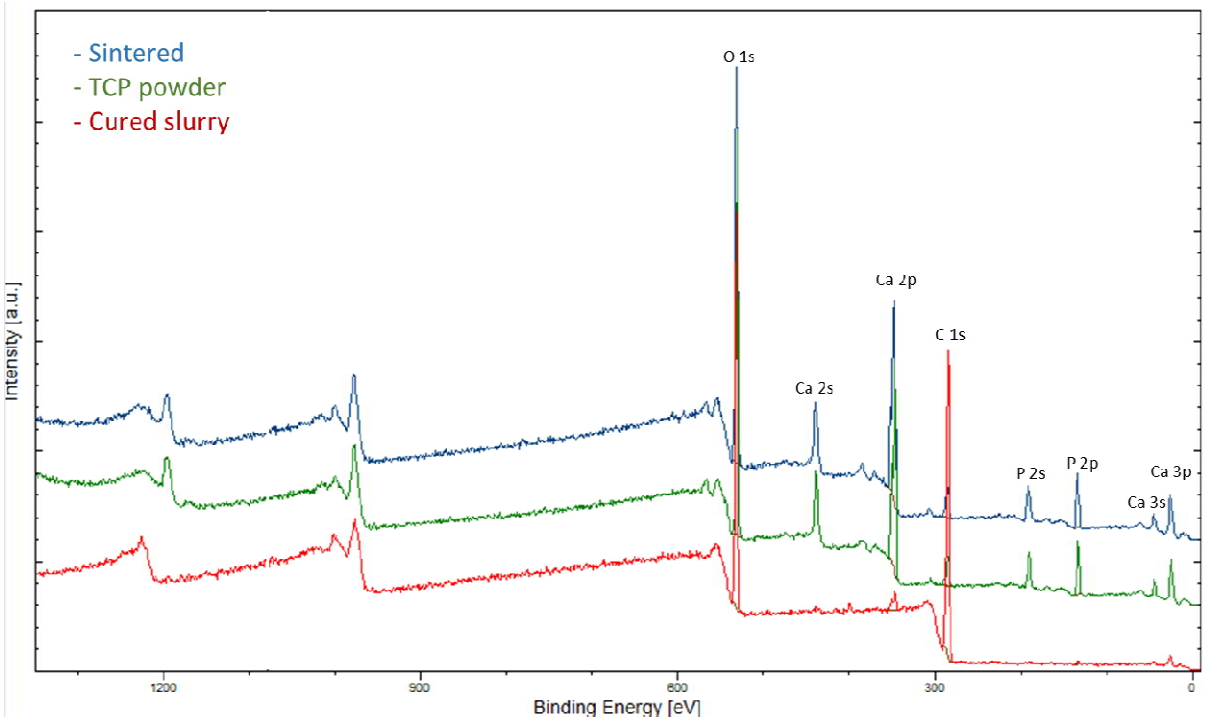


*Appendix 3.1: XPS spectrum of cured slurry(dried at 120 °C for 72 h), TCP powder, and sintered F0 part; before argon-ion etching.*

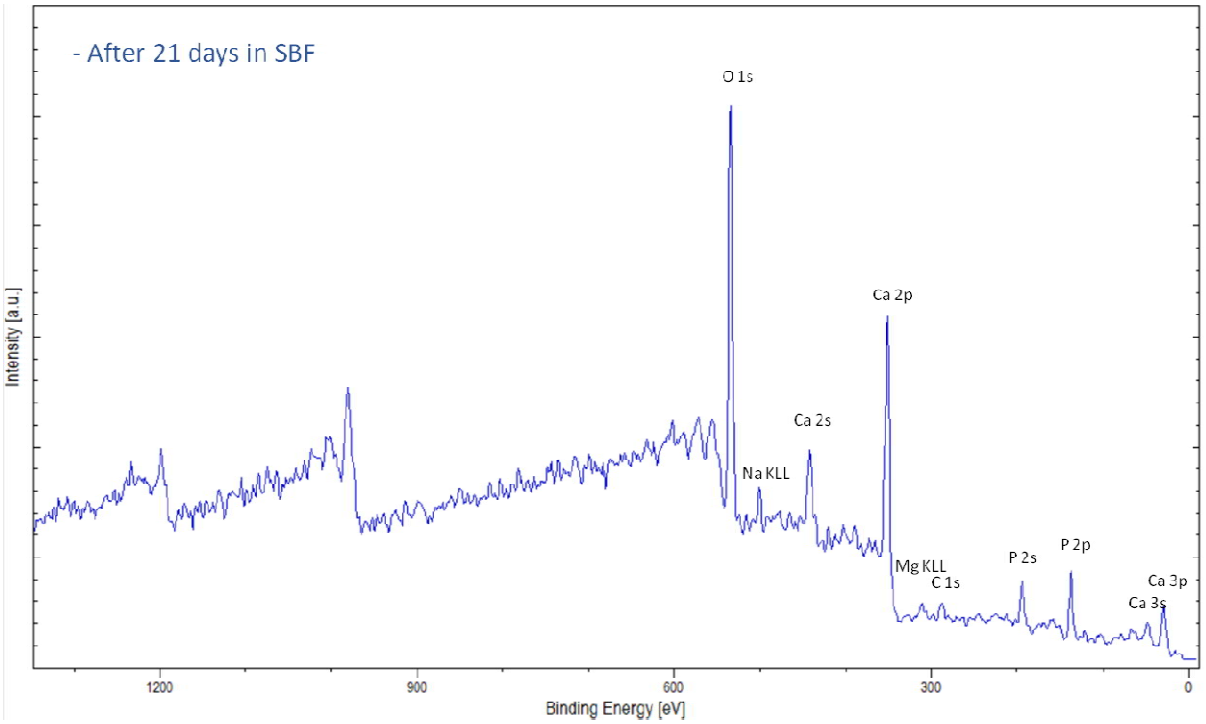


*Appendix 3.2: XPS spectrum of TCP G75 scaffold after exposure to SBF for 21 days.*

## 6.4 XRD spectra

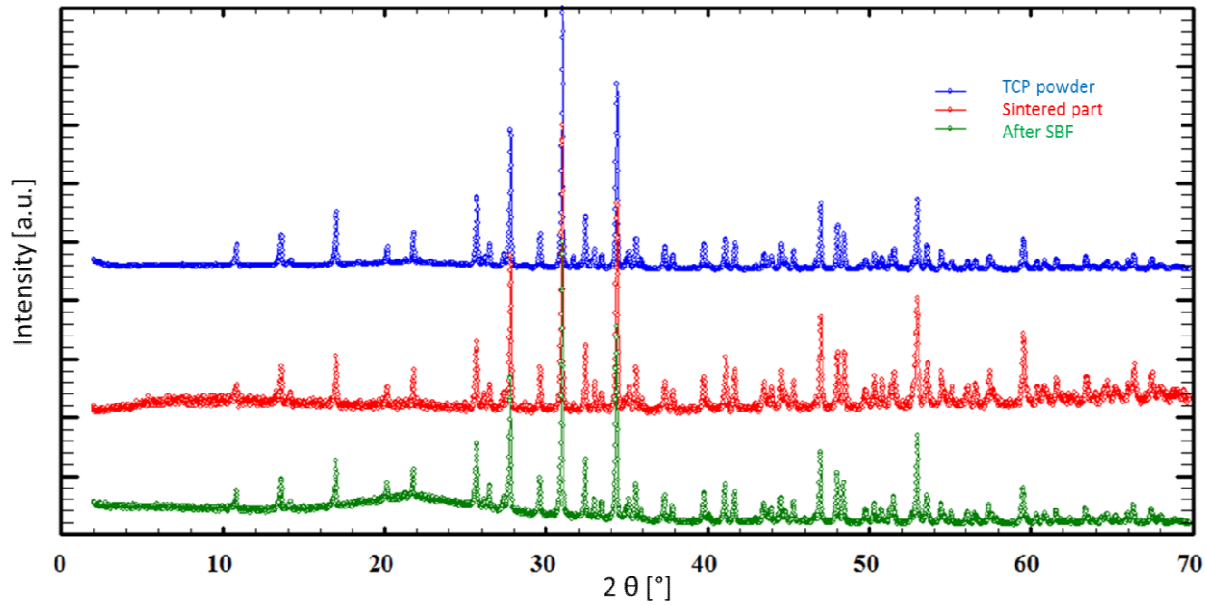


*Appendix 4: Powder XRD spectrum of TCP powder prior to processing, of sintered parts, and of sintered parts after immersion in SBF for 21 days.*

## 6.5 µ-CT Measurements

*Appendix 5: Raw data of µ-CT measurements perpendicular to x and y axes (yz and xz planes) and perpendicular to z axis (xy-plane) on the specimen surfaces and centers with specifications (specs.) as comparison.*

| | Unit cell size [µm] | | Pore size [µm] | | | | | Porosity [%] | |
|---|---|---|---|---|---|---|---|---|---|
| | µ-CT | specs | xz+yz, surface | xz+yz, center | xy, surface | xy, center | specs | µ-CT | specs |
| **G75** | 638 ± 9.3 | 690 | 411 ± 8.3 | 388 ± 7.0 | 396 ± 18 | 363 ± 12 | 460 | 63.63 | 75 |
| **G50** | 1040 ± 15 | 1030 | 438 ± 14 | 406 ± 13 | 408 ± 7.3 | 378 ± 7.0 | 476 | 30.15 | 50 |
| **G25** | 2045 ± 27 | 2000 | 358 ± 12 | | 339 ± 26 | | 450 | 18.80 | 25 |
| **S50** | 700 ± 17 | 690 | 424 ± 4.2 | 405 ± 13 | 386 ± 11 | 335 ± 9.4 | 460 | 64.56 | 75 |
| **S75** | 1040 ± 18 | 1030 | 431 ± 15 | 398 ± 16 | 391 ± 11 | 348 ± 22 | 460 | 42.10 | 50 |
| **H75** | 1487 ± 17 | 1450 | 428 ± 19 | 416 ± 18 | 426 ± 13 | 441 ± 8.3 | 500 | 65.23 | 75 |
| **H50** | 4056 ± 52 | 4000 | 374 ± 66 | | 493 ± 29 | | 500 | 48.87 | 50 |
| **K75** | 991 ± 20 | 1000 | - | - | 552 ± 10 | 565 ±8.2 | 600 | 64.44 | 69 |
| **K50** | 1020 ± 13 | 1040 | - | - | 481 ± 6.1 | 485 ± 17 | 540 | 52.36 | 56 |
| **K25** | 1707 ± 35 | 1700 | - | - | 478 ± 18 | 506 ± 15 | 540 | 26.20 | 30 |
| **G75B** | 651 ± 16 | 650 | 438 ± 27 | 420 ± 18 | 429 ± 13 | 409 ± 12 | 400 | 73.14 | 75 |
| **G50B** | 888 ± 15 | 880 | 400 ± 7.5 | 388 ± 7.5 | 389 ± 4.5 | 402 ± 11 | 400 | 48.37 | 50 |
| **K75B** | 682 ± 5.7 | 680 | - | - | 393 ± 6.4 | 383 ± 9.9 | 400 | 65.84 | 75 |
| **K50B** | 930 ± 22 | 940 | - | - | 395 ± 9.8 | 377 ± 11 | 400 | 42.13 | 50 |

## 6.6 Negative Controls

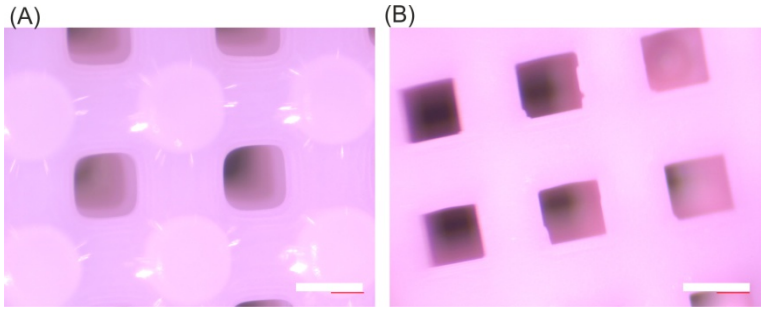


*Appendix 6: Negative control of (A): collagen and (B): calcium staining. Scale bars are 400 µm.*

# 7. Bibliography


[1] F. Borgström *et al.*, "The International Costs and Utilities Related to Osteoporotic Fractures Study (ICUROS)—quality of life during the first 4 months after fracture," *Osteoporos. Int.*, vol. 24, no. 3, pp. 811–823, Mar. 2013.

[2] H. Yuan *et al.*, "Osteoinductive ceramics as a synthetic alternative to autologous bone grafting.," *Proc. Natl. Acad. Sci. U. S. A.*, vol. 107, no. 31, pp. 13614–9, Aug. 2010.

[3] B. P. Chan and K. W. Leong, "Scaffolding in tissue engineering: general approaches and tissue-specific considerations.," *Eur. Spine J.*, vol. 17 Suppl 4, no. Suppl 4, pp. 467–79, Dec. 2008.

[4] F. J. O'Brien, "Biomaterials & scaffolds for tissue engineering," *Mater. Today*, vol. 14, no. 3, pp. 88–95, Mar. 2011.

[5] T. Grimm, *User's guide to rapid prototyping*. Society of Manufacturing Engineers, 2004.

[6] C. Sun, N. Fang, D. M. Wu, and X. Zhang, "Projection micro-stereolithography using digital micro-mirror dynamic mask," *Sensors Actuators A Phys.*, vol. 121, no. 1, pp. 113–120, May 2005.

[7] Y. Lu, G. Mapili, G. Suhali, S. Chen, and K. Roy, "A digital micro-mirror device-based system for the microfabrication of complex, spatially patterned tissue engineering scaffolds," *J. Biomed. Mater. Res. Part A*, vol. 77A, no. 2, pp. 396–405, May 2006.

[8] L.-H. Han, G. Mapili, S. Chen, and K. Roy, "Projection Microfabrication of Three-Dimensional Scaffolds for Tissue Engineering," *J. Manuf. Sci. Eng.*, vol. 130, no. 2, p. 021005, Apr. 2008.

[9] G. Katal, N. Tyagi, and A. Joshi, "Digital Light Processing and its Future Applications," *Int. J. Sci. Res. Publ.*, vol. 3, no. 1, pp. 2250–3153, 2013.

[10] L. J. Hornbeck, "Digital Light Processing™: A New MEMS-Based Display Technology."

[11] S. Waheed *et al.*, "3D printed microfluidic devices: enablers and barriers," *Lab Chip*, vol. 16, no. 11, pp. 1993–2013, May 2016.

[12] Y. Pan, C. Zhou, and Y. Chen, "A Fast Mask Projection Stereolithography Process for Fabricating Digital Models in Minutes," *J. Manuf. Sci. Eng.*, vol. 134, no. 5, p. 051011, Oct. 2012.

[13] Y.-M. Huang, S. Kuriyama, and C.-P. Jiang, "Fundamental study and theoretical analysis in a constrained-surface stereolithography system," *Int. J. Adv. Manuf. Technol.*, vol. 24, no. 5–6, pp. 361–369, Sep. 2004.

[14] J. Choi, R. B. Wicker, S. Cho, C. Ha, and S. Lee, "Cure depth control for complex 3D microstructure fabrication in dynamic mask projection microstereolithography," *Rapid Prototyp. J.*, vol. 15, no. 1, pp. 59–70, Jan. 2009.

[15] M. Hatzenbichler, M. Geppert, R. Seemann, and J. Stampfl, "Additive manufacturing of photopolymers using the Texas Instruments DLP lightcrafter," in *Proceedings of SPIE 8618, Emerging Digital Micromirror Device Based Systems and Applications V*, 2013, vol. 8618, p. 86180A.

[16] Y.-M. Huang and C.-P. Jiang, "On-line force monitoring of platform ascending rapid prototyping system," *J. Mater. Process. Technol.*, vol. 159, no. 2, pp. 257–264, Jan. 2005.

[17] Y. Chen and C. Zhou, "Digital mask-image-projection-based additive manufacturing that applies shearing force to detach each added layer," US13872954, 29-Apr-2013.

[18] M. Schwentenwein and J. Homa, "Additive manufacturing of dense alumina ceramics," *Int. J. Appl. Ceram. Technol.*, vol. 12, no. 1, pp. 1–7, 2015.

[19] F. P. W. Melchels, J. Feijen, and D. W. Grijpma, "A review on stereolithography and its

applications in biomedical engineering," *Biomaterials*, vol. 31, no. 24, pp. 6121–6130, 2010.

[20] S. C. Ligon, R. Liska, J. Stampfl, M. Gurr, and R. Mülhaupt, "Polymers for 3D Printing and Customized Additive Manufacturing.," *Chem. Rev.*, vol. 117, no. 15, pp. 10212–10290, Aug. 2017.

[21] S. Maruo and K. Ikuta, "Submicron stereolithography for the production of freely movable mechanisms by using single-photon polymerization," *Sensors Actuators A Phys.*, vol. 100, no. 1, pp. 70–76, Aug. 2002.

[22] S.-H. Park, D.-Y. Yang, and K.-S. Lee, "Two-photon stereolithography for realizing ultraprecise three-dimensional nano/microdevices," *Laser Photonics Rev.*, vol. 3, no. 1–2, pp. 1–11, 2009.

[23] K.-S. Lee, R. H. Kim, D.-Y. Yang, and S. H. Park, "Advances in 3D nano/microfabrication using two-photon initiated polymerization," *Prog. Polym. Sci.*, vol. 33, no. 6, pp. 631–681, Jun. 2008.

[24] C. W. Hull, "Apparatus for production of three-dimensional objects by stereolithography," US4575330B1, 08-Aug-1984.

[25] E. J. Murphy, R. E. Ansel, and J. J. Krajewski, "Method of forming a three-dimensional object by stereolithography and composition therefore," US07429568, 31-Oct-1989.

[26] J. Stampfl *et al.*, "Photopolymers with tunable mechanical properties processed by laser-based high-resolution stereolithography," *J. Micromechanics Microengineering*, vol. 18, no. 12, p. 125014, Dec. 2008.

[27] A. L. Coats, J. P. Harrison, J. S. Hay, and Ramos Manuel Jacinto, "Stereolithography resins and methods," US10628304, 29-Jul-2003.

[28] J. V. Crivello, "The discovery and development of onium salt cationic photoinitiators," *J. Polym. Sci. Part A Polym. Chem.*, vol. 37, no. 23, pp. 4241–4254, Dec. 1999.

[29] J. V. Crivello, S. Kong, and M. Jang, "Cationic Polymerization: New Developments and Applications," *Macromol. Symp.*, vol. 217, no. 1, pp. 47–62, Oct. 2004.

[30] V. Sipani and A. B. Scranton, "Kinetic studies of cationic photopolymerizations of phenyl glycidyl ether: termination/trapping rate constants for iodonium photoinitiators," *J. Photochem. Photobiol. A Chem.*, vol. 159, no. 2, pp. 189–195, Jul. 2003.

[31] C. Esposito Corcione, A. Greco, and A. Maffezzoli, "Photopolymerization kinetics of an epoxy-based resin for stereolithography," *J. Appl. Polym. Sci.*, vol. 92, no. 6, pp. 3484–3491, Jun. 2004.

[32] G. Zhiwei, M. Jianhua, H. Shuhuai, and X. Hongquan, "Development of a hybrid photopolymer for stereolithography," *J. Wuhan Univ. Technol. Sci. Ed.*, vol. 21, no. 1, pp. 99–101, Mar. 2006.

[33] A. Badev *et al.*, "Photopolymerization kinetics of a polyether acrylate in the presence of ceramic fillers used in stereolithography," *J. Photochem. Photobiol. A Chem.*, vol. 222, no. 1, pp. 117–122, Jul. 2011.

[34] R. Bail *et al.*, "The Effect of a Type I Photoinitiator on Cure Kinetics and Cell Toxicity in Projection-Microstereolithography," *Procedia CIRP*, vol. 5, pp. 222–225, Jan. 2013.

[35] I. Mironi-Harpaz, D. Y. Wang, S. Venkatraman, and D. Seliktar, "Photopolymerization of cell-encapsulating hydrogels: Crosslinking efficiency versus cytotoxicity," *Acta Biomater.*, vol. 8, no. 5, pp. 1838–1848, May 2012.

[36] K. T. Nguyen and J. L. West, "Photopolymerizable hydrogels for tissue engineering applications," *Biomaterials*, vol. 23, no. 22, pp. 4307–4314, Nov. 2002.

[37] S. J. Bryant, C. R. Nuttelman, and K. S. Anseth, "Cytocompatibility of UV and visible light photoinitiating systems on cultured NIH/3T3 fibroblasts in vitro.," *J. Biomater. Sci. Polym. Ed.*,

vol. 11, no. 5, pp. 439–57, 2000.

[38] J.-W. Choi *et al.*, “Fabrication of 3D biocompatible/biodegradable micro-scaffolds using dynamic mask projection microstereolithography,” *J. Mater. Process. Technol.*, vol. 209, pp. 5494–5503, 2009.

[39] R. Bail, J. Y. Hong, and B. D. Chin, “Effect of a red-shifted benzotriazole UV absorber on curing depth and kinetics in visible light initiated photopolymer resins for 3D printing,” *J. Ind. Eng. Chem.*, vol. 38, pp. 141–145, 2016.

[40] C. Hinczewski, S. Corbel, and T. Chartier, “Ceramic suspensions suitable for stereolithography,” *J. Eur. Ceram. Soc.*, vol. 18, no. 6, pp. 583–590, Jan. 1998.

[41] P. J. Bartolo and J. Gaspar, “Metal filled resin for stereolithography metal part,” *CIRP Ann.*, vol. 57, no. 1, pp. 235–238, Jan. 2008.

[42] W. Zimbeck and M. Pope, “Microstructures and Strengths of Metals and Ceramics made by Photopolymer- based Rapid Prototyping.”

[43] A. de Blas Romero *et al.*, “Lithography-based additive manufacture of ceramic biodevices with design-controlled surface topographies,” *Int. J. Adv. Manuf. Technol.*, vol. 88, no. 5–8, pp. 1547–1555, 2017.

[44] I. Manjubala *et al.*, “Biomimetic mineral-organic composite scaffolds with controlled internal architecture,” *J Mater Sci Mater Med*, vol. 16, no. 12, pp. 1111–1119, 2005.

[45] X. Wang, M. Jiang, Z. Zhou, J. Gou, and D. Hui, “3D printing of polymer matrix composites: A review and prospective,” *Compos. Part B Eng.*, vol. 110, pp. 442–458, Feb. 2017.

[46] C. V. Adake, P. Gandhi, and P. Bhargava, “Fabrication of Ceramic Component Using Constrained Surface Microstereolithography,” *Procedia Mater. Sci.*, vol. 5, pp. 355–361, Jan. 2014.

[47] V. Tomeckova and J. W. Halloran, “Flow behavior of polymerizable ceramic suspensions as function of ceramic volume fraction and temperature,” *J. Eur. Ceram. Soc.*, vol. 31, no. 14, pp. 2535–2542, Nov. 2011.

[48] Y. De Hazan, J. Heinecke, A. Weber, and T. Graule, “High solids loading ceramic colloidal dispersions in UV curable media via comb-polyelectrolyte surfactants,” *J. Colloid Interface Sci.*, vol. 337, no. 1, pp. 66–74, Sep. 2009.

[49] L. Elomaa, S. Teixeira, R. Hakala, H. Korhonen, D. W. Grijpma, and J. V. Seppälä, “Preparation of poly(ε-caprolactone)-based tissue engineering scaffolds by stereolithography,” *Acta Biomater.*, vol. 7, no. 11, pp. 3850–3856, Nov. 2011.

[50] W. D. Teng, M. J. Edirisinghe, and J. R. G. Evans, “Optimization of Dispersion and Viscosity of a Ceramic Jet Printing Ink,” *J. Am. Ceram. Soc.*, vol. 80, no. 2, pp. 486–494, 1997.

[51] K. Li and Z. Zhao, “The effect of the surfactants on the formulation of UV-curable SLA alumina suspension,” *Ceram. Int.*, vol. 43, no. 6, pp. 4761–4767, Apr. 2017.

[52] A. Goswami, K. Ankit, N. Balashanmugam, A. M. Umarji, and G. Madras, “Optimization of rheological properties of photopolymerizable alumina suspensions for ceramic microstereolithography,” *Ceram. Int.*, vol. 40, no. 2, pp. 3655–3665, 2014.

[53] M. L. Griffith and J. W. Halloran, “Scattering of ultraviolet radiation in turbid suspensions,” *J. Appl. Phys.*, vol. 81, no. 47, pp. 2538–24902, 1997.

[54] S. P. Gentry and J. W. Halloran, “Light scattering in absorbing ceramic suspensions: Effect on the width and depth of photopolymerized features,” *J. Eur. Ceram. Soc.*, vol. 35, no. 6, pp. 1895–1904, Jun. 2015.

[55] C. Sun and X. Zhang, “The influences of the material properties on ceramic micro-stereolithography,” *Sensors Actuators A Phys.*, vol. 101, no. 3, pp. 364–370, Oct. 2002.

[56] E. F. MORGAN, G. L. BARNES, and T. A. EINHORN, “CHAPTER 1 - The Bone Organ System: Form and Function,” in *Osteoporosis*, Academic Press, 2008, pp. 3–25.

[57] J. G. Betts *et al.*, “Chapter 6. Bone Tissue and the Skeletal System,” in *Anatomy & Physiology*, OpenStax College, Rice University, 2013.

[58] A. Rutkovskiy, K.-O. Stensløkken, and I. J. Vaage, “Osteoblast Differentiation at a Glance,” *Med. Sci. Monit. Basic Res.*, vol. 22, pp. 95–106, 2016.

[59] G. R. Beck, B. Zerler, and E. Moran, “Gene array analysis of osteoblast differentiation.,” *Cell Growth Differ.*, vol. 12, no. 2, pp. 61–83, 2001.

[60] A. K. Nair, A. Gautieri, S.-W. Chang, and M. J. Buehler, “Molecular mechanics of mineralized collagen fibrils in bone,” *Nat. Commun.*, vol. 4, no. 1, p. 1724, Dec. 2013.

[61] K. J. Koester, J. W. Ager, and R. O. Ritchie, “The true toughness of human cortical bone measured with realistically short cracks,” *Nat. Mater.*, vol. 7, no. 8, pp. 672–677, Aug. 2008.

[62] D. Vashishth, “Rising crack-growth-resistance behavior in cortical bone:: implications for toughness measurements,” *J. Biomech.*, vol. 37, no. 6, pp. 943–946, Jun. 2004.

[63] M. Bienz and F. Saad, “Androgen-deprivation therapy and bone loss in prostate cancer patients: a clinical review,” *Bonekey Rep.*, vol. 4, Jun. 2015.

[64] A. J. Wagoner Johnson and B. A. Herschler, “A review of the mechanical behavior of CaP and CaP/polymer composites for applications in bone replacement and repair,” *Acta Biomater.*, vol. 7, no. 1, pp. 16–30, Jan. 2011.

[65] D. R. Carter and W. C. Hayes, “Bone compressive strength: the influence of density and strain rate.,” *Science*, vol. 194, no. 4270, pp. 1174–6, Dec. 1976.

[66] S. H. Ralston, “Bone structure and metabolism,” *Medicine (Baltimore).*, vol. 41, no. 10, pp. 581–585, Oct. 2013.

[67] D. J. HADJIDAKIS and I. I. ANDROULAKIS, “Bone Remodeling,” *Ann. N. Y. Acad. Sci.*, vol. 1092, no. 1, pp. 385–396, Dec. 2006.

[68] X. Feng and J. M. McDonald, “Disorders of bone remodeling.,” *Annu. Rev. Pathol.*, vol. 6, pp. 121–45, 2011.

[69] M. G. Joshi, S. G. Advani, F. Miller, and M. H. Santare, “Analysis of a femoral hip prosthesis designed to reduce stress shielding,” *J. Biomech.*, vol. 33, no. 12, pp. 1655–1662, Dec. 2000.

[70] M. I. Z. Ridzwan, S. Shuib, A. Y. Hassan, A. A. Shokri, and M. N. M. Ibrahim, “Problem of Stress Shielding and Improvement to the Hip Implant Designs: A Review,” *J. Med. Sci.*, vol. 7, no. 3, pp. 460–467, Mar. 2007.

[71] Y. Fillingham and J. Jacobs, “Bone grafts and their substitutes,” *Bone Joint J.*, vol. 98–B, no. 1_Supple_A, pp. 6–9, Jan. 2016.

[72] G. E. Friedlaender, “Immune responses to osteochondral allografts. Current knowledge and future directions.,” *Clin. Orthop. Relat. Res.*, no. 174, pp. 58–68, Apr. 1983.

[73] E. Chiarello *et al.*, “Autograft, allograft and bone substitutes in reconstructive orthopedic surgery,” *Aging CLin Exp Res*, vol. 25, pp. 101–103, 2013.

[74] C. Xie *et al.*, “Structural Bone Allograft Combined with Genetically Engineered Mesenchymal Stem Cells as a Novel Platform for Bone Tissue Engineering,” *Tissue Eng.*, vol. 13, no. 3, pp. 435–445, Mar. 2007.

[75] M. A. Flierl *et al.*, “Outcomes and complication rates of different bone grafting modalities in long bone fracture nonunions: a retrospective cohort study in 182 patients,” *J. Orthop. Surg. Res.*, vol. 8, no. 1, p. 33, Sep. 2013.

[76] H. C. Pape, A. Evans, and P. Kobbe, “Autologous Bone Graft: Properties and Techniques,” *J. Orthop. Trauma*, vol. 24, pp. S36–S40, Mar. 2010.

[77] E. D. Arrington, W. J. Smith, H. G. Chambers, A. L. Bucknell, and N. A. Davino, “Complications of iliac crest bone graft harvesting.,” *Clin. Orthop. Relat. Res.*, no. 329, pp. 300–9, Aug. 1996.

[78] E. M. Younger and M. W. Chapman, “Morbidity at bone graft donor sites.,” *J. Orthop. Trauma*, vol. 3, no. 3, pp. 192–5, 1989.

[79] H. Kausar and R. N. Kishore, “BONE TISSUE ENGINEERING,” *Int. J. Pharm. Pharm. Sci.* , vol. 5, no. 1, pp. 30–32, 2013.

[80] D. Williams, *Definitions in Biomaterials. Progress in Biomedical Engineering*. Amsterdam: Elsevier, 1987.

[81] J. Liu, S. Willför, and A. Mihranyan, “On importance of impurities, potential leachables and extractables in algal nanocellulose for biomedical use,” *Carbohydr. Polym.*, vol. 172, pp. 11–19, Sep. 2017.

[82] R. G. M. Breuls, T. U. Jiya, and T. H. Smit, “Scaffold Stiffness Influences Cell Behavior: Opportunities for Skeletal Tissue Engineering,” *Open Orthop. J.*, vol. 2, pp. 103–9, May 2008.

[83] and A. B. Susmita Bose, Mangal Roy, “Recent advances in bone tissue engineering scaffolds,” *Trends Biotechnol.*, vol. 30, no. 10, pp. 546–554, 2012.

[84] T. Alberktsson and C. Johansson, “Osteoinduction, osteoconduction and osseointegration,” *Eur Spine J*, vol. 10, pp. 96–101, 2001.

[85] L. Malladi, A. Mahapatro, and A. S. Gomes, “Fabrication of magnesium-based metallic scaffolds for bone tissue engineering,” *Mater. Technol.*, vol. 33, no. 2, pp. 173–182, Jan. 2018.

[86] L. Roseti *et al.*, “Scaffolds for Bone Tissue Engineering: State of the art and new perspectives,” *Mater. Sci. Eng. C*, vol. 78, pp. 1246–1262, 2017.

[87] X. Liu and P. X. Ma, “Polymeric Scaffolds for Bone Tissue Engineering,” *Ann. Biomed. Eng.*, vol. 32, no. 3, pp. 477–486, 2004.

[88] Q. Fu, E. Saiz, M. N. Rahaman, and A. P. Tomsia, “Bioactive glass scaffolds for bone tissue engineering: state of the art and future perspectives.,” *Mater. Sci. Eng. C. Mater. Biol. Appl.*, vol. 31, no. 7, pp. 1245–1256, Oct. 2011.

[89] S. Samavedi, A. R. Whittington, and A. S. Goldstein, “Calcium phosphate ceramics in bone tissue engineering: A review of properties and their influence on cell behavior,” *Acta Biomater.*, vol. 9, no. 9, pp. 8037–8045, Sep. 2013.

[90] W. Habraken, P. Habibovic, M. Epple, and M. Bohner, “Calcium phosphates in biomedical applications: materials for the future?,” *Mater. Today*, vol. 19, no. 2, pp. 69–87, Mar. 2016.

[91] P. Miranda, A. Pajares, E. Saiz, A. P. Tomsia, and F. Guiberteau, “Mechanical properties of calcium phosphate scaffolds fabricated by robocasting,” *J. Biomed. Mater. Res. Part A*, vol. 85A, no. 1, pp. 218–227, Apr. 2008.

[92] S. E. Lobo and T. Livingston Arinzeh, “Biphasic Calcium Phosphate Ceramics for Bone Regeneration and Tissue Engineering Applications,” *Materials (Basel).*, vol. 3, no. 2, pp. 815–826, Jan. 2010.

[93] T. Ghassemi, A. Shahroodi, M. H. Ebrahimzadeh, A. Mousavian, J. Movaffagh, and A. Moradi, “Current Concepts in Scaffolding for Bone Tissue Engineering.,” *Arch. bone Jt. Surg.*, vol. 6, no.

2, pp. 90–99, Mar. 2018.

[94] N. Zhao, Y. Wang, L. Qin, Z. Guo, and D. Li, “Effect of composition and macropore percentage on mechanical and in vitro cell proliferation and differentiation properties of 3D printed HA/β-TCP scaffolds,” *RSC Adv.*, vol. 7, no. 68, pp. 43186–43196, Sep. 2017.

[95] S. F. Hulbert, F. A. Young, R. S. Mathews, J. J. Klawitter, C. D. Talbert, and F. H. Stelling, “Potential of ceramic materials as permanently implantable skeletal prostheses,” *J. Biomed. Mater. Res.*, vol. 4, no. 3, pp. 433–456, Sep. 1970.

[96] D. Druecke *et al.*, “Neovascularization of poly(ether ester) block-copolymer scaffoldsin vivo: Long-term investigations using intravital fluorescent microscopy,” *J. Biomed. Mater. Res.*, vol. 68A, no. 1, pp. 10–18, Jan. 2004.

[97] Q. M. Jin, H. Takita, T. Kohgo, K. Atsumi, H. Itoh, and Y. Kuboki, “Effects of geometry of hydroxyapatite as a cell substratum in BMP-induced ectopic bone formation.,” *J. Biomed. Mater. Res.*, vol. 51, no. 3, pp. 491–9, 2000.

[98] Y. Kuboki, Q. Jin, M. Kikuchi, J. Mamood, and H. Takita, “Geometry of Artificial ECM: Sizes of Pores Controlling Phenotype Expression in BMP-Induced Osteogenesis and Chondrogenesis,” *Connect. Tissue Res.*, vol. 43, no. 2–3, pp. 529–534, Jan. 2002.

[99] Y. Kuboki *et al.*, “BMP-Induced osteogenesis on the surface of hydroxyapatite with geometrically feasible and nonfeasible structures: Topology of osteogenesis,” *J Biomed Mater Res*, vol. 39, pp. 190–199, 1998.

[100] B. Feng *et al.*, “The effect of pore size on tissue ingrowth and neovascularization in porous bioceramics of controlled architecture in vivo,” *Biomed. Mater.*, vol. 6, no. 1, p. 015007, Feb. 2011.

[101] Y. Kuboki, Q. Jin, and H. Takita, “Geometry of carriers controlling phenotypic expression in BMP-induced osteogenesis and chondrogenesis.,” *J. Bone Joint Surg. Am.*, vol. 83–A Suppl 1, no. Pt 2, pp. S105-15, 2001.

[102] C. M. Murphy, M. G. Haugh, and F. J. O’Brien, “The effect of mean pore size on cell attachment, proliferation and migration in collagen–glycosaminoglycan scaffolds for bone tissue engineering,” *Biomaterials*, vol. 31, no. 3, pp. 461–466, Jan. 2010.

[103] E. Tsuruga, H. Takita, H. Itoh, Y. Wakisaka, and Y. Kuboki, “Pore Size of Porous Hydroxyapatite as the Cell-Substratum Controls BMP-Induced Osteogenesis,” *J. Biochem.*, vol. 121, no. 2, pp. 317–324, 1997.

[104] J. R. Woodard *et al.*, “The mechanical properties and osteoconductivity of hydroxyapatite bone scaffolds with multi-scale porosity,” *Biomaterials*, vol. 28, no. 1, pp. 45–54, Jan. 2007.

[105] P. Habibovic, H. Yuan, C. M. van der Valk, G. Meijer, C. A. van Blitterswijk, and K. de Groot, “3D microenvironment as essential element for osteoinduction by biomaterials,” *Biomaterials*, vol. 26, no. 17, pp. 3565–3575, Jun. 2005.

[106] V. Karageorgiou and D. Kaplan, “Porosity of 3D biomaterial scaffolds and osteogenesis,” *Biomaterials*, vol. 26, pp. 5474–5491, 2005.

[107] A. S. G. Curtis, N. Gadegaard, M. J. Dalby, M. O. Riehle, C. D. W. Wilkinson, and G. Aitchison, “Cells React to Nanoscale Order and Symmetry in Their Surroundings,” *IEEE Trans. Nanobioscience*, vol. 3, no. 1, pp. 61–65, Mar. 2004.

[108] M. M. Stevens and J. H. George, “Exploring and engineering the cell surface interface.,” *Science*, vol. 310, no. 5751, pp. 1135–8, Nov. 2005.

[109] C. M. Bidan, K. P. Kommareddy, M. Rumpler, P. Kollmannsberger, P. Fratzl, and J. W. C. Dunlop, “Geometry as a Factor for Tissue Growth: Towards Shape Optimization of Tissue

Engineering Scaffolds," *Adv. Healthc. Mater.*, vol. 2, no. 1, pp. 186–194, 2013.

[110] M. Rumpler, A. Woesz, J. W. C. Dunlop, J. T. Van Dongen, and P. Fratzl, "The effect of geometry on three-dimensional tissue growth."

[111] S. Park, G. Kim, Y. C. Jeon, Y. Koh, and W. Kim, "3D polycaprolactone scaffolds with controlled pore structure using a rapid prototyping system," *J. Mater. Sci. Mater. Med.*, vol. 20, no. 1, pp. 229–234, Jan. 2009.

[112] S.-I. Roohani-Esfahani, P. Newman, and H. Zreiqat, "Design and Fabrication of 3D printed Scaffolds with a Mechanical Strength Comparable to Cortical Bone to Repair Large Bone Defects," *Sci. Rep.*, vol. 6, no. 1, p. 19468, May 2016.

[113] D. Loca, I. Narkevica, and J. Ozolins, "The effect of TiO2 nanopowder coating on in vitro bioactivity of porous TiO2 scaffolds," *Mater. Lett.*, vol. 159, pp. 309–312, Nov. 2015.

[114] T. Kuang *et al.*, "Facile preparation of open-cellular porous poly (l-lactic acid) scaffold by supercritical carbon dioxide foaming for potential tissue engineering applications," *Chem. Eng. J.*, vol. 307, pp. 1017–1025, Jan. 2017.

[115] V. S. Deshpande, N. A. Fleck, and M. F. Ashby, "Effective properties of the octet-truss lattice material," *J. Mech. Phys. Solids*, vol. 49, no. 8, pp. 1747–1769, Aug. 2001.

[116] L. Dong, V. Deshpande, and H. Wadley, "Mechanical response of Ti–6Al–4V octet-truss lattice structures," *Int. J. Solids Struct.*, vol. 60–61, pp. 107–124, May 2015.

[117] S. R. Johnston, M. Reed, H. V Wang, and D. W. Rosen, "Analysis of Mesostructure Unit Cells Comprised of Octet-truss Structures."

[118] S. C. Kapfer, S. T. Hyde, K. Mecke, C. H. Arns, and G. E. Schröder-Turk, "Minimal surface scaffold designs for tissue engineering," *Biomaterials*, vol. 32, no. 29, pp. 6875–6882, 2011.

[119] L. R. Meza *et al.*, "Reexamining the mechanical property space of three-dimensional lattice architectures," *Acta Mater.*, vol. 140, pp. 424–432, Nov. 2017.

[120] L. C. Montemayor, L. R. Meza, and J. R. Greer, "Design and Fabrication of Hollow Rigid Nanolattices via Two-Photon Lithography," *Adv. Eng. Mater.*, vol. 16, no. 2, pp. 184–189, Feb. 2014.

[121] L. R. Meza, S. Das, and J. R. Greer, "Strong, lightweight, and recoverable three-dimensional ceramic nanolattices," *Science (80-. ).*, vol. 345, no. 6202, pp. 1322–1326, Sep. 2014.

[122] H. Montazerian, E. Davoodi, M. Asadi-Eydivand, J. Kadkhodapour, and M. Solati-Hashjin, "Porous scaffold internal architecture design based on minimal surfaces: A compromise between permeability and elastic properties," *Mater. Des.*, vol. 126, no. January, pp. 98–114, 2017.

[123] J. Shi, L. Zhu, L. Li, Z. Li, J. Yang, and X. Wang, "A TPMS-based method for modeling porous scaffolds for bionic bone tissue engineering," *Sci. Rep.*, vol. 8, no. 1, p. 7395, Dec. 2018.

[124] M. Wohlgemuth, N. Yufa, J. Hoffman, and E. L. Thomas, "Triply Periodic Bicontinuous Cubic Microdomain Morphologies by Symmetries," *Macromolecules*, vol. 34, no. 17, pp. 6083–6089, 2001.

[125] X. Zheng, Z. Fu, K. Du, C. Wang, and Y. Yi, "Minimal surface designs for porous materials: from microstructures to mechanical properties," *J. Mater. Sci.*, Apr. 2018.

[126] S. C. Han, J. W. Lee, and K. Kang, "A New Type of Low Density Material: Shellular," *Adv. Mater.*, vol. 27, no. 37, pp. 5506–5511, Oct. 2015.

[127] P. Hudon and I.-H. Jung, "Critical Evaluation and Thermodynamic Optimization of the CaO-P2O5 System," *Metall. Mater. Trans. B*, vol. 46, no. 1, pp. 494–522, Feb. 2015.

[128] J. D. Pasteris, “A mineralogical view of apatitic biomaterials,” *Am. Mineral.*, vol. 101, no. 12, pp. 2594–2610, Dec. 2016.

[129] E. R. Kreidel and F. A. Hummel, “CaO–P2O5, Phase Diagrams for Ceramist,” in *Two Oxides*, 1969.

[130] F. H. Perera, F. J. Martínez-Vázquez, P. Miranda, A. L. Ortiz, and A. Pajares, “Clarifying the effect of sintering conditions on the microstructure and mechanical properties of b-tricalcium phosphate,” 2010.

[131] J. Chen *et al.*, “A simple sol-gel technique for synthesis of nanostructured hydroxyapatite, tricalcium phosphate and biphasic powders,” *Mater. Lett.*, vol. 65, no. 12, pp. 1923–1926, Jun. 2011.

[132] M. B. Thürmer, C. E. Diehl, and L. A. L. dos Santos, “Calcium phosphate cements based on alpha-tricalcium phosphate obtained by wet method: Synthesis and milling effects,” *Ceram. Int.*, vol. 42, no. 16, pp. 18094–18099, Dec. 2016.

[133] B. Nasiri-Tabrizi and A. Fahami, “Mechanochemical synthesis and structural characterization of nano-sized amorphous tricalcium phosphate,” *Ceram. Int.*, vol. 39, no. 8, pp. 8657–8666, Dec. 2013.

[134] F. W. Zok, R. M. Latture, and M. R. Begley, “Periodic truss structures,” *J. Mech. Phys. Solids*, vol. 96, pp. 184–203, Nov. 2016.

[135] I. Gibson, D. Rosen, and B. Stucker, *Additive Manufacturing Technologies*. New York, NY: Springer New York, 2015.

[136] “ASTM D695-15, Standard Test Method for Compressive Properties of Rigid Plastics.” ASTM International, West Conshohocken, PA, 2015.

[137] J. B. Quinn and G. D. Quinn, “A practical and systematic review of Weibull statistics for reporting strengths of dental materials.,” *Dent. Mater.*, vol. 26, no. 2, pp. 135–47, Feb. 2010.

[138] J. Rodriguez-Carvajal, “FullProf.” 1993.

[139] B. I. Lazoryak, S. Y. Oralkov, V. N. Golubev, and A. N. Zhdanova, “Ca3[PO4]2,” *Russ. J. Inorg. Chem*, vol. 34, pp. 968–970, 1989.

[140] P. A. Arsen’ev, A. A. Evdokimov, S. A. Smirnov, M. R. Filimonova, V. M. Tsekhanovich, and M. Y. Sheinin, “Ca5[PO4]3[OH],” *Russ. J. Inorg. Chem*, vol. 37, pp. 1366–1368, 1992.

[141] J. C. Wurst and J. A. Nelson, “Lineal Intercept Technique for Measuring Grain Size in Two-Phase Polycrystalline Ceramics,” *J. Am. Ceram. Soc.*, vol. 55, no. 2, pp. 109–109, Feb. 1972.

[142] T. Kokubo and H. Takadama, “How useful is SBF in predicting in vivo bone bioactivity?,” *Biomaterials*, vol. 27, no. 15, pp. 2907–2915, May 2006.

[143] M. Griffin, L. Nayyer, P. E. Butler, R. G. Palgrave, A. M. Seifalian, and D. M. Kalaskar, “Development of mechano-responsive polymeric scaffolds using functionalized silica nano-fillers for the control of cellular functions.,” *Nanomedicine*, vol. 12, no. 6, pp. 1725–33, 2016.

[144] P. F. (Paul F. Jacobs and D. T. Reid, *Rapid prototyping & manufacturing : fundamentals of stereolithography*. Society of Manufacturing Engineers in cooperation with the Computer and Automated Systems Association of SME, 1992.

[145] G. Mitteramskogler *et al.*, “Light curing strategies for lithography-based additive manufacturing of customized ceramics,” pp. 110–118, 2014.

[146] N. Bouslama, F. Ben Ayed, and J. Bouaziz, “Mechanical properties of tricalcium phosphate-fluorapatite-alumina composites,” *Phys. Procedia*, vol. 2, pp. 1441–1448, 2008.

[147] V. der K. Industrie, “5. Eigenschaften Technischer Keramik,” in *Brevier Technische Keramik*,

Lauf: Fahner Verlag, 2003.

[148] F. Mangolini, J. B. McClimon, F. Rose, and R. W. Carpick, “Accounting for Nanometer-Thick Adventitious Carbon Contamination in X-ray Absorption Spectra of Carbon-Based Materials,” *Anal. Chem.*, vol. 86, no. 24, pp. 12258–12265, Dec. 2014.

[149] C. C. Chusuei, D. W. Goodman, M. J. Van Stipdonk, D. R. Justes, and E. A. Schweikert, “Calcium Phosphate Phase Identification Using XPS and Time-of-Flight Cluster SIMS,” *Anal. Chem.*, vol. 71, no. 1, pp. 149–153, Jan. 1999.

[150] H. B. Lu, C. T. Campbell, D. J. Graham, and B. D. Ratner, “Surface characterization of hydroxyapatite and related calcium phosphates by XPS and TOF-SIMS.,” *Anal. Chem.*, vol. 72, no. 13, pp. 2886–94, Jul. 2000.

[151] Verband der Keramischen Industrie, “7. Keramikgerechtes Konstruieren,” in *Brevier Technische Keramik*, Lauf: Fahner Verlag, 2003.

[152] A. M. Knapp and J. W. Halloran, “Binder Removal from Ceramic-Filled Thermoplastic Blends.”

[153] L. J. Gibson and M. F. Ashby, “Chapter 5 The mechanics of foams: basic results,” in *Cellular solids*, Cambridge: Cambridge University Press, 1997.

[154] S. C. Han, J. W. Lee, and K. Kang, “A New Type of Low Density Material: Shellular,” *Adv. Mater.*, vol. 27, no. 37, pp. 5506–5511, Oct. 2015.

[155] S.-H. Lee *et al.*, “Mechanical properties and cell-culture characteristics of a polycaprolactone kagome- structure scaffold fabricated by a precision extruding deposition system,” *Biomed. Mater*, vol. 12, 2017.

[156] B.-K. Lee and K.-J. Kang, “A parametric study on compressive characteristics of Wire-woven bulk Kagome truss cores,” *Compos. Struct.*, vol. 92, no. 2, pp. 445–453, Jan. 2010.

[157] J. M. Sobral, S. G. Caridade, R. A. Sousa, J. F. Mano, and R. L. Reis, “Three-dimensional plotted scaffolds with controlled pore size gradients: Effect of scaffold geometry on mechanical performance and cell seeding efficiency,” *Acta Biomater.*, vol. 7, no. 3, pp. 1009–1018, Mar. 2011.

[158] A. Tevlek, S. Odabas, E. Çelik, and H. M. Aydin, “Preparation of MC3T3-E1 cell sheets through short-term osteogenic medium application,” *Artif. Cells, Nanomedicine, Biotechnol.*, pp. 1–9, Jun. 2018.

[159] H.-J. Lee *et al.*, “Microgrooves on titanium surface affect peri-implant cell adhesion and soft tissue sealing; an *in vitro* and *in vivo* study,” *J. Periodontal Implant Sci.*, vol. 45, no. 3, p. 120, Jun. 2015.

[160] C. D. Hoemann, H. El-Gabalawy, and M. D. McKee, “In vitro osteogenesis assays: Influence of the primary cell source on alkaline phosphatase activity and mineralization,” *Pathol. Biol.*, vol. 57, no. 4, pp. 318–323, Jun. 2009.

[161] M. Lievremont, J. Potus, and B. Guillou, “Use of Alizarin Red S for Histochemical Staining of Ca2+ in the Mouse; Some Parameters of the Chemical Reaction in vitro,” *Cells Tissues Organs*, vol. 114, no. 3, pp. 268–280, 1982.

[162] C. . Hernandez, G. . Beaupré, T. . Keller, and D. . Carter, “The influence of bone volume fraction and ash fraction on bone strength and modulus,” *Bone*, vol. 29, no. 1, pp. 74–78, Jul. 2001.

[163] T. S. Keller, “Predicting the compressive mechanical behavior of bone,” *J. Biomech.*, vol. 27, no. 9, pp. 1159–1168, Sep. 1994.

[164] P. Tsimbouri *et al.*, “Nanotopographical Effects on Mesenchymal Stem Cell Morphology and Phenotype,” *J. Cell. Biochem.*, vol. 115, no. 2, pp. 380–390, Feb. 2014.